

國立交通大學
土木工程學系碩士班
碩士論文

點振動夯實造成砂土密度及土壓力變化
Variation of Soil Density and Earth Pressure due to
Vibratory Compaction at A Point



研究生：許仕達
指導教授：方永壽 博士

中華民國九十六年九月

點振動夯實造成砂土密度及土壓力變化
Variation of Soil Density and Earth Pressure due to
Vibratory Compaction at A Point

研究生：許仕達
指導教授：方永壽 博士

Student : Shih-Da Hsu
Advisor : Dr. Yung-Show Fang

國立交通大學土木工程學系碩士班

碩士論文

A Thesis

Submitted to the Department of Civil Engineering

College of Engineering

National Chiao Tung University

in Partial Fulfillment of the Requirements

for the Degree of

Master of Engineering in

Civil Engineering

September 2007

Hsinchu, Taiwan, Republic of China

中華民國九十六年九月

點振動夯實造成砂土密度及土壓力變化

研究生：許仕達 指導教授：方永壽 博士

國立交通大學土木工程學系碩士班

摘要

本論文以實驗方法探討點振動夯實造成疏鬆乾砂回填土之地表沉陷、密度變化及土壓力變化。本研究以氣乾渥太華砂作為回填土，回填土高 1.5 公尺。量測於鬆砂相對密度($D_r = 34\%$)表面進行單點振動夯實造成之砂土密度及土壓力變化。本變研究利用國立交通大學模型擋土牆設備來探討經過 7 秒、20 秒、46 秒、及 123 秒的地表振動夯實對地表沉陷、砂土密度及土壓力造成的變化。依據實驗結果，本研究獲得以下幾項結論。

1. 在鬆砂的回填土中，土壤內部的垂直與水平土壓力可以分別用 $\sigma_v = \gamma z$ 與 Jaky 公式估算。
2. 在無凝聚性土壤表面受夯實的受力情況可模擬成方形鋼樁承受振動式打樁機的貫入模式。在夯實過程中，土層發生地表沉陷，直到樁底的極限承載力 q_p 與振動夯實應力 σ_{cyc} 達到平衡。
3. 隨著夯實時間的增加，相對密度等高線($D_r = 36\%$)會往深處發展，並且土壤內部之最大相對密度 $D_{r,max}$ ，也會隨著夯實時間的增加而增大。
4. 隨著夯實時間的增加，土體殘餘的最大垂直與最大水平應力變化(夯實後測得的應力減去初始未夯實測得之應力)也跟著增加。這是因為隨著夯實時間增加，夯實能量也持續傳遞至土壤內部。
5. 夯實後移走夯實機，土壤內部可測得夯實造成之殘餘應力。最大的垂直應力

$\Delta\sigma_v$ 位置，隨著夯實時間的增加，此位置會從深度 250 mm 稍微向下移動至 350 mm 的位置。

關鍵字：夯實、土壤壓力、模型測試、沉陷、砂、相對密度



Variation of Soil Density and Earth Pressure due to Vibratory Compaction at a Point

Student : Shih-Da Hsu

Advisor : Dr. Yung-Show Fang

Department of Civil Engineering

National Chiao Tung University

Abstract

This paper studies the surface settlement, change of soil density and earth pressures due to vibratory compaction at a point. Dry Ottawa sand was used as the backfill material. The height of backfill was 1.5 m. The variation of soil density and earth pressure due to the vibratory compaction on the surface of the loose sand ($D_r = 34\%$) was measured. The instrumented model retaining-wall at National Chiao Tung University was used to investigate the variation of the surface settlement, soil density and earth pressures after 7, 20, 46 and 123 seconds of vibratory compaction. Based on the test results, the following conclusions were drawn.

1. For a loose backfill, the vertical and horizontal earth pressures in the soil mass can be properly estimated with the equation $\sigma_v = \gamma z$ and Jaky's equation, respectively.
2. The compaction of a cohesionless soil with a vibratory compactor can be simulated with the penetration of a square steel pile driven with a vibratory pile hammer. In the compaction process, the soils under the compacting plate settled until the ultimate tip resistance q_p and the cyclic compacting stress σ_{cyc} reached an equilibrium.
3. The depth of the relative density contour ($D_r = 36\%$) increased with increasing time of compaction. The peak relative density in the soil also increased with increasing time of compaction.
4. It was obvious that the peak $\Delta\sigma_v$ (3.60, 3.99, 4.44, 4.96, kN/m^2) and $\Delta\sigma_h$ (1.93,

2.41, 3.16, 3.32 kN/m²) increased with increasing compaction time. This is because, with increasing compaction time, more compaction energy was transmitted to the soil.

5. After the removal of the compactor, residual stresses in the soil mass were measured due to the vibratory compaction. The point of peak $\Delta\sigma_v$, as the compaction time increased, moved downward slightly from the depth of 250 mm to the depth of 350 mm.

Keywords: compaction, earth pressure, model test, settlement, sand, relative density.



Acknowledgements

The author wishes to give his sincere appreciation to his advisor, Dr. Yung-Show Fang for his enthusiastic advice and continuous encouragement in the past two years. If there is not the guidance from him, the thesis can not be accomplished.

Very special thanks are extended to Dr. Yii-Wen Pan, Dr. Jyh-Jong Liao, Dr. An-Bin Huang, Dr. Shinn-Yu Shann and Dr. Zhi-Ping Lin for their teaching and valuable suggestions. In addition, the author also wants to express his appreciation to the members of his supervisory committee, Dr. Mei-Ling Lin and Dr. Tsang-Jiang Chen for their helpful advice and discussions.

The author is indebted to his classmates for their stimulating suggestions and the donation of their time. Appreciation is extended to Mr. Hao-Chen Chang, Mr. Yu-Lun Chien, Mr. Yung-Cheng Cheng, Mr. Chun-Te Wu, Mr. Sheng-Feng Huang, Mr. Po-Shih Cheng and Miss I-Chen Chiang for their encouragement and assistance.

Table of Contents

	Page
Abstract (in Chinese)	i
Abstract	iii
Acknowledgements	v
Table of Contents	vi
List of Tables	ix
List of Figures	x
List of Symbols	xiv
Chapter 1 Introduction	1
1.1 Objectives of Study	1
1.2 Research Outline	2
Chapter 2 Literature Review	4
2.1 Earth Pressure At-Rest Theory	4
2.1.1 Coefficient of Earth Pressure At-Rest	4
2.1.2 Jaky's Formula	6
2.2 Ultimate Bearing Capacity of Surface Footing	7
2.3 Density Change due to Compaction	8
2.4 Elastic Solution	8
2.4.1 Boussinesq's Equations	8
2.4.2 Holl's Equations	9
2.5 Penetration of pile	10
2.6 Effective of Vibratory Compaction on Earth Pressure	11
2.6.1 Duncan and Seed	12
2.6.2 Study of Peck and Mesri	14
2.6.3 Study of Chen	15

	Page
Chapter 3 Experimental Apparatus	16
3.1 Soil Bin	16
3.2 Soil Pressure Transducers (SRT)	17
3.3 Data Acquisition System	17
3.4 Vibratory Soil Compactor	18
Chapter 4 Backfill Characteristics	19
4.1 Backfill Properties	19
4.2 Reduction of Wall Friction	20
Chapter 5 Experimental Results for Loose Sand	22
5.1 Control of Soil Density	22
5.1.1 Air-Pluviation of Backfill	22
5.1.2 Uniformity of Soil Density	23
5.2 Stresses in Loose Sand	23
Chapter 6 Variation of Surface Settlement and Soil Density due to Compaction	25
6.1 Pilot Tests	25
6.2 Surface Settlement due to Compaction	26
6.3 Density Change due to Compaction	27
Chapter 7 Variation of σ_v due to Compaction	29
7.1 Distribution of Vertical Earth Pressure after Compaction	29
7.1.1 Testing procedure	29
7.1.2 Test result	30
7.2 Change of Vertical Earth Pressure due to Compaction	31
Chapter 8 Variation of σ_h due to Compaction	32
8.1 Distribution of Horizontal Earth Pressure after Compaction ..	32
8.2 Change of Horizontal Earth Pressure due to Compaction	33
8.3 Mechanism of Soils under Compaction	34
Chapter 9 Conclusions	35

	Page
Reference	36
Tables	40
Figures	44
Appendix A: Calibration of Soil Pressure Transducer	128
Appendix B: Operation of Software Sufer 8 and Grapher 7 and Rlative Density Measured at Grid Points after Compaction	141
Appendix C: $\Delta\sigma_v$ Measured at Grid Points after Compaction	145
Appendix D: $\Delta\sigma_h$ Measured at Grid Points after Compaction	148



List of Tables

No.		Page
3.1	Technical information of the Acentric Motor	40
4.1	Properties of Ottawa Sand	41
6.1	Determination of compaction time for testing with hyperbolic model	42
6.2	Compaction Time for Testing with Corresponding Settlement of the Center of Square Compactor	42
6.3	Compaction between the NCTU's Compaction Tests and D'Appolonia's Field Tests	43



List of Figures

No.		Page
1.1	Compaction on the surface of a 1500 mm-thick loose sand	44
1.2	Compaction of backfill using hand tamper (after Day, 1998)	45
2.1	Development of in-situ stresses (after Chen, 2003)	46
2.2	Principal stresses in soil element (after Chen, 2003)	47
2.3	Jaky's formulation of the relationship between K_o on OC and ϕ mobilized in OAB (after Mesri and Hayat, 1993)	48
2.4	(a) Mode of foundation failure in sand (after Vesic, 1973) (b) Definition of failure mode (after Vesic, 1973)	49
2.5	Settlement of circular and rectangular plates used to achieve an ultimate load ($D_f / B = 0$) in sand (after Vesic, 1963)	50
2.6	Growth curves for a silty clay - relationship between dry unit weight and number of passes of 84.5 kN three-wheel roller when the soil is compacted in 229 mm loose layers at different moisture contents (after Johnson and Sallberg, 1960)	51
2.7	Vibratory compaction of a sand - variation of dry unit weight with number of roller passes; thickness of lift = 2.45 m (after D'Appolonia, et al., 1969)	52
2.8	Principles of vibratory rollers (after Das, 1994)	53
2.9	Stresses due to a vertical point load in rectangular coordinates (after Boussinesq, 1883)	54
2.10	Stresses below the corner of a rectangular loaded area	55
2.11	Ultimate load-carrying capacity of pile (after Das, 2004)	56
2.12	Nature of variation of unit point resistance in a homogeneous sand (after Das, 2004)	57
2.13	Variation of the maximum values of N_q^* with soil friction with soil friction angle ϕ' (after Meyerhof, 1976)	58
2.14	Load transfer mechanism for piles at deep foundation in a punching mode (after Das, 2004)	59
2.15	Basic components of hysteretic K_o -loading/unloading model (after Duncan and Seed, 1986)	60
2.16	Hand-calculation for estimating σ_h (after Peck and Mesri, 1987)	61

2.17	Distribution of horizontal earth pressure after compaction (after Chen, 2003)	62
3.1	NCTU non-yielding soil bin (after Chen, 2003)	63
3.2	Soil-pressure transducer (Kyowa BE-2KCM17) (after Chen, 2003) ..	64
3.3	Data acquisition system (after Wang, 2005)	65
3.4	Acentric motors (Mikasa KJ75) (after Wang, 2005)	66
3.5	Side-view of vibratory soil compactor (after Chen, 2003)	67
3.6	Vibratory soil compactor (after Chen, 2003)	68
4.1	Grain size distribution of Ottawa sand (after Hou, 2006)	69
4.2	Shear box of direct shear test device (after Wu, 1992)	70
4.3	Relationship between unit weight γ and internal angle (after Chang, 2000)	71
4.4	Lubrication layers on four walls	72
4.5	Schematic diagram of sliding block test (after Fang et al., 2004)	73
4.6	Sliding block test apparatus (after Fang et al., 2004)	74
4.7	Variation of interface angle with normal stress (after Fang et al., 2004)	75
5.1	Soil hopper	76
5.2	Pluviation of dry sand into soil bin	77
5.3	Relationship between relative density and drop height (after Ho, 1999)	78
5.4	Soil-density cup (after Ho, 1999)	79
5.5	Soil-density cup	80
5.6	Soil density cups buried at the different elevations	81
5.7	Locations of soil density cups at the same elevation	82
5.8	Steps of soil density control test	83
5.9	Distribution of soil density for loose sand	84
5.10	(a) Locations of SPT to measure vertical earth pressure; (b) Locations of SPT to measure horizontal earth pressure	85
5.11	Positioning of soil pressure transducer in the backfill	86
5.12	(a) SPT placed in soil bin to measure σ_v ; (b) SPT placed in soil bin to measure σ_h	87
5.13	(a) Distributions of vertical earth pressure; (b) Distributions of horizontal earth pressure	88

6.1	Major cross-section of measurement in this study	89
6.2	Measurement of surface settlement	90
6.3	Hyperbolic model to estimate surface settlement S as a function of time of compaction	91
6.4	Variation of surface settlement due to point compaction	92
6.5	Surface settlement after due to 123 s of compaction	93
6.6	Location of soil density cups in the backfill (side-view)	94
6.7	Location of soil density cups (top-view)	95
6.8	Relative density measured at grid points after 7 s of point compaction	96
6.9	Distribution of relative density after 7 s of point compaction	97
6.10	Distribution of relative density after 20 s of point compaction	98
6.11	Distribution of relative density after 46 s of point compaction	99
6.12	Distribution of relative density after 123 s of point compaction	100
6.13	Relationship between relative density and compaction time	101
6.14	Comparison of distribution of soil unit weight after compaction	102
7.1	Location of SPT to measure σ_v under the center of compactor (side view)	103
7.2	Distributions of σ_v under compactor	104
7.3	Change of vertical earth pressure under compactor	105
7.4	Location of SPT to measure $\Delta\sigma_v$ (side view)	106
7.5	SPT placed in soil bin (top view)	107
7.6	Location of SPT to measure $\Delta\sigma_v$ (top view)	108
7.7	$\Delta\sigma_v$ after 7 s of point compaction measured at grid points	109
7.8	Distribution of $\Delta\sigma_v$ after 7 s of compaction	110
7.9	Distribution of $\Delta\sigma_v$ after 20 s of compaction	111
7.10	Distribution of $\Delta\sigma_v$ after 46 s of compaction	112
7.11	Distribution of $\Delta\sigma_v$ after 123 s of compaction	113
7.12	Vertical earth pressure due to the surface Square loading q by Holl's elastic equation	114
8.1	Location of SPT to measure σ_h under the center of compactor (side view)	115
8.2	Distributions of σ_h under compactor	116

8.3	Change of horizontal earth pressure under compactor	117
8.4	Location of SPT to measure $\Delta\sigma_h$ (side view)	118
8.5	SPT placed in soil bin (top view)	119
8.6	Location of SPT to measure $\Delta\sigma_h$ (top view)	120
8.7	$\Delta\sigma_h$ after 7 s of point compaction measured at grid points	121
8.8	Distribution of $\Delta\sigma_h$ after 7 s of compaction	122
8.9	Distribution of $\Delta\sigma_h$ after 20 s of compaction	123
8.10	Distribution of $\Delta\sigma_h$ after 46 s of compaction	124
8.11	Distribution of $\Delta\sigma_h$ after 123 s of compaction	125
8.12	Horizontal earth pressure due to the surface loading q by Holl's elastic equation	126
8.13	Mechanism of soils under 123 seconds vibratory compaction liked the penetration of pile	127



List of Symbols

C_u	= Coefficient of uniformity of soil
D_r	= Relative density of soil
D_{10}	= Soil particle diameter corresponding to 60% finer
D_{60}	= Soil particle diameter corresponding to 10% finer
E	= Young's modulus
e_{\max}	= Maximum void ratio of soil
e_{\min}	= Minimum void ratio of soil
G_s	= Specific gravity of soil
K_o	= Coefficient of earth pressure at-rest
K_a	= Coefficient of active earth pressure
K_p	= Coefficient of passive earth pressure
t	= Compaction time
S	= Surface settlement
z	= Depth
ϕ	= Internal friction angle of soil
δ	= Wall friction angle
δ_{sw}	= Angle of side wall friction
σ	= Normal stress
σ_h	= Horizontal earth pressure
σ_v	= Vertical earth pressure
σ_{cyc}	= Cyclic normal stress
$\Delta\sigma_h$	= Change of horizontal earth pressure
$\Delta\sigma_v$	= Change of vertical earth pressure
γ	= Unit weight of soil
ν	= Poisson's ratio
τ	= Shear stress
ε	= Normal strain



Chapter 1

INTRODUCTION

In this study, the effects of the vibratory compaction on the surface of a cohesionless soil mass are studied. Fig 1.1 shows the vibratory compaction on the surface of a 1500 mm-thick loose sand for this study. To achieve a dense backfill in the field the vibratory compactor is commonly used to densify the backfill. With a horizontal ground level, the geostatic vertical stress σ_v before compaction can be estimated from its effective overburden pressure $\sigma_v = \gamma z$. The horizontal earth pressure σ_h before compaction can be estimated from the Jaky's (1944) equation $\sigma_h = K_0 \gamma z$. However, after the vibratory compaction, how to estimate the change of soil density due to compaction? How to determine the variation of earth pressure in the backfill due to compaction? In this paper, experiments were conducted with the NCTU model retaining wall facilities to investigate the change of soil density and earth pressures due to vibratory compaction at a point.

1.1 Objectives of Study

In most specifications for earthworks, the contractor is required that the backfill be compacted to 90-95 % of its maximum dry unit weight ($\gamma_{d,max}$) determined by the Standard Proctor test. Compaction is considered as an artificial densification of an earth mass. It is a particular kind of soil stabilization and one of the oldest methods for improving existing soil or man-placed fills. The objective of the compaction operation is to improve the engineering properties of soil, such as increasing the fill's bearing capacity or reducing settlement. For granular soils, achieving a relative density of 70-75 % is generally recommended (see the NAVFAC Design Manual) (US Navy, 1982) by vibratory compaction. Therefore, in most cases, the backfill

encountered in the field would be dense soil. As indicated in Fig. 1.2, hand tampers or vibratory compaction equipment are commonly used to densify the backfill.

To analyze the residual lateral earth pressure induced by soil compaction, several methods of analysis have been proposed by Rowe (1954), Broms (1971), Duncan and Seed (1986), Peck and Mesri (1987) and other researchers. Duncan et al. (1991) used the analytical procedures proposed by Duncan and Seed (1986) to develop earth pressure charts and tables that can be used to estimate residual earth pressure due to compaction. However, little information regarding the mechanism of soils under compaction has been reported. This study presents experimental data to investigate the surface settlement, change of soil density, and earth pressures in the soil mass induced by the vibratory compaction. The mechanism of soils under vibratory compaction is proposed. All experiments mentioned in this study were conducted in the National Chiao Tung University (NCTU) retaining wall facility that is described in Chapter 3. The vertical and horizontal stresses in the soil mass were measured with the soil pressure transducers (SPTs) which were embedded in the backfill.

1.2 Research Outline

This research utilizes the NCTU model wall facility to investigate the surface settlement, change of soil density, and earth pressures in the soil mass due to compaction. Previous studies associated with the effects of compaction on soil behavior are summarized in Chapter 2. Details of the NCTU non-yielding model wall system and the vibratory compactor used to densify the backfill are discussed in Chapter 3. Test results regarding the characteristics of the backfill are introduced in Chapter 4. To reduce the effects of the boundary friction, the arrangement of lubrication layers on the four walls are discussed.

In Chapter 5, experiments were conducted to study the distribution of soil density in the loose backfill prepared with air-pluviation method. Test results

regarding the vertical and horizontal stresses in the loose sand are also reported in Chapter 5.

The variation of the surface settlement, change of soil density and earth pressures in the soil mass due to vibratory compaction was studied Chapter 6. Pilot tests were conducted to establish the program of compaction tests. the point compaction time was determined.

After determining the time of compaction, experiments were conducted and the stresses in the soil mass were measured. In Chapter 7, test results associated with the $\Delta\sigma_v$ were reported. In Chapter 8, the test results regarding $\Delta\sigma_h$ due to compaction were reported. Based on the experimental results, the mechanism of the cohesionless backfill subjected to a vibratory compaction was proposed.



Chapter 2

LITERATURE REVIEW

Previous studies regarding the surface settlement, change of soil density, and earth pressures after vibratory compaction are introduced in this chapter. In the field, the vibratory compaction is commonly used to densify the soil mass. However, the effects due to vibratory compaction at a point on the surface of a cohesionless backfill have received little attention in the literature.

2.1 Earth Pressure at-Rest

Donath (1891) was the first to introduce the concept of “the stationary pressure of unlimited ground”. Donath (1891) defined the coefficient of earth pressure K as the ratio of the effective horizontal pressure (σ_h) to the effective vertical earth pressure (σ_v) in soil

$$K = \frac{\sigma_h}{\sigma_v} \quad (2.1)$$

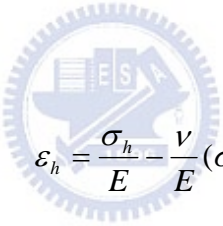
2.1.1 Coefficient of Earth Pressure at-Rest

The coefficient at-rest K_o is refer to the condition where no lateral yielding occurs, under the condition of constrained lateral deformation. As shown in Fig. 2.1(a), the overburden pressure σ_v , compresses the soil element A formed in a horizontal sedimentary deposit. During the formation of the deposit, the element is consolidated under this vertical pressure. The

vertical stress produces a lateral deformation against surrounding soils due to the Poisson's ratio effect. However, based on the definition and the field observation, over the geological period, the horizontal strain is kept to zero. It is concluded that the surrounding soil resists the lateral deformation with a developed lateral stress σ_h . A stable stress state will develop in which σ_h and σ_v become stresses acting on the vertical and horizontal planes as shown in Fig. 2.1(b). For an isotropic soil element shown in Fig. 2.2, if the soil behaved as an ideal elastic material, based on the mechanics of materials, the lateral strain ε_y can be expressed as:

$$\varepsilon_y = \frac{\sigma_y}{E} - \frac{\nu}{E}(\sigma_x + \sigma_z) \quad (2.2)$$

or



$$\varepsilon_h = \frac{\sigma_h}{E} - \frac{\nu}{E}(\sigma_h + \sigma_v) \quad (2.3)$$

where E is the elastic modulus and ν is the Poisson's ratio of the soil.

Base on the definition of the at-rest condition, the lateral strain would be zero under the application of stress state and the $\sigma_h = K_o \sigma_v$. Then the Eq. 2.3 can be written as:

$$\varepsilon_h = \frac{1}{E}(K_o \sigma_v - \nu K_o \sigma_v - \nu \sigma_v) = 0 \quad (2.4)$$

and the coefficient of earth pressure at-rest K_o :

$$K_o = \frac{\nu}{1-\nu} \quad (2.5)$$

It should be mentioned that Eq. 2.5 is applicable for the isotropic and the

elastic materials only. However, the behavior of soil element is more complex and far from these assumptions. It is evident that the relationship between K_o and elastic parameter ν of Eq. 2.5 is obsolescent for predicting in-situ horizontal stress.

2.1.2 Jaky's Formula

Attempts have been made to establish a theoretical relationship between the strength properties of a soil and K_o . The empirical relationship to estimate K_o of coarse-grained soils is discussed in this section.

Mesri and Hayat (1993) reported that Jaky (1944) arrived at a relationship between K_o and the angle of internal friction ϕ by analyzing a talus of granular soil freestanding at the angle of repose. Jaky (1944) assumed that the angle of repose is equal to the angle of internal friction ϕ . This assumption is reasonable for sedimented, normally consolidated materials for which the angle of repose is equal to the constant-volume friction angle, ϕ_{cv} (Cornforth, 1973). Darwin (1883) defined the angle of repose as the greatest inclination to the horizon at which a talus will stand. Jaky (1944) reasoned that the sand cone OAD in Fig. 2.3 is in a state of equilibrium and its surface and inner points are motionless. The horizontal pressure acting on OC is the earth pressure at-rest. As OC is a line of symmetry, shear stresses can not develop on it. Hence OC is a principal stress trajectory. Based on the equations of equilibrium, Jaky expressed the coefficient of earth pressure at-rest with the angle of internal friction,

$$K_o = (1 - \sin \phi) \frac{1 + \frac{2}{3} \sin \phi}{1 + \sin \phi} \quad (2.6)$$

In 1948, Jaky presented a simplified version of the expression given by

Eq. 2.6.

$$K_o = 1 - \sin \phi \quad (2.7)$$

These expressions were the first attempt to relate the coefficient of earth pressure at-rest K_o to the angle of resistance ϕ of the soil. Eq. 2.7 is still widely used due to its practical significance and attractive simplicity. It should be mentioned that Jaky's analysis was for a soil with $\phi = \phi_{cv}$. Thus, these expressions were suitable for K_o of sedimented, normal consolidated clays and granular materials that have not been densified by vibration or compaction.

2.2 Ultimate Bearing Capacity of Surface Footing

To study the mechanism of soils under vibratory compaction, it is helpful to study the bearing failure of a shallow footing. In Fig. 2.4, Vesic (1973) defined three types of the bearing failure mode with the soil density and the depth of embedment of footing. Typical failure modes of a footing includes: punch shear failure, local shear failure, and general shear failure. If the relative density of backfill is about 34% and the vertical loading was applied on the surface of the backfill ($D_f = 0$). Based on Fig. 2.4, the punching shear failure would occur under the loaded footing.

Vesic (1963) presented the settlement S required for circular and rectangular plates acting on the surface of a sand to reach an ultimate load. Fig. 2.5. indicates a general range of S/B required to reach q_{ult} as a function of the relative density of the foundation soil. In general, for foundations on a dense sand, the ultimate load q_{ult} would occur at a foundation settlement of 4 ~ 10 % of B . The S/B increases together with the decrease of soil density. In the case of local or punching shear failure, the ultimate load would occur at the settlement of $0.14B \sim 0.23B$.

2.3 Density Change due to Compaction

Johnson and Sallberg (1960) proposed that the dry unit weight of soil would be affected by the number of roller passes during compaction. Fig. 2.6 shows the growth curves for a silty clay soil. The dry unit weight of a soil at a given moisture content increases to a certain point with the number of roller passes. Beyond this point, the dry unit weight remains approximately constant. In most cases, about 10 to 15 roller passes yield the maximum dry unit weight economically attainable.

D'Appolonia, et al. (1969) reported that the variation in the unit weight of compaction with depth for a poorly graded sand for which compaction was achieved by a vibratory drum roller is as shown in Fig. 2.7. The vibratory drum roller is shown in Fig. 2.8. Vibration was produced by mounting an eccentric weight on a single rotating shaft within the drum cylinder. The weight of the roller used for this compaction was 55.6 kN, and the drum diameter was 1.19 m. The lifts were kept at 2.44 m. In Fig. 2.7 at any given depth, the dry unit weight of compaction increases with the number of roller passes. However, the rate of increase in unit weight of soil gradually decreases after about 15 passes. Another fact from Fig. 2.7 is the distribution of dry unit weight with depth for any given number of roller pass. The dry unit weight and hence the relative density, D_r , reach maximum values at a depth of about 0.5 m and gradually decreases at lesser depths. This decrease occurs because of the lack of confining pressure near the surface of the fill.

2.4 Elastic Solution

2.4.1 Boussinesq's Equations

Boussinesq (1883) developed theoretical expressions for determining stresses at a point within an "ideal" mass due to a surface point load. The theory was based on the assumptions that the mass is an elastic, isotropic, homogeneous, and semi-infinite medium that extends infinitely in all directions from a level surface. Boussinesq's equations provide a widely used basis for estimating the stresses within a soil mass caused by a concentrated load applied perpendicularly to the soil surface.

Boussinesq's equation may be expressed in terms of rectangular coordinates. Referring to the element shown in Fig. 2.9, the two equations to determine the vertical normal stress σ_z and the horizontal normal stress σ_x are as follow:

$$\sigma_z = \frac{3Qz^3}{2\pi R^5} \quad (2.8)$$

$$\sigma_x = \frac{3Q}{2\pi} \left\{ \frac{x^2}{R^5} + \frac{1-2\mu}{3} \left[\frac{1}{R(R+z)} - \frac{(2R+z)x^2}{R^3(R+z)^2} - \frac{z}{R^3} \right] \right\} \quad (2.9)$$

where

$Q = \text{point load}$

$r = \sqrt{x^2 + y^2}$

$R = \sqrt{z^2 + r^2}$

$\mu = \text{Poisson's ratio}$

2.4.2 Holl's Equations

Holl (1940) advanced the integration technique of Boussinesq's equation for determining stresses at the point A which is beneath the corner of a rectangle rectangular load. Referring to the Point A shown in Fig. 2.10, the two equations to determine the vertical normal stress σ_z and the horizontal normal stress σ_x are as follows:

$$\sigma_z = \frac{q_o}{2\pi} \left[\tan^{-1} \frac{LB}{zR_3} + \frac{LBz}{R_3} \left(\frac{1}{R_1^2} + \frac{1}{R_2^2} \right) \right] \quad (2.10)$$

$$\sigma_x = \frac{q_o}{2\pi} \left[\tan^{-1} \frac{LB}{zR_3} - \frac{LBz}{R_1^2 R_3} \right] \quad (2.11)$$

where

$q_o = \text{load per unit area}$

$$R_1 = \sqrt{L^2 + z^2}$$

$$R_2 = \sqrt{B^2 + z^2}$$

$$R_3 = \sqrt{L^2 + B^2 + z^2}$$

2.5 Penetration of Pile

The penetration of a pile into the ground is shown in Fig. 2.11. Fig. 2.12 shows that the unit point resistance q_p of a pile in sand generally increases with increasing depth of embedment then reaches a maximum value at an embedment ratio of $L/D = (L_b/D)_{cr}$. In a homogeneous soil L_b is equal to the actual embedment length of the pile, L (Fig. 2.11). However, where a pile has penetrated into a bearing stratum $L_b < L$. Beyond the critical embedment ratio, $(L_b/D)_{cr}$, the value of q_p remains constant ($q_p = q_l$). That is, as shown in Fig. 2.12 for the case of a homogeneous soil, $L = L_b$. For piles in sand, $c' = 0$, the point bearing of piles is

$$Q_p = A_p q_p = A_p q' N_q^* \quad (2.12)$$

where

$Q_p = \text{point bearing capacity}$

$A_p = \text{area of pile tip}$

$c' = \text{cohesion of the soil supporting the pile tip}$

$q_p = \text{unit point resistance}$

$q' = \text{effective vertical stress at the level of the pile tip}$

N_c^* , N_q^* = the bearing capacity factors

The variation of N_q^* with soil friction angle ϕ' is shown in Fig. 2.13. However, Q_p should not exceed the limiting value $A_p q_l$; that is,

$$Q_p = A_p q' N_q^* \leq A_p q_l \quad (2.13)$$

The limiting point resistance is

$$q_l = 0.5 p_a N_q^* \tan \phi' \quad (2.14)$$

where

p_a = atmospheric pressure ($p_a = 100 \text{ kN/m}^2$)

ϕ' = effective soil friction angle of the bearing stratum

At an ultimate load, the failure surface in the soil at the pile tip (a bearing capacity failure caused by Q_p) is like that shown in Fig. 2.14. Pile foundations are deep foundations and that the soil fails mostly in a punching mode, as illustrated previously in Fig. 2.4. That is, a triangular zone, I, is developed at the pile tip, which is pushed downward without producing any other visible slip surface. In dense sands and stiff clayey soils, a radial shear zone, II, may partially develop. Hence, the load displacement curves of piles will resemble those shown in Fig. 2.4.

2.6 Effects of Vibratory Compaction on

Earth Pressure

Compaction of soil can produce a stiff, settlement-free and less permeable mass. It is usually accomplished by mechanical means that cause the density of soil to increase. At the same time the air voids are reduced. It has been realized that the compaction of the backfill material has an important effect on the earth pressure.

Some theories introduce the idea that compaction represents a form of overconsolidation, where stresses resulting from a temporary or transient loading condition are retained following removal of this load.

2.6.1 Study of Duncan and Seed

Duncan and Seed (1986) presented an analytical procedure for the calculation of peak and residual compaction-induced stresses either in the free field or acting against vertical non-yielding structures. This procedure employs a hysteretic K_o -loading model (Fig. 2.15) to track the vertical and lateral stresses for a lift of backfill as it is placed, and as overlying lifts are subsequently placed and compacted. In their model, it is assumed that the effect of compaction could be considered as a cyclic surcharge on the backfill surface. When the surcharge is applied on the soil surface, it will increase the vertical stress and the horizontal stress. In Fig. 2.15, as the virgin loading is applied on the soil, both σ_v and σ_h increase along the K_o -line ($K_o = 1 - \sin\phi$). However, when the surcharge is removed, σ_v and σ_h would decrease along the virgin unloading path. All unloading is subject to the passive failure limiting conditions. When virgin reloading was applied again, the increment of earth pressure is less than that induced by virgin loading.

The hysteretic model was used to the analysis. Compaction was represented by a transient, moving surficial load of finite lateral extent by directly modeling loading as an increase in vertical effective stress ($\Delta\sigma_v$). To simulate the compaction loading, a parameter of the peak virgin, compaction-induced horizontal stress increase ($\Delta\sigma'_{h,vc,p}$) is defined as the horizontal effective stress which would be induced by the most critical positioning of the compactor. If the soil had been previously uncompacted (that is, the soil had no “lock-in” residual stresses due to previous compaction), $\Delta\sigma'_{h,vc,p}$ can be obtained by using the simple elastic analysis. The hysteretic K_o model described up to this point is a one-dimensional model. But a compactor does not cover the entire backfill surface and the real case is three-dimensional. To account for the three-dimensional effects, an “equivalent peak vertical stress” is applied to represent the compactor in the K_o -model. Compaction loading would be modeled on the basis of $\Delta\sigma'_{h,vc,p}$ transformed to an equivalent peak vertical stress increase ($\Delta\sigma'_{v,e,p}$)

which can be calculated as

$$\Delta\sigma'_{v,e,p} = \frac{\Delta\sigma'_{h,vc,p}}{K_o} \quad (2.15)$$

In this model the peak compaction loading was based on directly calculated lateral stress increase, rather than on the basis of a directly calculated peak vertical stress increase subsequently multiplied by K_o , K_a or some other coefficient. Seed and Duncan (1983) presented a study and recommendations for the calculation of $\Delta\sigma'_{h,vc,p}$ for various situation. Seed and Duncan (1983) concluded that either in the free field, or at or near vertical, nondeflecting soil/structure interfaces, $\Delta\sigma'_{h,vc,p}$ resulting from surficial compaction loading can be calculated directly by simple elastic analysis. The parameter of Poisson's ratio, ν for surficial compaction loading was chosen according to the empirically derived relationship

$$\nu = \nu_o + \frac{1}{2}(0.5 - \nu_o) \quad (2.16)$$

where $\nu_o = \frac{K_o}{1 + K_o}$

and $K_o = 1 - \sin\phi$

Seed and Duncan (1983) also pointed that based on the observation of field measurements, the loading imposed by a typical vibratory roller can be modeled as approximately two to four times the static weight of the roller. For $\Delta\sigma'_{h,vc,p}$ acting at a vertical, nondeflecting soil-structure interface due to concentrated surficial loading can be taken as twice the value that would be calculated at the same point by closed-form elastic solutions. Unfortunately, as the comments by Seed and Duncan, the hysteretic model is very complex. However, based on the concept, the proposed model may be incorporated in an increment analytical procedure, which can be used to evaluate the earth pressure resulting from the placement and compaction of soil layers.

2.6.2 Study of Peck and Mesri

Based on the elastic analysis, Peck and Mesri (1987) presented a calculation method to evaluate the compaction-induced earth pressure. The lateral pressure profile can be determined by four conditions on σ_h , as illustrated in Fig. 2.16 and summarized in the following.

1. Lateral pressure resulting from the overburden of the compacted backfill,

$$\sigma_h = (1 - \sin \phi) \gamma z \quad (2.17)$$

2. Lateral pressure limited by passive failure condition,

$$\sigma_h = \tan^2(45 + \phi/2) \gamma z \quad (2.18)$$

3. Lateral pressure resulting from backfill overburden plus the residual horizontal stresses,

$$\sigma_h = (1 - \sin \phi) \gamma z + \frac{1}{4} (5^{1.2 \sin \phi} - 1) \Delta \sigma_h \quad (2.19)$$

where $\Delta \sigma_h$ is the lateral earth pressure increase resulted from the surface compaction loading of the last backfill lift and can be determined based on the elastic solution.

4. Lateral pressure profile defined by a line which envelops the residual lateral pressures resulting from the compaction of individual backfill lifts. This line can be computed by Eq. 2.20.

$$\frac{\Delta \sigma_h}{\Delta z} = \frac{1 - \sin \phi}{4} (5 - 5^{1.2 \sin \phi}) \gamma \quad (2.20)$$

Fig. 2.16 indicates that near the surface of backfill, from point a to b, the lateral pressure on the wall is subject to the passive failure condition. From b to c, the overburden and compaction-induced lateral pressure profile is determined by Eq. 2.19.

From c the lateral pressure increases with depth according to Eq. 2.20 until point d is reached. Below d, the overburden pressure exceeds the peak increase in stress by compaction. In the lower part of the backfill, the lateral pressure is directly related to the effective overburden pressure.

2.6.3 Study of Chen

Chen (2003) reported some experiments in non-yielding retaining wall at National Chiao Tung University to investigate influence of earth pressure due to vibratory compaction. Air-dry Ottawa sand was used as backfill material. Vertical and horizontal stresses in the soil mass were measured in loose and compacted sand. Based on his test results, Chen (2003) proposed three points of view: (1) after compaction, the lateral stress measured near the top of backfill is almost identical to the passive earth pressure estimated with Rankine theory (Fig. 2.17). The compaction-influenced zone rises with rising compaction surface. Below the compaction-influenced zone, the horizontal stresses converge to the earth pressure at-rest, as indicated in Fig. 2.17 (e); (2) when total (static + dynamic) loading due to the vibratory compacting equipment exceeds the bearing capacity of foundation soils, the mechanism of vibratory compaction on soil can be described with the bearing capacity failure of foundation soils; (3) the vibratory compaction on top of the backfill transmits elastic waves through soil elements continuously. For soils below the compaction-influenced zone, soil particles are vibrated. The passive state of stress among particles is disturbed. The horizontal stresses among soil particles readjust under the application of a uniform overburden pressure and constrained lateral deformation, and eventually converge to the at-rest state of stress.

Chapter 3

EXPERIMENTAL APPARATUS

To investigate the effects of vibratory compaction on the vertical and horizontal stresses in a cohesionless soil mass, an instrumented model retaining wall facility at National Chiao Tung University (NCTU) was used. This chapter introduces the NCTU model retaining wall facilities and the vibratory compactor used to densify the loose backfill. The NCTU non-yielding retaining wall facilities consist of three components: (1) the soil bin, (2) soil pressure transducers, and (3) the data acquisition system (Chen and Fang, 2002). The details of the foregoing apparatuses are described in the following sections.



3.1 Soil Bin

The soil bin was designed to minimize the lateral deflection of the four walls. The soil bin was made of steel plates with inside dimensions of 1500 mm \times 1500 mm \times 1600 mm as illustrated in Fig. 3.1. The sidewalls and end-wall of the soil bin were made of 35 mm-thick steel plates. Vertical steel columns and horizontal steel beams were used to increase the stiffness of the soil bin. If the soil bin was filled with dense sand, the estimated maximum deflection of the sidewall would be 1.86×10^{-3} mm. The bottom of the soil bin was covered with a layer of SAFETY WALK to provide adequate friction between the soil and the base of the bin.

The model wall shown in Fig. 3.1 is 1500 mm-wide, 1600 mm-high, and 45 mm-thick. To achieve an at-rest condition, the wall material should be nearly rigid. As a result, a solid steel plate with a Young's modulus of 210 GPa was chosen as the wall material. As indicated in Fig. 3.1, the model wall is actually the front-side of the

reinforced steel box. To avoid the lateral deformation of the box, twenty-four 20 mm-thick steel columns were welded vertically on the outside of the box. In addition, twelve C-shaped steel beams were welded horizontally around the box to further increase the stiffness of the box.

Assuming a 1.5 m-thick cohesionless backfill with a unit weight $\gamma = 17.1 \text{ kN/m}^3$, and an internal friction angle $\phi = 41^\circ$ was pluviated into the box. The estimated deflection of the model wall would be only $1.22 \times 10^{-3} \text{ mm}$. Therefore, it can be concluded that the lateral deformation of the model wall is negligible. From a practical point of view, the model wall, sidewalls, end-wall, and base plate of the soil bin were welded together to reduce flexibility..

3.2 Soil Pressure Transducers (SPT)

To investigate the development of stresses in the backfill, a series of soil pressure transducers (Kyowa BE-2KCM17, capacity = 98.1 kN/m^2) were embedded in the cohesionless soil mass. The transducers were used to measure the variation of vertical and horizontal earth pressure after the filling and compaction of the backfill. The soil pressure transducers buried in the backfill were strain-gage-type transducers as shown in Fig. 3.2. The five radial extensions attached to the transducers were used to prevent possible rotation of the transducer due to vibratory compaction. The effective diameter of the transducer was 22 mm and its thickness was 6 mm.

3.3 Data Acquisition System

A data acquisition system was used to collect and store the considerable amount of data generated during the tests. In the Fig. 3.3, the data acquisition system was composed of the following three parts: (1) dynamic strain amplifiers (Kyowa: DPM601A and DPM711B); (2) AD/DA card (NI BNC-2090); and (3) Personal Computer. The analog signals from the sensors were filtered and amplified by the dynamic strain amplifiers (Kyowa DPM601A and DPM711B). Then, the analog test

data were digitized by an A/D-D/A card. Finally, the digital data were transmitted to the personal computer for storage and analysis.

3.4 Vibratory Soil Compactor

To simulate compaction of backfill in the field, a vibratory soil compactor was used. The acentric motor (Mikasa, KJ75-2P) was selected to be the source of vibration. The acentric force generated by the motor could be controlled by adjusting the number of acentric plates attached to the motor as illustrated in Fig. 3.4. Fig. 3.4 shows acentric steel plates were attached to the central rotating shaft of the motor. For this study, sixteen acentric plates (8+8) were used. Detail information regarding the acentric motor was listed in Table 3.1.

The vibratory soil compactor with the base area of 225 mm × 225 mm was illustrated in Fig. 3.5 and Fig. 3.6. The acentric motor was fixed on the steel compaction plate of the compactor. The height of the handle is 1.0 m, and the total mass of the compactor was 12.1 kg (0.119kN). Chen (2003) reported the peak cyclic vertical force (static + dynamic) measured with a load cell placed under the base plate of the vibratory compactor was 1.767kN, and the frequency of vibration was 44 Hz. With the 225 mm × 225 mm compaction plate, the peak cyclic normal stress σ_{cyc} applied on the surface of soil was 34.9 kN/m². It should be mentioned that the distribution of contact pressure between the foundation and the cohesionless soil varies with the stiffness of the footing. If the footing was perfectly rigid, the static contact pressure on the footing increases from zero at the edge to a maximum at the center.

Chapter 4

BACKFILL CHARACTERISTICS

This chapter introduces the properties of backfill. The interface characteristics between the backfill and the walls of soil bin are discussed. The following sections included: (1) backfill properties; (2) reduction of wall friction.

4.1 Backfill Properties

Air-dry Ottawa silica sand (ASTM C-778) was used as the backfill material for all experiments. Physical properties of Ottawa sand are listed in Table 4.1. Grain-size distribution of the backfill is shown in Fig. 4.1. Major factors considered in choosing Ottawa sand as backfill material are summarized as follows.

1. Its round shape, which avoids the effect of angularity of soil grains.
2. Its uniform distribution of grain size (coefficient of uniformity $C_u = 1.78$), which avoids the effects due to soil gradation.
3. High rigidity of solid grains, which reduces possible disintegration of soil particles under loading.
4. Its high permeability, which allows fast drainage and therefore reduces water pressure behind the wall.

To establish the relationship between unit weight of backfill γ and its internal friction angle ϕ , direct shear tests were conducted. The shear box used has a square (60 mm \times 60 mm) cross-section, and its arrangement is shown in Fig. 4.2. Before shearing, Ottawa sand was air-pluviated into the shear box. Details of the technique to control soil density are discussed in section 5.1.

Chang (2000) established the relationship between the internal friction angle ϕ and unit weight γ of Ottawa sand as shown in Fig. 4.3. It is obvious from the figure

that soil strength increases with increasing soil density. For the air-pluviated backfill, the empirical relationship between soil unit weight γ and ϕ angle was formulated as follows

$$\phi = 6.43\gamma - 68.99 \quad (4.1)$$

where

ϕ = angle of internal friction of soil (degree)

γ = unit weight of soil (kN/m³)

Eq. (4.1) is applicable for $\gamma = 15.45 \sim 17.4$ kN/m³ only.

For compacted backfill, the following relationship can be formulated.

$$\phi = 7.25 \gamma - 79.55 \quad (4.2)$$

Eq. (5.2) is applicable for $\gamma = 15.8 \sim 17.05$ kN/m³ only.

4.2 Reduction of Wall Friction

To decrease the boundary effect for earth pressure tests, the shear stress between the backfill and wall should be minimized to nearly frictionless. To reduce the friction between wall and soil, a lubrication fabricated layer with plastic sheets was furnished for all earth pressure experiments. Two types of plastic sheeting, one thick (0.152 mm-thick) and two thin (0.009 mm-thick) plastic sheets, were adopted to reduce the interface friction. All plastic sheets were hung vertically on each sidewall before the backfill was deposited as shown in Fig. 4.4.

Multiple layers of thin plastic sheets (without any lubricant) were used by McElroy (1997) for shaking table tests of geosynthetic reinforced soil (GRS) slopes. Burgess (1999) used three thin plastic sheets to reduce side wall friction in full-scale GRS wall tests. The wall friction angle was approximately 15° as determined by the shear box tests. In this study, two thin and one thick plastic sheets were adopted for the experiments. The friction angle developed between the plastic sheets and steel sidewall was determined by the sliding block test. A schematic diagram and a

photograph of the sliding block test proposed by Fang et al. (2004) are illustrated in Fig. 4.5 and Fig. 4.6. The sidewall friction angle δ_{sw} for the sliding block test was determined using basic principles of physics. Fig. 4.7 shows the variation of friction angle δ_{sw} as a function of the normal stress σ for the plastic sheet method (1 thick + 2 thin sheeting) used in this study. The measured friction angle with this method was about 7.5° . It is clear in Fig. 4.7 that the interface friction angle δ_w is nearly independent of the applied normal stress σ on the interface. This constancy is an important advantage in establishing the input soil properties for analytical models that might be used to analyze the experimental results. For all experiments in this paper, the lubrication layer was applied on four walls as indicated in Fig. 4.4. The plastic sheets not only can help to reduce the friction angle between the wall and the backfill. The plastic sheets can also help to reduce the reflection of elastic waves transmitted to the soil-wall boundaries during compaction.

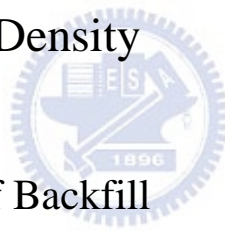


Chapter 5

EXPERIMENTAL RESULTS FOR LOOSE SAND

This chapter introduces the distribution of soil density, the horizontal and vertical earth pressure in a loose cohesionless backfill. For all experiments, the surface of backfill was horizontal and the backfill was filled up to 1500 mm above the base of the soil bin.

5.1 Control of Soil Density



5.1.1 Air Pluviation of Backfill

To achieve a uniform soil density in the backfill, Ottawa sand was deposited by air-pluviation method into the soil bin. The air-pluviation method had been widely used to reconstitute laboratory sand specimens. Rad and Tumay (1987) reported that pluviation was the method that provided reasonably homogeneous specimens with a desired relative density. Lo Presti et al. (1992) reported that the pluviation method could be performed for greater specimens in less time. In Fig. 5.1, the soil hopper that lets the sand pass through a calibrated slot opening at the lower end was used for the spreading of sand. Air-pluviation of the Ottawa sand into soil bin is shown in Fig. 5.2.

Das (1994) suggested that the relative density of 15~50 % is defined as a loose condition. Ho (1999) established the relationship among slot opening, drop height, and soil density as shown in Fig. 5.3. The drop height of 1.0 m and hopper slot-opening of 15 mm were selected to achieve the loose backfill ($D_r = 34\%$) for

testing in this study.

5.1.2 Uniformity of Soil Density

To observe the distribution of soil density in the soil bin, measurements were made. The soil density cup made of acrylic is illustrated in Fig. 5.4 and Fig. 5.5. During the preparation of soil specimen, density cups were embedded in the soil mass at different elevations and different locations as shown in Fig. 5.6 and Fig. 5.7. The four steps of the soil density control test for a loose sand are shown in Fig. 5.8 (a) to (d). After the soil had been filled up to 1.5 m from the bottom of the soil bin, the density cups were dug out from the soil mass carefully. Fig. 5.8 (a) shows the density cup was placed in the soil bin and Fig. 5.8 (d) shows the weight of the cup and soil was measured with an electrical scale. Based on the measurements, the distribution of soil density with depth for loose sand is shown in Fig. 5.9. The mean relative density was $D_r = 34.1\%$ with a standard deviation of 2.4%. The test results were in fairly good agreement with the data reported by Chen (2003). The backfill achieved with the air-pluviation method was obviously loose, $D_r = 15\sim 50\%$ as suggested by Das (1994).

5.2 Stresses in Loose Sand

For comparison purposes, at the beginning of this study, experiments were conducted to investigate the stresses in an uncompacted backfill. Fig. 5.10 (a) shows the locations of soil pressure transducers in the soil mass to measure σ_v . Fig. 5.10 (b) illustrates the locations of soil pressure transducers in the soil mass to measure σ_h . The method to confirm depth of the SPT in the soil mass is shown in Fig. 5.11. After the backfill had been filled up to 1.5 m thick, the vertical earth pressure σ_v measured with the SPTs was illustrated in Fig. 5.12 (a). In the figure, the vertical pressure σ_v increased linearly with increasing depth. The test data were in fairly good agreement with the σ_v estimated traditional equation $\sigma_v = \gamma z$, where γ is the unit weight of

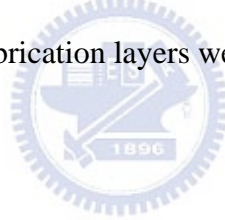
backfill. The distribution of horizontal earth pressure σ_h in the soil mass is shown in Fig. 5.12 (b). In the figure the horizontal pressure σ_h profile induced by the 1500 mm-thick loose fill was approximately linear. Jaky's equation slightly overestimated the horizontal earth pressure. Mayne and Kulhawy (1982), Mesri and Hayat (1993) reported that Jaky's equation is suitable for backfill in its loosest state. From a practical point of view, it may be concluded that for a loose backfill, the vertical and horizontal earth pressures in the soil mass can be properly estimated with the equation $\sigma_v = \gamma z$ and Jaky's equation, respectively.



Chapter 6

VARIATION OF SURFACE SETTLEMENT AND SOIL DENSITY DUE TO COMPACTION

This chapter introduces the variation of surface settlement and soil density due to compaction. For all experiments, the height of backfill was 1500 mm and the surface of the backfill was horizontal. Before compaction the backfill was loose and the initial relative density of the loose sand was 34 %. To reduce the friction between the soil and the four walls, the lubrication layers were applied at the side-wall interfaces.



6.1 Pilot Tests

To establish the program for testing, pilot tests were executed.

Fig. 6.1 shows the major cross-section in this study to measure the surface settlement, change of soil density, earth pressures after compaction. The longitudinal axis of the compactor (Fig. 3.4) was placed forward the model wall or end wall.

The testing procedures of point compaction were introduced as follows:

1. Before compaction, the loose backfill ($D_r = 34\%$) was filled with the air-pluviation method.
2. After the entire loose backfill had been filled, the vibratory compactor was placed at the center of the soil bin as shown in Fig. 1.1.
3. The soil mass was compacted for 5 seconds first, then remove the compactor and measure the surface settlement profile. Fig. 6.2 illustrates the measurement of surface settlement after the compaction.

4. Compacting the backfill, remove the compactor and measuring the surface settlement at $t = 10, 20, 40, 80, 160, 320$ and 640 seconds.

Fig. 6.3 shows the measured surface settlement versus the compaction time. In the figure, the surface settlement increased rapidly after first 20 seconds of compaction. As the compaction time increased, the rate of surface settlement increased slowly. Based on the tests data, a hyperbolic relationship function of the surface settlement versus the compaction time can be established as shown in Fig. 6.3. In the figure, the data points obtained from tests 0602, 0604 and 0609 indicated that the test results were quite reproducible. Based on the test results, the hyperbolic model was established to estimate the surface settlement S as a function of compaction time. The relationship can be expressed as:

$$S_{(t)} = \frac{t}{0.7348 + 0.0238t} \quad (6.1)$$

where

S = surface settlement (mm)

t = compaction time (s)



The asymptote of the hyperbolic model was $S_{\max} = 42$ mm. Table 6.1 shows that the S_{\max} was divided into five equal parts and their corresponding compaction time was assumed. The effects of compaction on the fill after 7, 20, 46 and 123 seconds of compaction were discussed in the following sections.

6.2 Surface Settlement due to Compaction

The surface settlements profiles measured after 7, 20, 46, and 123 seconds of compaction were shown in Fig. 6.4. After the 7 seconds of the compaction, the average settlement was approximately 21 mm (Table 6.2). The surface settlement was about 9.3% of the width of the vibratory compactor ($S/B = 9.3\%$). It is clear in Fig. 6.4 that the amount of surface settlement increased with increasing compaction time.

After 123 seconds of vibratory compaction, the settlement measured was approximately 40.5 mm. The settlement / width ratio has increased to $S/B = 18\%$. Fig.

6.5 shows the surface settlement after 123 seconds of vibratory compaction.

6.3 Density Change due to Compaction

Before compaction, the loose backfill (34 %) was prepared with the air-pluviation method with the drop height of 1.0 m and a hopper slot-opening of 15 mm. The change of soil density was induced by the vibratory compaction. To investigate the change of soil relative density in the soil bin, many soil density cups were embedded in the backfill to measure the local densities at different locations. To constitute the contours of density change, density cups were buried closely in the soil mass at different elevations as shown in Fig. 6.6. Fig. 6.7. shows the locations of soil density cups placed at the same elevation. After the desired compaction time, the soil density cups were dug out from the soil mass and their weights measured carefully.

The distribution of relative density after 7 seconds of point compaction is shown in Fig. 6.8. To visually observe the trend of the change of the relative density, the Software Surfer 8.0 was used. By using the Software Surfer 8, the values of D_r at grid points were converted into a Grapher Grid file. The Grapher Grid file included the test data of relative density. Opening the file with the program Software Grapher 7, the contours of the relative density after 7 seconds of compaction can be obtained as illustrated in Fig 6.9. The detail operation of the Software Surfer 8 and Grapher 7 are described in Appendix B. The distribution of relative density after the 20, 46 and 123 seconds of compaction measured at grid points are shown in Appendix B.

Before compaction, the backfill has a uniform relative density of 34 %. In Fig. 6.9, it is obvious that the soil density became quite dense ($D_r = 51$ %) under the vibratory compactor, and the soil density decreased gradually with the increasing distance from the compactor. Right below the compactor, the relative density increased from 34 % to 51 %, the effects of vibratory compaction on the soil density were quite obvious. As the compaction time increased to 20, 46, and 123 seconds, more compaction energy was transmitted to the soils.

The maximum relative densities measured below the compactor were 51 %, 61 %, 68 %, and 70 %, after 7, 20, 46 and 123 seconds of compaction, respectively. It can also be observed in Fig. 6.9 to Fig 6.12 that the depth of the $D_r = 36$ % contour increased with increasing time of compaction (see Table 6.2). Fig. 6.13 shows the relationship between dry unit weight and compaction time in this study. The peak relative density in the soil was increased with increasing time of compaction.

Fig. 6.14 shows the comparison of distribution of soil unit weight after compaction. Table 6.3 listed the reason about the difference from the NCTU model wall tests and the field tests.



Chapter 7

VARIATION OF σ_v DUE TO COMPACTION

This chapter reports experimental results regarding the variation of the vertical earth pressures in the soil mass due to compaction. The $\Delta\sigma_v$ had been carefully measured with soil pressure transducers embed in the soil mass. The change of vertical earth pressure is defined as the difference of σ_v measured before and after compaction. The loose ($D_r = 34\%$) Ottawa sand with the unit weight γ of 15.6 kN/m^3 was prepared as the backfill material before compaction.

7.1 Distribution of Vertical Earth Pressure after Compaction

7.1.1 Testing procedure

The testing procedures to investigate the change of vertical earth pressure, are introduced as follows:

1. Before compaction, the loose backfill ($D_r = 34\%$) was prepared with the air-pluviation method. With the filling of the Ottawa sand, the SPTs were placed at the desired locations. Fig. 7.1 shows the location of soil pressure transducers (SPT) embedded in the soil mass below the center of the compactor.
2. After the 1.5m-thick loose backfill had been filled, the vibratory compactor was placed at the center of the soil bin as shown in Fig. 1.1.

3. The soil mass was compacted for $t = 7$ seconds, and then the compactor was removed. In the range of 5 to 10 seconds after the compactor removed, the earth pressure below the compactor was recorded. The σ_v in the soil mass was monitored by soil pressure transducers placed in the backfill.
4. Repeat step 3 for $t = 20s, 46s$ and $123s$.

7.1.2 Test results

Fig. 7.2 shows the distributions of vertical earth pressure under the compactor after compaction. Before compaction, the measured σ_v increased with increasing depth. The vertical overburden pressure can be properly estimated with the equation $\sigma_v = \gamma z$. In Fig. 7.2 the vertical earth increased after 7 seconds of compaction. Is this $\Delta\sigma_v$ increase a result of γ increase due to compaction? It can be observed in Fig. 7.2 that, as compared with the $\sigma_v = \gamma z$ for $D_r = 70\%$, the $\Delta\sigma_v$ was much greater than the vertical increase due to the increase of γ . At the depth of 100mm, after 123 seconds of compaction, in soil unit weight increased from 15.6 to 16.5 kN/m³.

Fig. 7.3 shows that the extra vertical stress $\Delta\sigma_v$ induced by the 7, 20, 46 and 123 seconds of compaction. It is obvious from the figure that the compaction-influenced zone extended from the compacted surface to the depth of approximately 600 ~ 800 mm. Based on the test results, the zone to measure $\Delta\sigma_v$ was determined.

7.2 Change of Vertical Earth Pressure due to Compaction

To observe the change of vertical earth pressure after compaction. SPTs were buried in the soil mass at different elevations as shown in Fig. 7.4. The location of SPTs placed on the backfill at the same elevation was illustrated in Fig. 7.5 and Fig. 7.6. The of SPT was positioned primarily from the surface to the depth of 600 mm. Based on the measurement of σ_v and σ_h in the soil mass, it is hoped that mechanism of soils under compaction could be explored.

The change of vertical earth pressure after 7 seconds of compaction at the same

spot measured at grid points is shown in Fig. 7.7. The $\Delta\sigma_v$ measured after 20, 46 and 123 seconds of compaction are shown in appendix C. Fig. 7.8, Fig. 7.9, Fig. 7.10 and Fig. 7.11 show the contours of $\Delta\sigma_v$ after 7, 20, 46 and 123 seconds of compaction. In the figures, it is obvious that the peak $\Delta\sigma_v$ (3.60, 3.99, 4.44, 4.96, kN/m^2) increased as the compaction time increasing. This is because more compaction energy was transmitted to the soil.

After the removal of the compactor, the residual stress in the soil mass was induced by the vibratory compaction. The point of peak $\Delta\sigma_v$, as the compaction time increased, has moved downward slightly from the depth of 250 mm to the depth of 350 mm.

To compare with the elastic solution (section 2.4.2), Fig. 7.12 shows the distribution of $\Delta\sigma_v$ in the soil mass due to a surface square loading q . It is obvious in the figure that the influenced zone was nearly 500 mm. In Fig. 7.12, the peak $\Delta\sigma_v$ zone is located right below the surface static loading. However, in Fig. 7.11, the peak residual $\Delta\sigma_v$ zone is located about 350 mm below the vibratory compactor, and the residual $\Delta\sigma_v$ might below the compactor is less than 0.5 kN/m^2 .

Chapter 8

VARIATION OF σ_h DUE TO COMPACTION

This chapter reports experimental results regarding the variation of the horizontal earth pressure due to compaction and the mechanism of soil during compaction. The variation of horizontal earth pressure had been carefully measured with soil pressure transducers embedded in the soil mass. The change of horizontal earth pressure $\Delta\sigma_h$ was defined as the horizontal earth pressure measured before and after compaction. A loose ($D_r = 34\%$) Ottawa sand with a unit weight γ of 15.6 kN/m^3 was prepared as the backfill material before compaction.

8.1 Distribution of Horizontal Earth Pressure after Compaction

The location of soil pressure transducers (SPT) arranged in the backfill under the compactor is illustrated in Fig. 8.1. The horizontal earth pressure was placed by soil pressure transducers mounted in the soil mass.

Fig. 8.2 shows the distributions of horizontal earth pressure σ_h under the compactor before and after 7, 20, 46 and 123 seconds of compaction. Test data indicate that before compaction the horizontal earth pressure σ_h can be approximated with the Jaky's equation $\sigma_h = K_o \gamma z$ ($K_o = 1 - \sin \phi$).

Before compaction, the loose ($D_r = 34\%$) Ottawa sand has an unit weight γ of 15.6 kN/m^3 and the soil friction angle $\phi = 31^\circ$. After compaction, it is clear in the figure that the vibratory compaction results some extra horizontal residual stress. And

the lateral stress measured near the top of the backfill was close to the passive earth pressure estimated with the Rankine theory.

Fig. 8.3 shows that the extra horizontal stress $\Delta\sigma_h$ was induced by 7, 20, 46 and 123 seconds of compaction. It is obvious from the figure that the compaction-influenced zone extended from the compacted surface to the depth of approximately 600 mm. Based on the test results, the zone for measuring of $\Delta\sigma_h$ was determined to be from $z = 0$ to $z = 600$ mm.

8.2 Change of Horizontal Earth Pressure due to Compaction

To study the change of horizontal earth pressure due to compaction, measurements were made with soil pressure transducers test. The procedures were similar to the method described in section 7.1. SPTs were buried closely in the soil mass at different elevations at the same cross-section as shown in Fig. 8.4. The location of SPTs placed on the backfill at the same elevation was illustrated in Fig. 8.5 and Fig. 8.6. Based on the test results of section 8.1, the SPTs were positioned from the compacting surface to the depth of 600 mm.

Fig. 8.7 shows the change of horizontal earth pressure $\Delta\sigma_h$ measured at grid points after 7 seconds of the compaction. The change of horizontal earth pressure after 20, 46 and 123 seconds of compaction measured at grid points were reported in appendix D. The Software Sufer 8 was used to draw the $\Delta\sigma_h$ contours. The contours of $\Delta\sigma_h$ after 20, 46 and 123 seconds of compaction were shown in Fig. 8.8, Fig. 8.9, Fig. 8.10 and Fig. 8.11. It was found that the peak $\Delta\sigma_h$ (1.93, 2.41, 3.16, 3.32 kN/m²) increased with increasing compaction time. This is because more compaction energy was transmitted to the soil. The peak $\Delta\sigma_h$ occurred at the depth of 200 mm and the peak $\Delta\sigma_h$ zoned expanded transversely with the increasing compaction time.

As compared with the elastic solution, Fig. 8.12 shows the distribution of $\Delta\sigma_h$ due to a static surface loading q acting on the surface of soil. It is obvious in the

figure that the surcharge influenced zone was approximately 300 mm. In Fig. 8.11 and Fig. 8.12, two high-stress zones can be observed under the surface loading area.

8.3 Mechanism of Soils Under Compaction

The compaction of a cohesionless soil with a vibratory compactor can be simulated with the penetration of a square steel pile driven with a vibratory pile driver as indicated in Fig. 8.13. Base on the penetration of pile theory (section 2.5), the ultimate point resistance q_p in a homogeneous soil can be calculated. For example, after the 123 seconds of vibratory compaction, the measured surface settlement was 40.3 mm. So the overburden pressure at the base of the compactor $q' = 0.62 \text{ kN/m}^2$. Before compaction, the soil unit weight of density was 15.6 kN/m^2 . And the soil friction angle was 31° . In Fig. 2.13, the bearing capacity factor $N_q^* = 60$ was determined. The ultimate point resistance q_p at 123 seconds of compaction is estimated with Eq. 2.12 was 37.44 kN/m^2 . By repeating the above-mentioned procedures, the ultimate load q_p after 7, 20 and 46 seconds of compaction could be estimated as 19.66, 27.14 and 32.92 kN/m^2 , respectively. As the compaction time increasing, the ultimate point resistance q_p increased to the cyclic compacting stress $\sigma_{cyc} = 34.9 \text{ kN/m}^2$ applied on the surface of soil. It is suggested that in the vibratory compaction process, the soil mass will settle until the ultimate load q_p and the cyclic compacting stress σ_{cyc} reached an equilibrium.

Chapter 9

CONCLUSIONS

Based on the vertical and horizontal earth pressure for loose sand and the surface settlement, change of soil density and earth pressures after the vibratory compaction at a point, the following conclusions were drawn.

1. For a loose backfill, the vertical and horizontal earth pressures in the soil mass can be properly estimated with the equation $\sigma_v = \gamma z$ and Jaky's equation, respectively.
2. The compaction of a cohesionless soil with a vibratory compactor can be simulated with the penetration of a square steel pile driven with a vibratory pile hammer. In the compaction process, the soils under the compacting plate settled until the ultimate tip resistance q_p and the cyclic compacting stress σ_{cyc} reached an equilibrium.
3. The depth of the relative density contour ($D_r = 36\%$) increased with increasing time of compaction. The peak relative density in the soil also increased with increasing time of compaction.
4. It was obvious that the peak $\Delta\sigma_v$ (3.60, 3.99, 4.44, 4.96, kN/m^2) and $\Delta\sigma_h$ (1.93, 2.41, 3.16, 3.32 kN/m^2) increased with increasing compaction time. This is because, with increasing compaction time, more compaction energy was transmitted to the soil.
5. After the removal of the compactor, residual stresses in the soil mass were measured due to the vibratory compaction. The point of peak $\Delta\sigma_v$, as the compaction time increased, moved downward slightly from the depth of 250 mm to the depth of 350 mm.

References

1. Bowles, J. E. (1988). *Foundation analysis and design*, 4th Edition, McGraw-Hill Book Co., Singapore, 474.
2. Boussinesq, V. J., (1883), "Application des Potentials a L'Etude de L'Equilibre et due Mouvement des Solides Elastiques," Gauthier-Villars, Paris.
3. Broms, B. (1971). "Lateral earth pressures due to compaction of cohesionless soils." *Proc., 4th Int. Conf. Soil Mech.*, Budapest, 373-384.
4. Broms, B., and Ingleson, I. (1971). "Earth pressures against abutment of a rigid frame bridge." *Geotechnique*, 21(1), 15-28.
5. Bros, B. (1972). "The influence of model retaining wall displacements on active and passive earth pressures in sand." *Proc., 5th European Conf. on Soil Mechanics*, Madrid, 1, 241-249.
6. Burgess, G. P. (1999). "Performance of two full-scale model geosynthetic reinforced segmental retaining walls," MS thesis, Royal Military College of Canada, Kingston, Ontario, 207.
7. Chang, S.Y. (2000). "Effect of backfill density on active earth pressure." Master of Engineering Thesis, Dept. of Civil Engineering, National Chiao Tung University, Hsinchu, Taiwan.
8. Chen, T. J. and Fang, Y. S. (2002). "A new facility for measurement of earth pressure at rest". *Geotechnical Engineering Journal*, SEAGES, Vol. 33. No. 3, December, pp.153-159.
9. Chen (2003). "Earth pressure due to vibratory compaction." Ph.D. dissertation, Department of Civil Engineering, National Chiao Tung University, Hsinchu, Taiwan.
10. Chen, N. C. (2005). "Earth pressure at-rest near a vertical rock face." Master of Engineering Thesis, Dept. of Civil Engineering, National Chiao Tung University, Hsinchu, Taiwan.
11. Cornforth, D. H. (1973). "Prediction of drained strength of sands from relative density measurements." *ASTM Special Technical Publication: 523*, 281-303.
12. Das, B. M. (1994). "Principal of geotechnical engineering." PWS Publishing Company, Boston.
13. Das, B. M. (2004). "Principal of geotechnical engineering." PWS Publishing Company, Boston.
14. Day, R. W. (1998). Discussion of "Earth pressures with sloping backfill." *Journal of Geotechnical and Geoenvironmental Engineering*, ASCE, 124(11), 1152-1153.

15. D'Appolonia, D.J., Whitman, R.V., and D'Appolonia, E.D. (1969). "Sand Compaction with Vibrator Rollers," *Journal of the Soil Mechanics and Foundation Division, ASCE*, Vol. 95, No. SM1, 263 - 284
16. Darwin, G. H. (1883). "On the horizontal thrust of a mass of sand." *Proceedings of the Institution of Civil Engineers*: 71, 351-378.
17. D'Appolonia, D. J., Whitman, R. V., and D'Appolonia, E. (1969). "Sand compaction with vibratory rollers." *Journal of the Soil Mechanics and Foundations Division, ASCE*, 95(SM1), 263-284.
18. Donath, A. D. (1891). "Untersuchungen ueber den erddruck auf stuetzwaende." *Zeitschrift fuer Bauwesen*, Berlin.
19. Duncan, J. M., and Seed, R. B., (1986), "Compaction-Induced Earth Pressures under K_0 -Conditions," *Journal of Geotechnical Engineering, ASCE*, Vol. 112, No. 1, pp. 1-22.
20. Duncan, J. M., Williams, G. W., Sehn, A. L., and Seed, R. B. (1991). "Estimation earth pressures due to compaction." *Journal of Geotechnical Engineering, ASCE*, 117(12), 1833-1847.
21. Dunncliff, J. (1988). *Geotechnical Instrumentation for Monitoring Field Performance*, John Wiley & Sons, Inc., New York.
22. Fang, Y. S., Chen, J. M., and Chen, C. Y. (1997). "Earth pressures with sloping backfill." *Journal of Geotechnical and Geoenvironmental Engineering, ASCE*, 123(3), March, 250-259.
23. Fang, Y. S., Chen, T. J., Holtz, R. D., and Lee, W. F. (2004). "Reduction of boundary friction in model tests." *ASTM Geotechnical Testing Journal*, 27(1), 1-10
24. Ho, Y. C., (1999), "Effects of Backfill Compaction on Passive Earth Pressure," *Master of Engineering Thesis, National Chaio Tung University, Hsinchu, Taiwan.*
25. Holl, D. L., (1940). "Stress transmission in earths." *Proc.High.Res.Board*, Vol.20, pp.709-721.
26. Hou, P. H. (2006). "Design and Construction of NCTU K_A Model Retaining Wall." *Master of Engineering Thesis, Dept. of Civil Engineering, National Chiao Tung University, Hsinchu, Taiwan.*
27. Jaky, J. (1944). "The coefficient of earth pressure at rest." *Journal for Society of Hungarian Architects and Engineers, Budapest, Hungary, Oct.*, 355-358.
28. Johnson, A.W., and Sallberg, J.R. (1960). "Factors That Influence Field Compaction of Soil," *Highway Research Board, Bulletin No. 272.*

29. Lo Presti, D. C. F., Pedroni, S., and Crippa, V. (1992). "Maximum dry density of cohesionless soils by pluviation and by ASTM D 4253-83: A comparative study." *ASTM Geotechnical Testing Journal*, 15(2), 180-189.
30. Matteotti, G. (1970). "Some results of quay-wall model tests on earth pressure." *Proceeding, Institution of Civil Engineers*, 47, 185-204.
31. Mackey, R. D., and Kirk, D. P. (1967). "At rest, active and passive earth pressures." *Proc., South East Asian Conference on Soil Mechanics and Foundation Engineering, Bangkok*, 187-199.
32. Mayne, P. W., and Kulhawy, F. H. (1982). "K_o-OCR relationships in soil." *Journal of Geotechnical Engineering Division, ASCE*, 108(GT6), 851-872.
33. McElroy, J. A. (1997). "Seismic stability of geosynthetic reinforced slopes: A shaking table study." MS thesis, University of Washington, Seattle, 286.
34. Mesri, G., and Hayat, T. M. (1993). "The coefficient of earth pressure at rest." *Canadian Geotechnical Journal*, 30(4), 647-666.
35. Meyerhof, G. G. (1976). "Bearing Capacity and Settlement of Pile Foundations," *Journal of the Geotechnical Engineering Division, American Society of Civil Engineers*, Vol. 102, No. GT3, pp. 197-228.
36. NAVFAC. (1982). *Foundations and earth retaining structures design manual*, Dept. of Navy, DM 7.2, Alexandria, Va.
37. Peck, R. B., and Mesri, G. (1987). Discussion of "Compacted-induced earth pressures under K_o-conditions." *Journal of Geotechnical Engineering, ASCE*, 113(11), 1406-1408.
38. Rad, N. S., and Tumay, M. T. (1987). "Factors affecting sand specimen preparation by raining." *ASTM Geotechnical Testing Journal*, 10(1), 31-37.
39. Rowe, P. W., (1954), "A Stress Strain Theory for Cohesionless Soil with Applications to Earth Pressures At Rest and Moving Walls," *Geotechnique*, Vol. 4, pp. 70-88.
40. Seed, R. B., and Duncan, J. M. (1983). "Soil-structure interaction effects of compaction-induced stresses and deflections." *Geotechnical Engineering Research Report No. UcB/GT/83-06*, Univ. of California Berkeley, CA.
41. Sowers, G. B., and Sowers, G. F. (1961). *Introductory soil mechanics and foundations*, New York: Macmillan, 386.
42. Tzeng, S. H. (2002). "Horizontal Pressures on an Unyielding Wall Due to Strip Loading on Compacted Backfill." *Master of Engineering Thesis*, Dept. of Civil Engineering, National Chiao Tung University, Hsinchu, Taiwan.
43. US NAVY. (1982). "Foundations and earth structures." *NAVFAC Design Manual DM-7.2*. Naval Facilities Engineering Command, U.S. Government Printing Office, Washington, D. C., 60.

44. Vesic, A. S. (1963). "Bearing Capacity of Deep Foundation in Sand." Highway Research Record No. 39, Nation Academy of Sciences, pp. 112-153.
45. Vesic, A. S. (1973). "Analysis of ultimate loads of shallow foundations." Journal of the Soil Mechanics and Foundations Division, 99(SM1), 45-73.
46. Wang, F. J. (2005). "Effect of Adjacent Rock Face Inclination on Earth Pressure At-Rest." Master of Engineering Thesis, Dept. of Civil Engineering, National Chiao Tung University, Hsinchu, Taiwan.
47. Weiler, W. A., and Kulhawy, F. H. (1982). "Factors affecting stress cell measurements in soil." Journal of Geotechnical Engineering Division, ASCE, 108 (GT12), December, 1529-1548.



Table 3.1. Technical Information of the Acentric Motor

Manufacture	Mikasa
Type	KJ75-2P
Power (Watt)	75
Voltage (Volt)	220
Frequency (Hz)	50/60
Vibration Per Minute	3000/3600
Mass (kg)	6.2



Table 4.1. Properties of Ottawa Sand

Shape	Rounded
e_{\max}	0.76
e_{\min}	0.50
G_s	2.65
D_{60}, mm	0.32
D_{10}, mm	0.21
C_u	1.78



Table 6.1. Determination of Compaction Time for Testing with Hyperbolic Model

Expected Surface Settlement	Surface Settlement, S (mm)	Time, t (s)	Compaction Time for Testing (s)
0.2 S_{max}	8.4	7.7	7
0.4 S_{max}	16.8	20.6	20
0.6 S_{max}	25.2	46.3	46
0.8 S_{max}	33.6	123.5	123
S_{max}	42.0	∞	

Table 6.2. Compaction Time with Corresponding Average Settlement

Compaction Time (s)	Surface Settlement, S (mm)	$D_{r,max}$ (%)	Depth of $D_r = 36\%$ contour
7	21.0	51	570
20	29.0	61	1100
46	34.5	68	1100
123	40.3	70	1400

Table 6.3. Compaction between the NCTU's Compaction Tests and D'Appolonia's Field Tests

Item	NCTU	D' Appolonia
Soil	Ottawa Sand	Sand Dune
Compaction	Hand tamper	Vibratory roller
Size	Small (12.1 kg)	Heavy
Method	Point	Area
Energy	Small	Large
Depth influence	0.4m	1.83m
Lift height	1.5m	2.44m



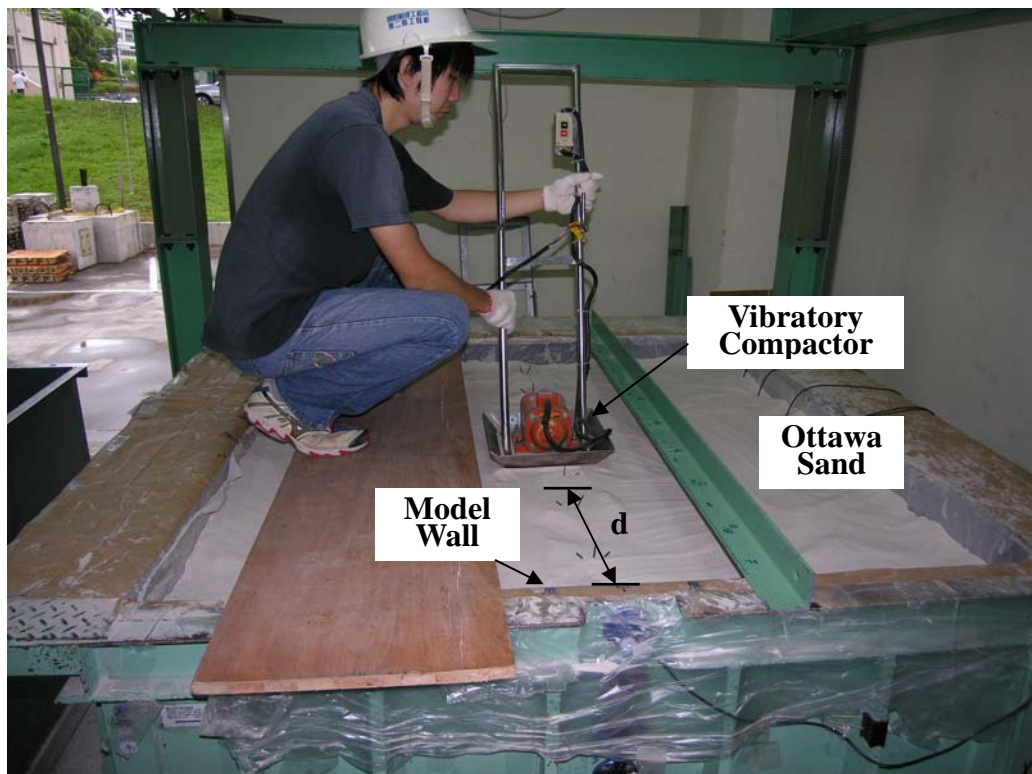


Fig. 1.1. Compaction on the surface of a 1500 mm-thick loose sand





Fig. 1.2. Compaction of backfill using hand tamper (after Day, 1998)



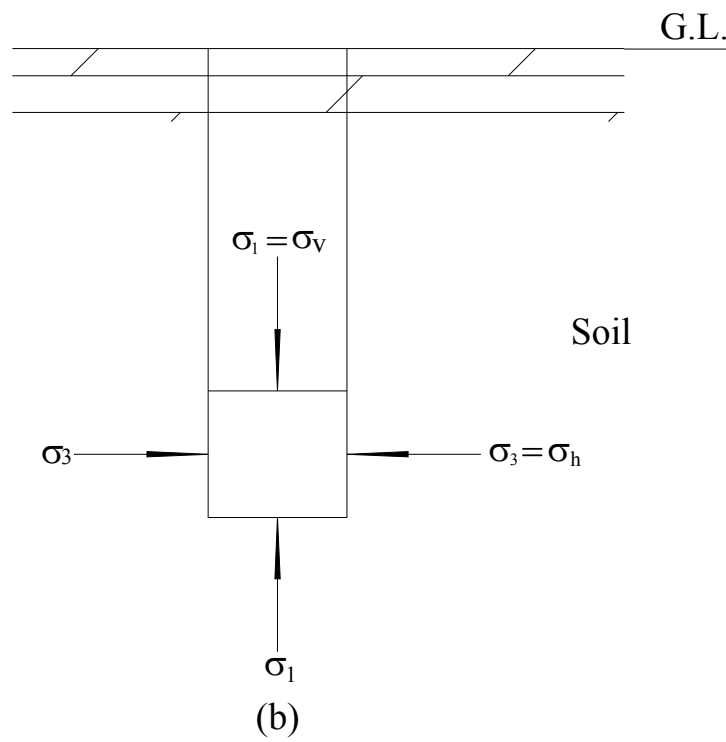
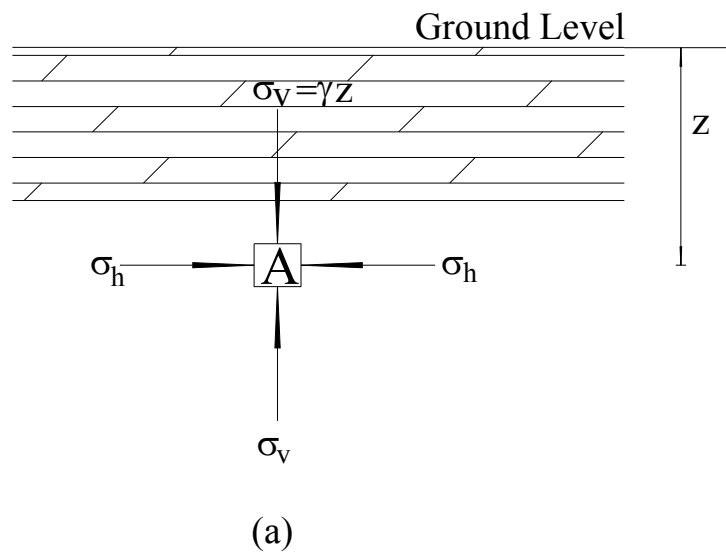


Fig. 2.1. Development of in-situ stresses (after Chen, 2003)

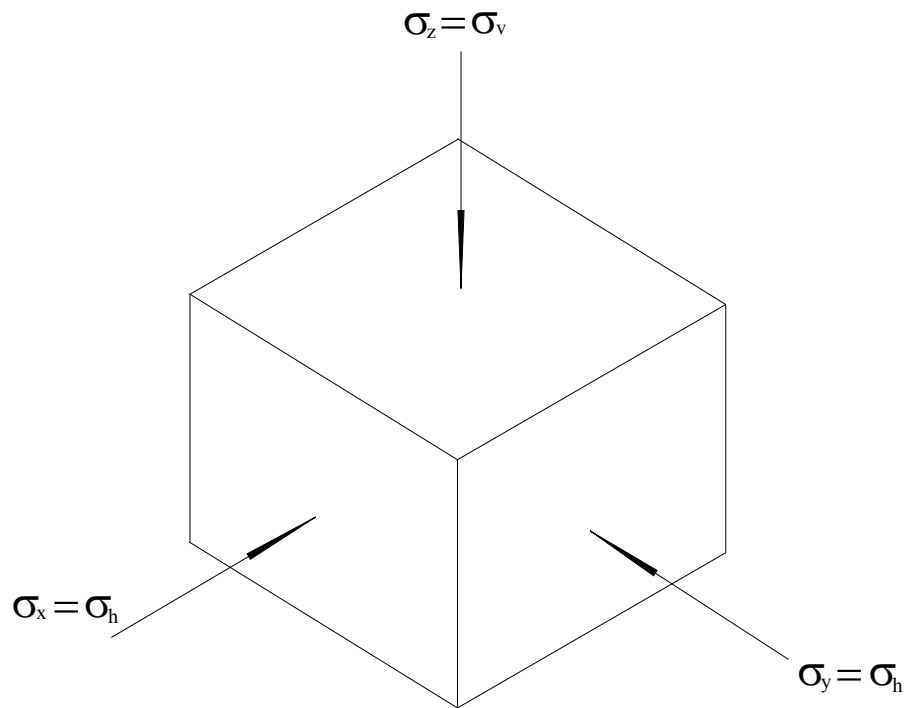


Fig. 2.2. Principal stresses in soil element (after Chen, 2003)



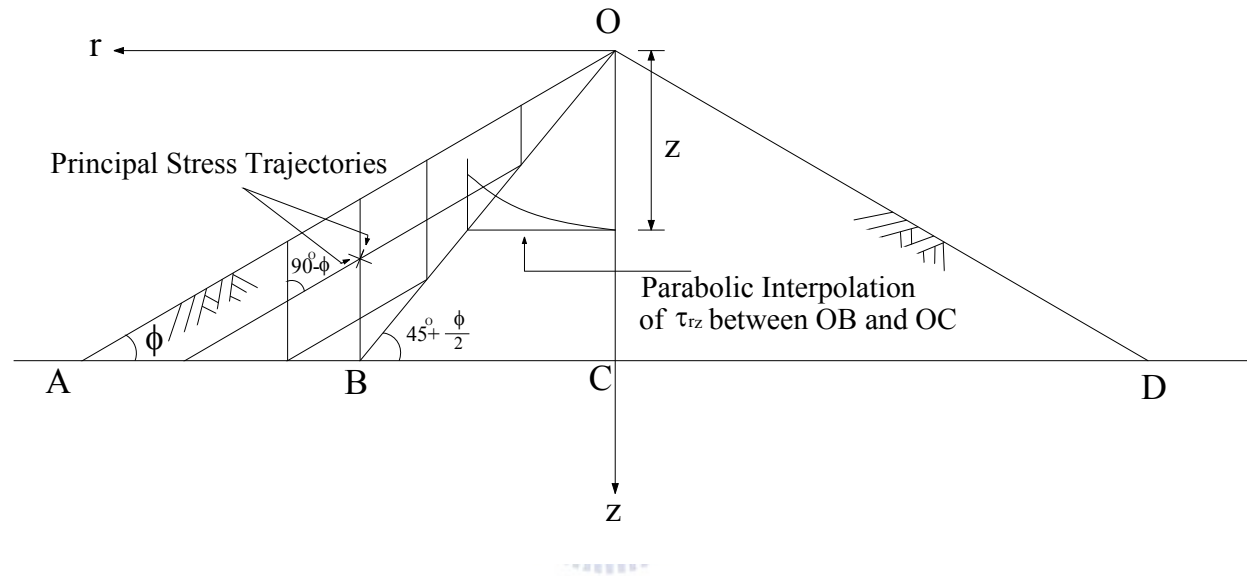


Fig. 2.3. Jaky's formulation of the relationship between K_o on OC and ϕ mobilized in OAB (after Mesri and Hayat, 1993)

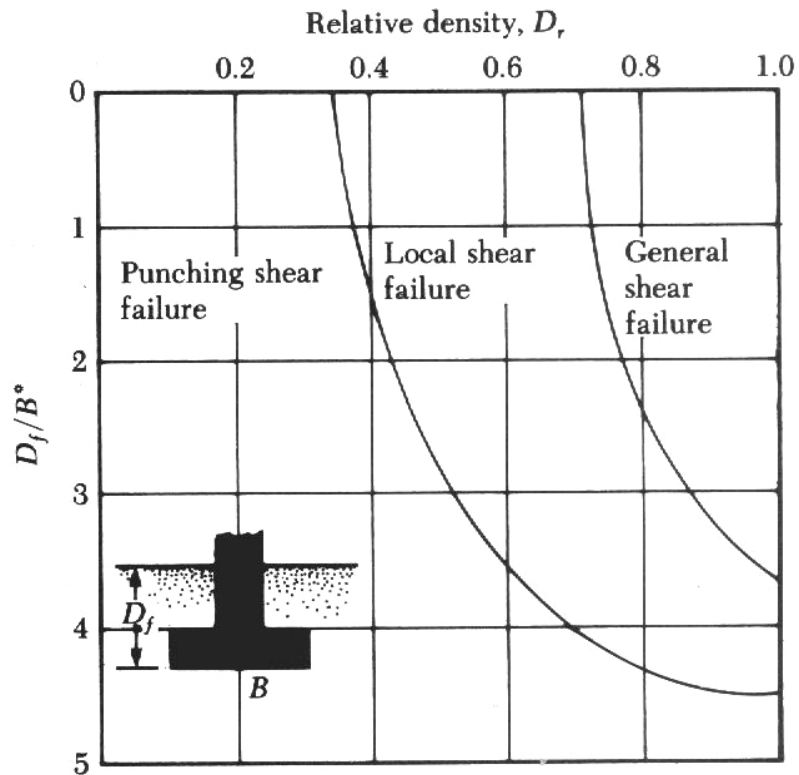


Fig. 2.4. (a) Mode of foundation failure in sand (after Vesic, 1973)

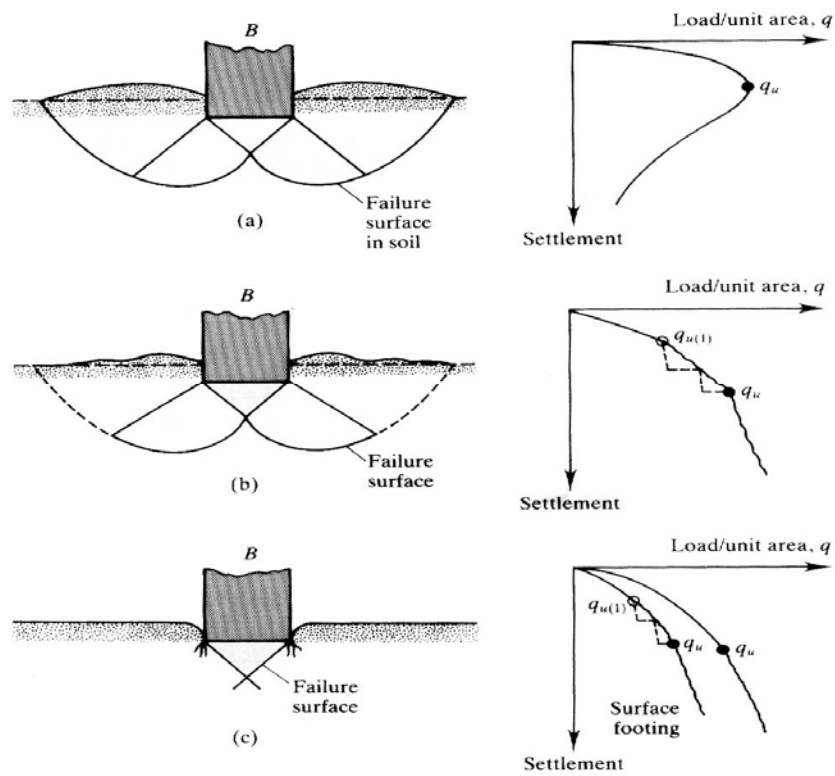


Fig. 2.4. (b) Definition of failure mode (after Vesic, 1973)

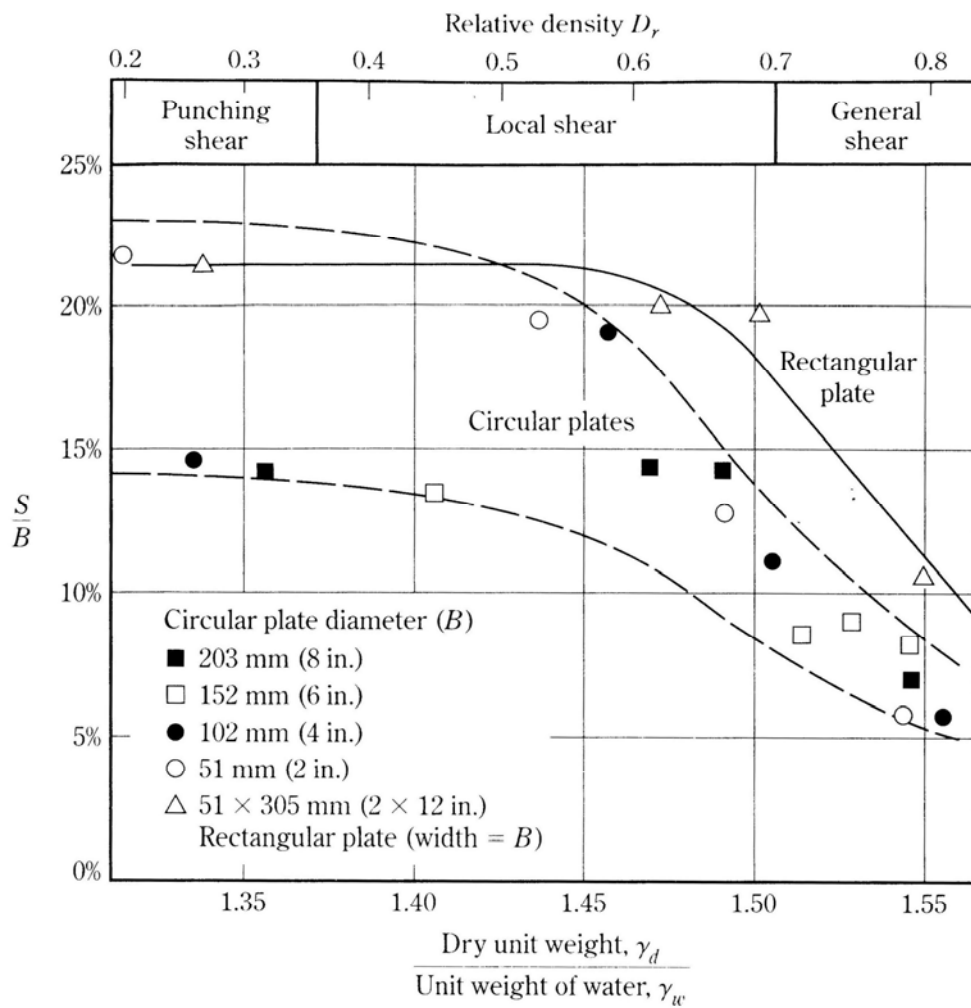


Fig 2.5. Settlement of circular and rectangular plates used to achieve an ultimate load ($D_f/B = 0$) in sand (after Vesic, 1963)

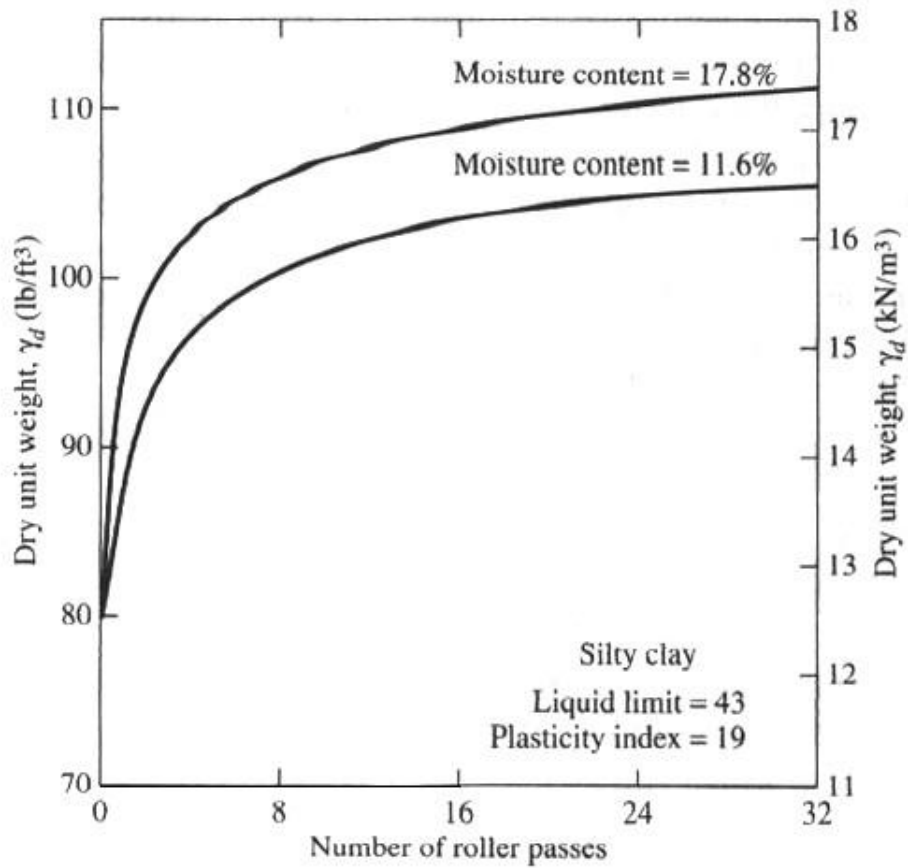


Fig. 2.6. Growth curves for a silty clay - relationship between dry unit weight and number of passes of 84.5 kN three-wheel roller when the soil is compacted in 229 mm loose layers at different moisture contents (after Johnson and Sallberg, 1960)

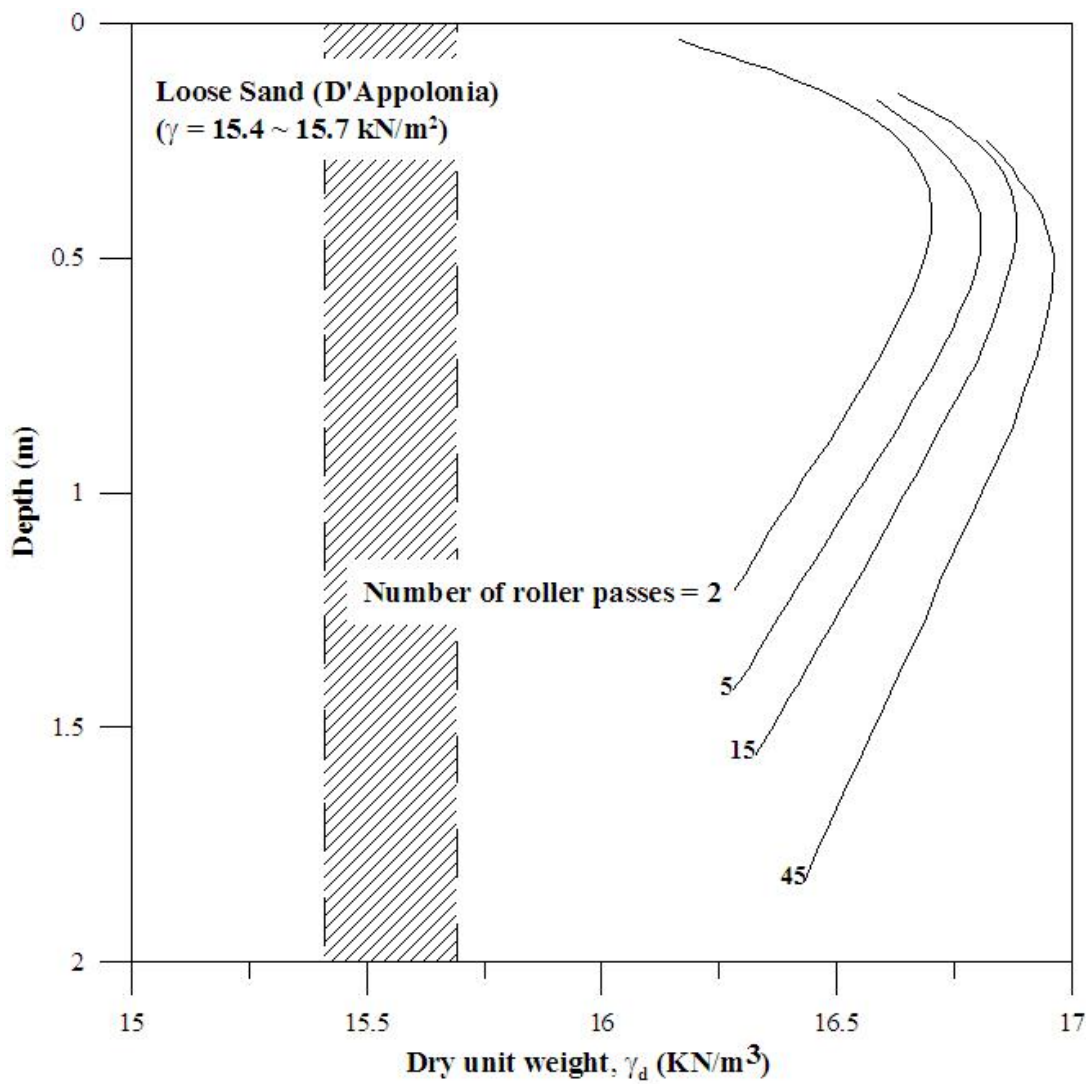


Fig. 2.7. Vibratory compaction of a sand - variation of dry unit weight with number of roller passes; thickness of lift = 2.45 m (after D'Appolonia, et al., 1969)

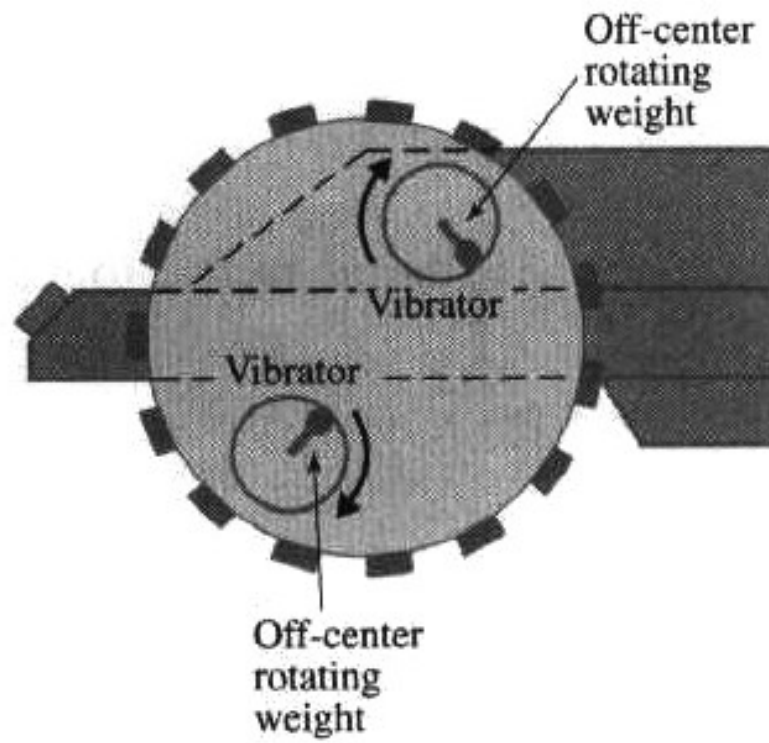


Fig. 2.8. Principles of vibratory rollers (after D'Appolonia, et al., 1969)



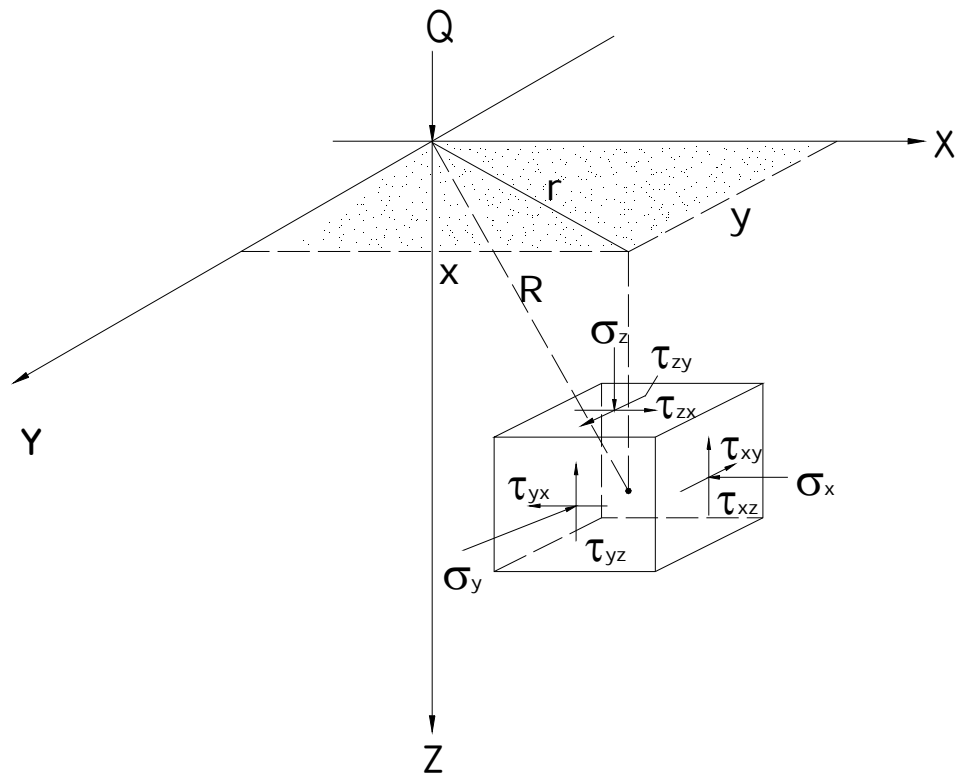


Fig. 2.9. Stresses due to a vertical point load in rectangular coordinates
(after Boussinesq, 1883)

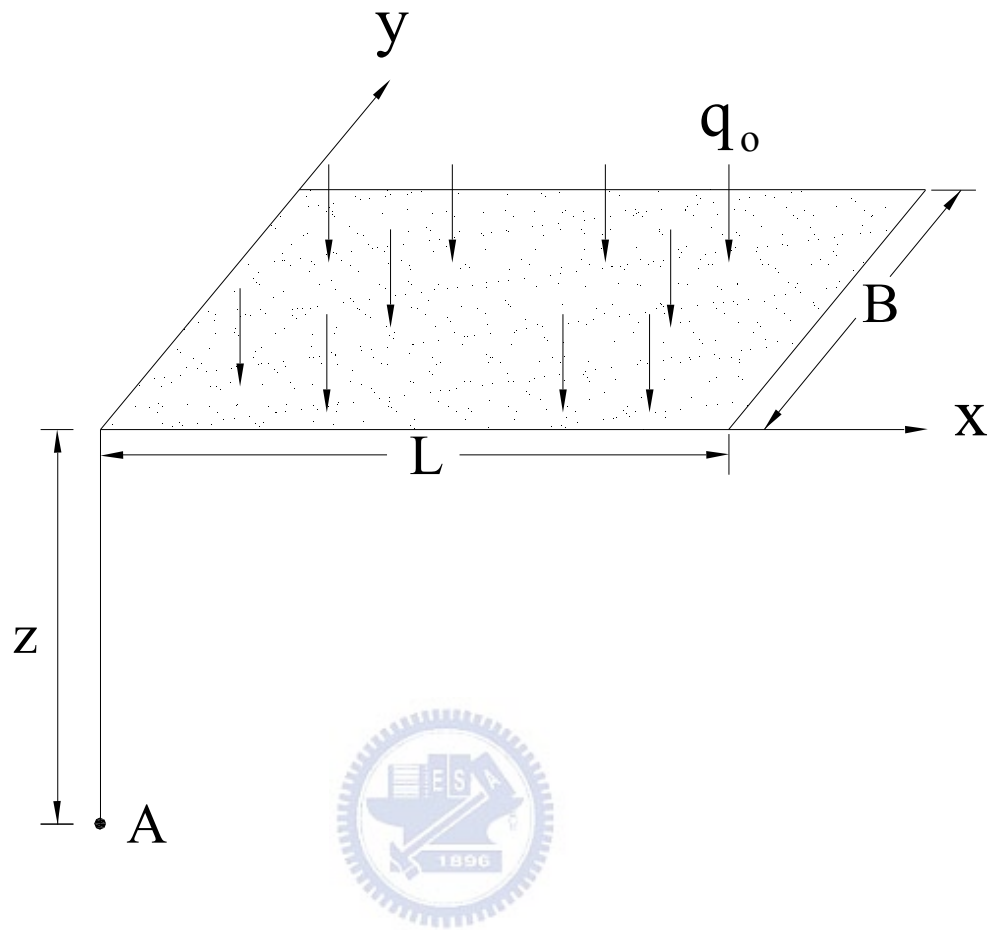


Fig. 2.10. Stresses below the corner of a rectangular loaded area

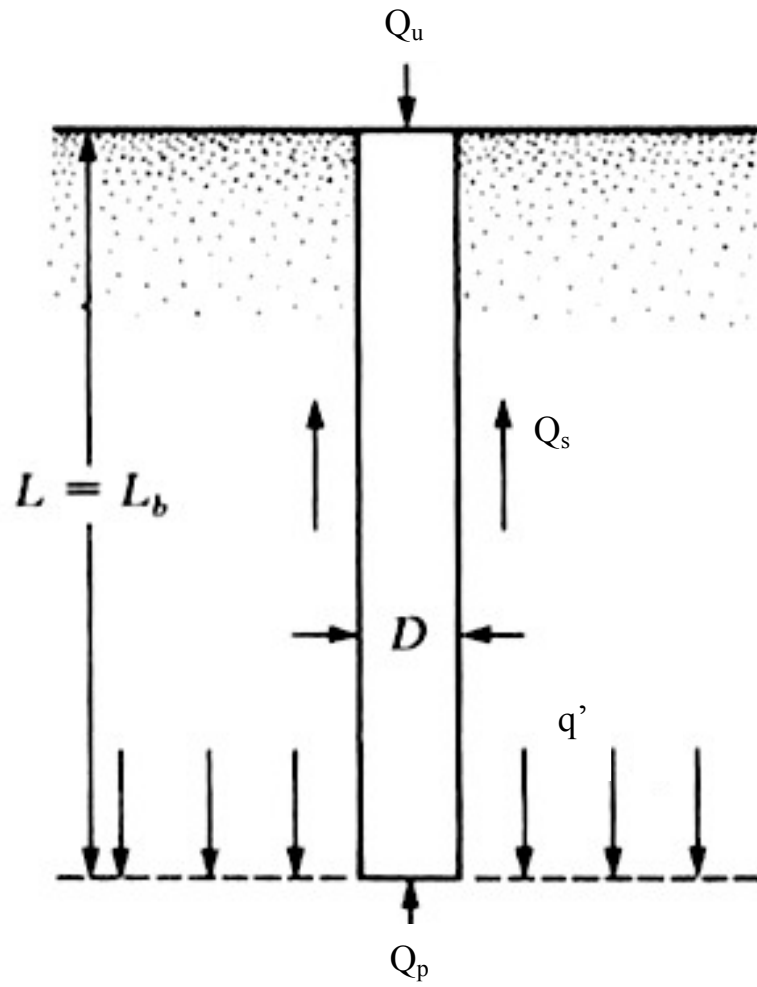


Fig. 2.11. Ultimate load-carrying capacity of pile (after Das, 2004)

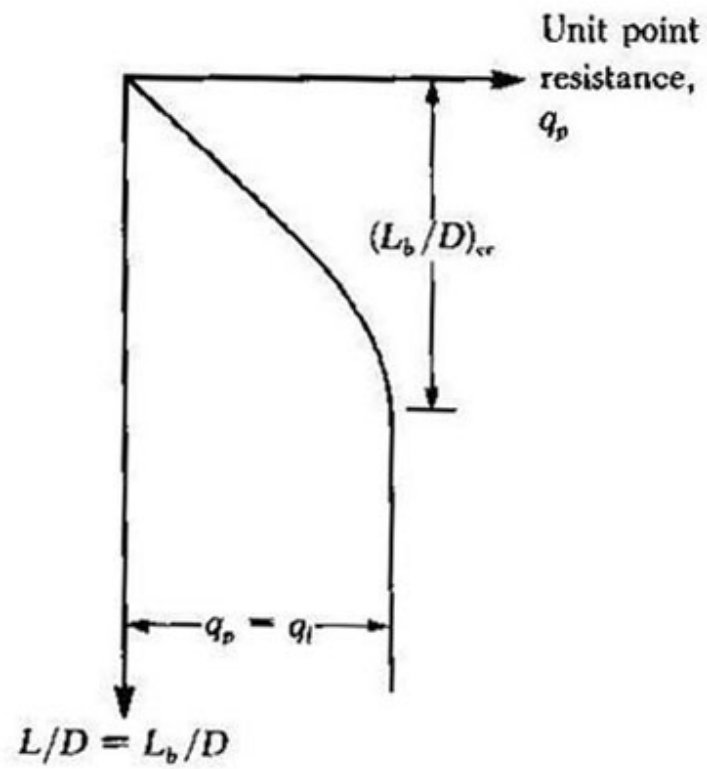


Fig. 2.12. Nature of variation of unit point resistance in a homogeneous sand (after Das, 2004)

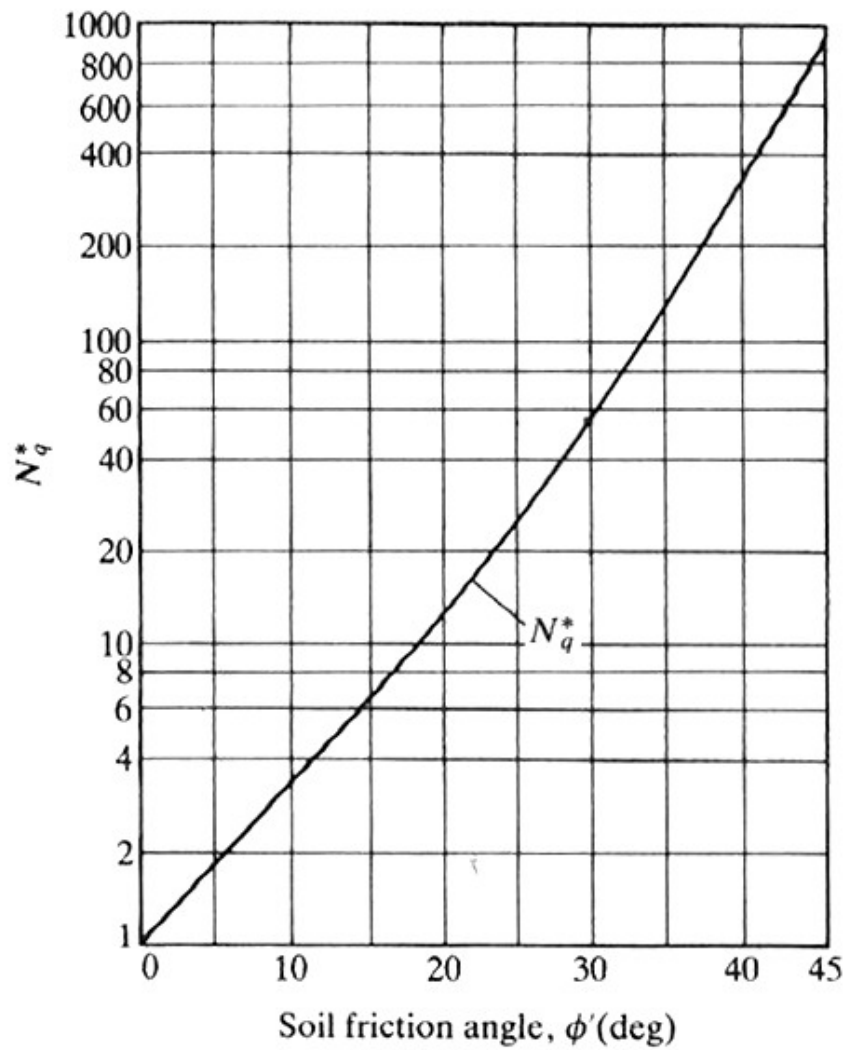


Fig. 2.13. Variation of the maximum values of N_q^* with soil friction with soil friction angle ϕ' (after Meyerhof, 1976)

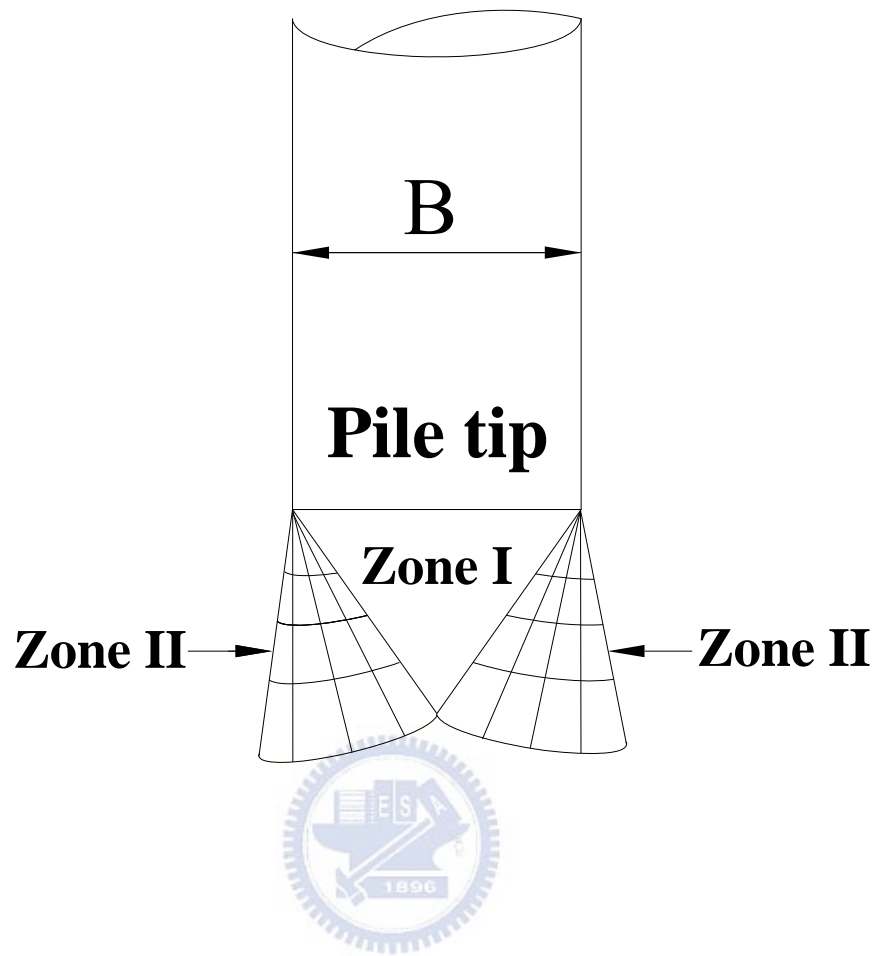


Fig. 2.14. Load transfer mechanism for piles at deep foundation in a punching mode

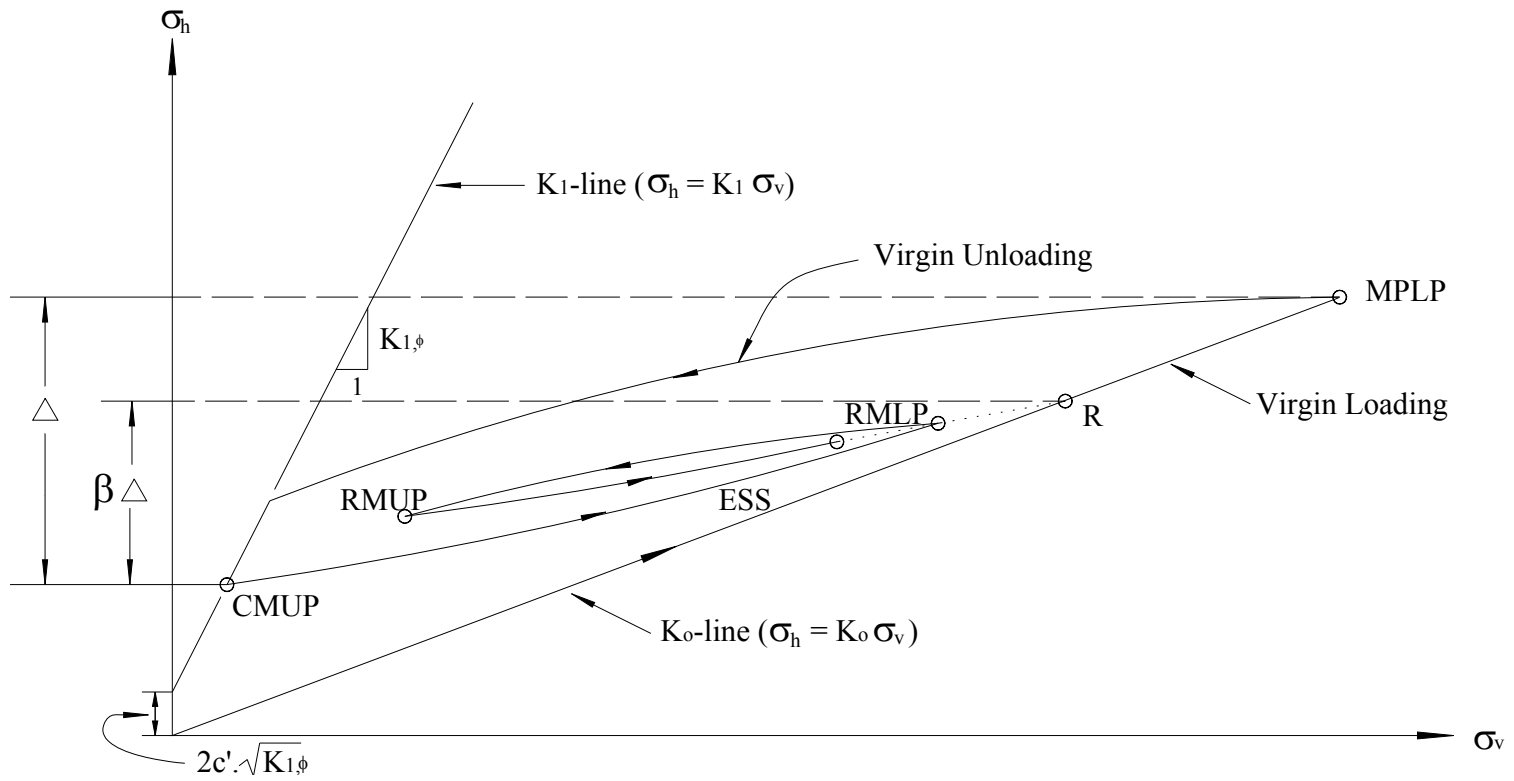


Fig. 2.15. Basic components of hysteretic K_o -loading/unloading model (after Duncan and Seed, 1986)

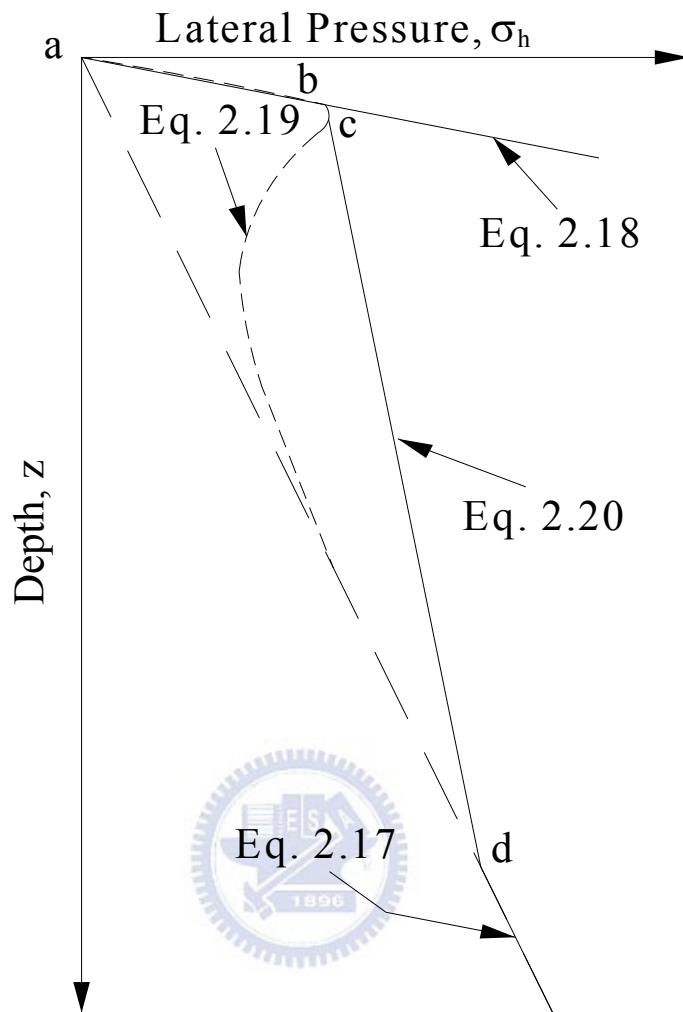


Fig. 2.16. Hand-calculation for estimating σ_h
(after Peck and Mesri, 1987)

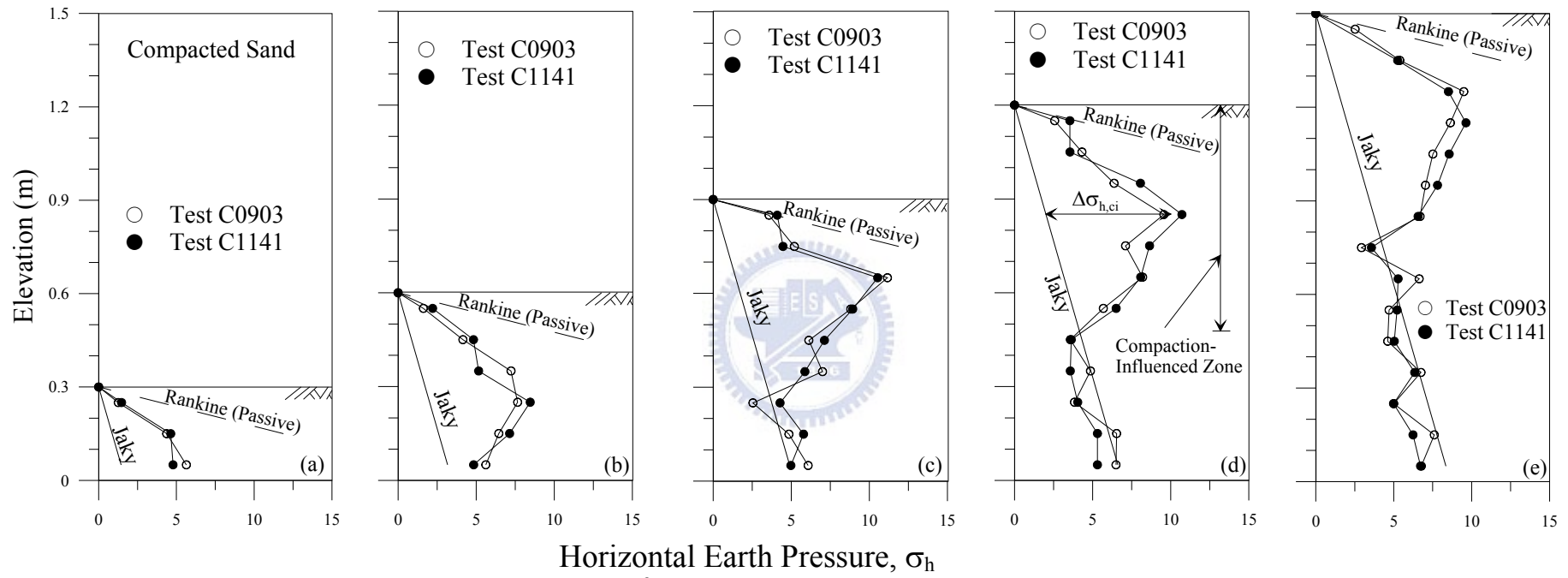


Fig. 2.17. Distribution of horizontal earth pressure after compaction (after Chen, 2003)

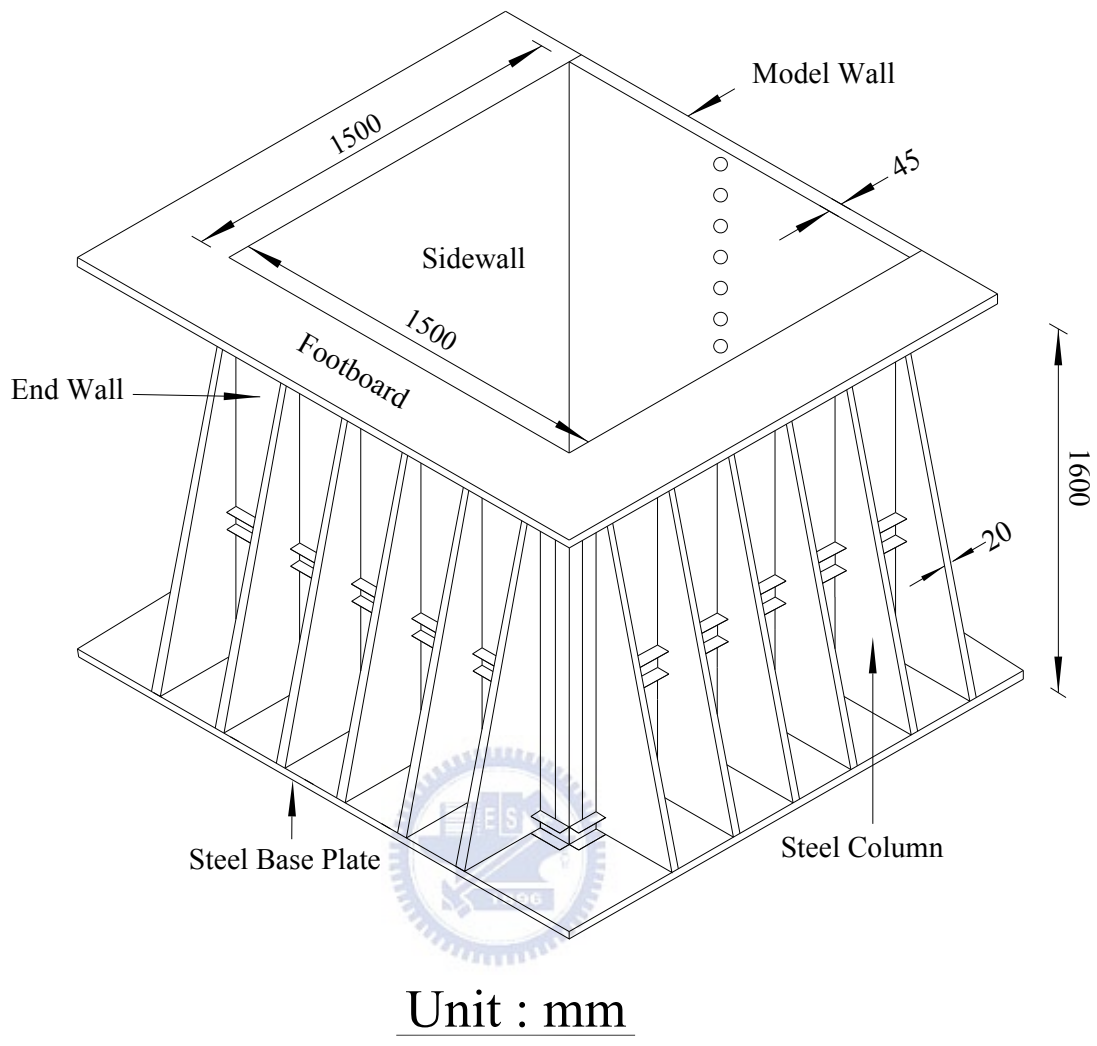


Fig. 3.1. NCTU non-yielding soil bin (after Chen, 2003)



Fig. 3.2. Soil-pressure transducer (Kyowa BE-2KCM17)
(after Chen, 2003)

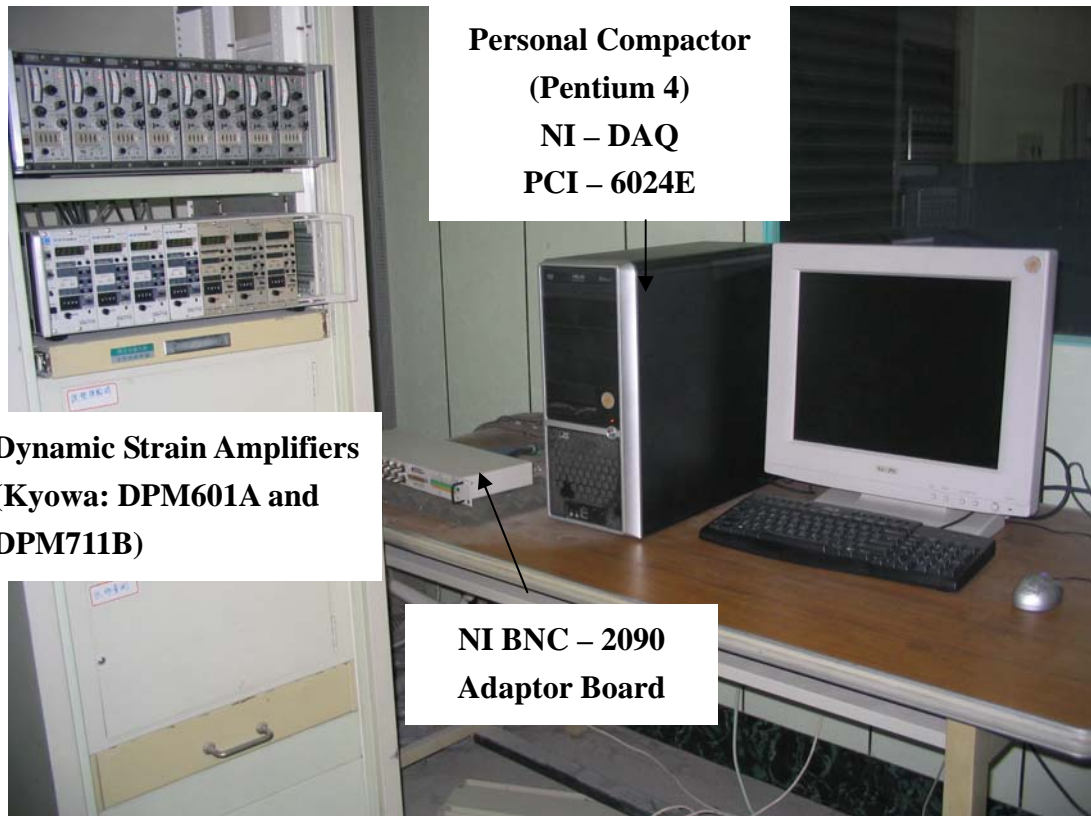


Fig. 3.3. Data acquisition system (after Wang, 2005)

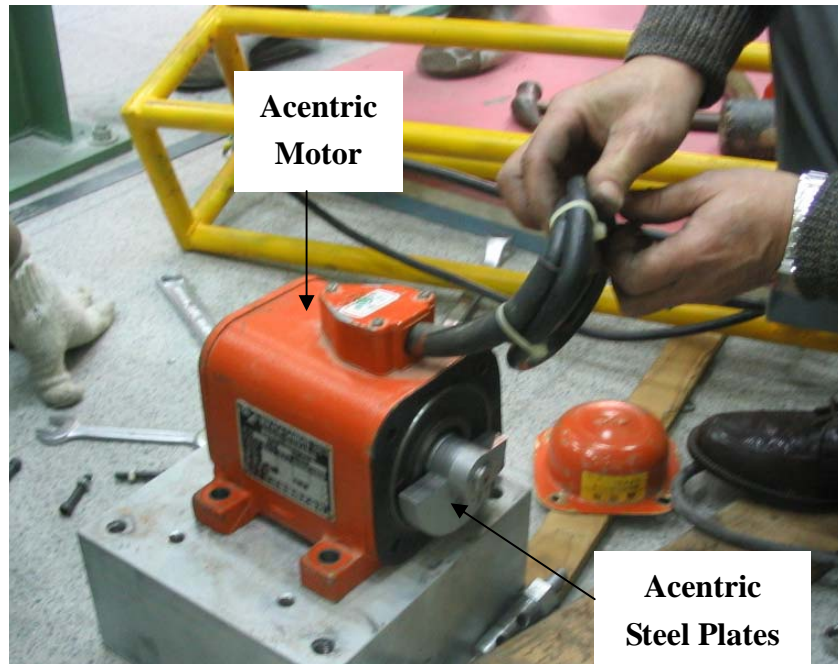


Fig. 3.4. Acentric motors (Mikasa KJ75) (after Wang, 2005)



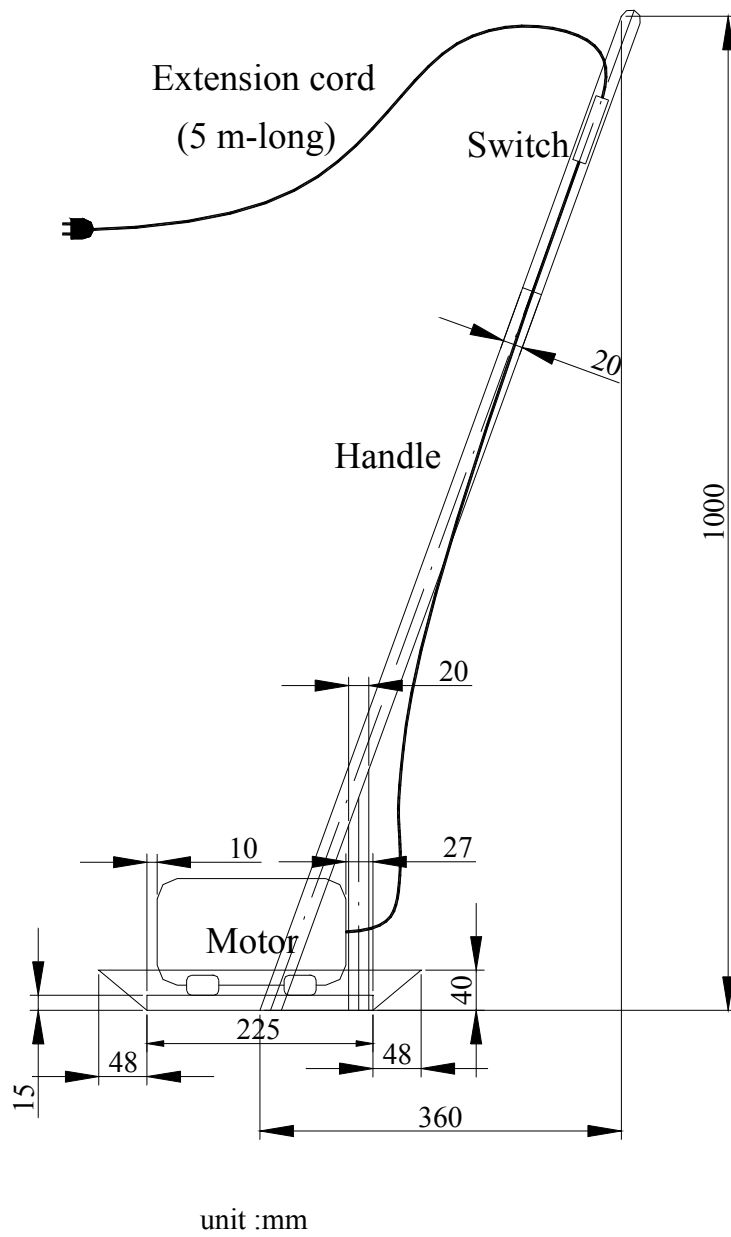


Fig. 3.5. Side-view of vibratory soil compactor (after Chen, 2003)



Fig. 3.6. Vibratory soil compactor (after Chen, 2003)

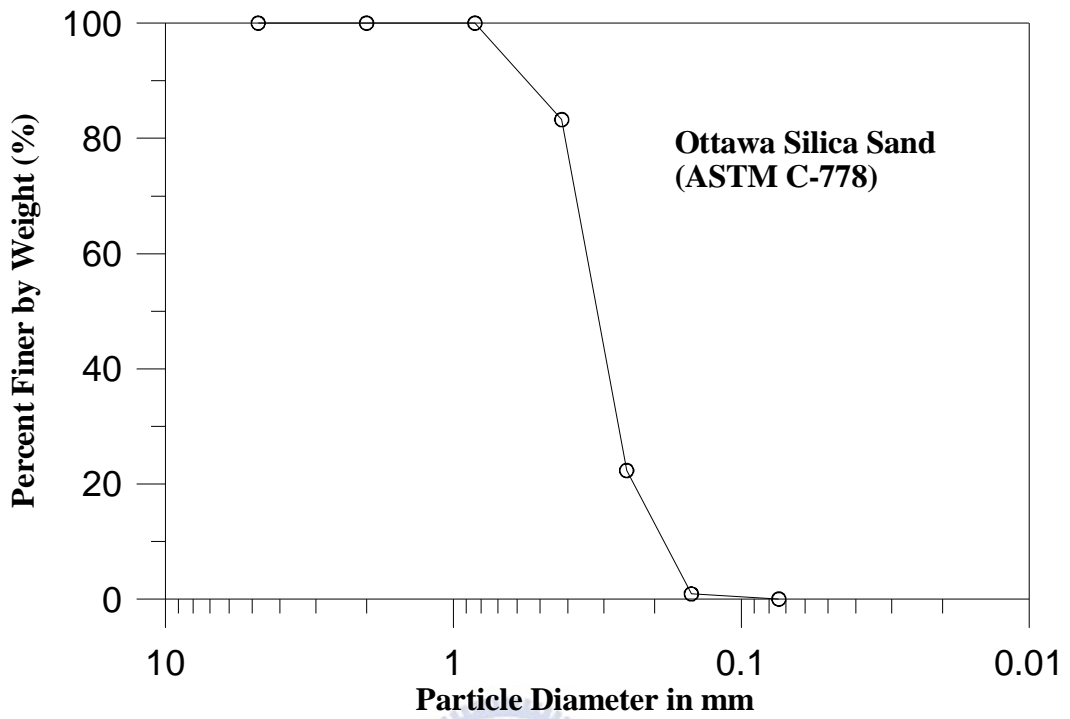
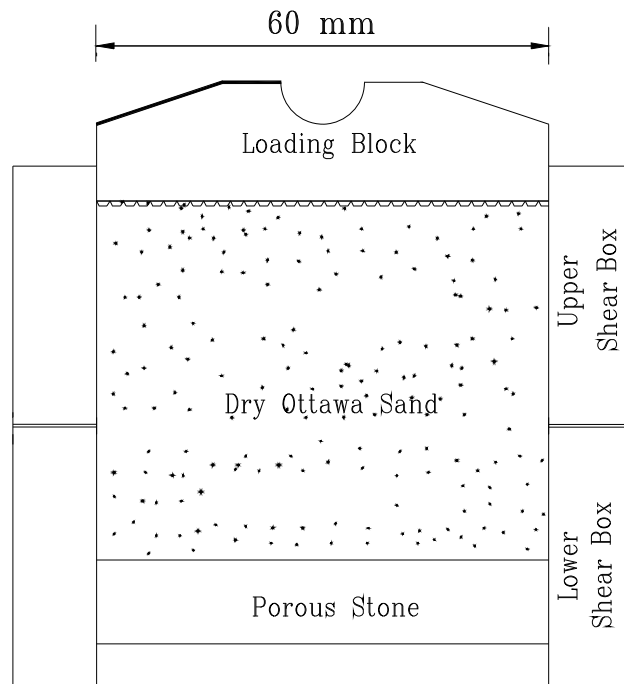


Fig. 4.1. Grain size distribution of Ottawa sand (after Hou, 2006)



Unit : mm



Fig. 4.2. Shear box of direct shear test device (after Wu, 1992)

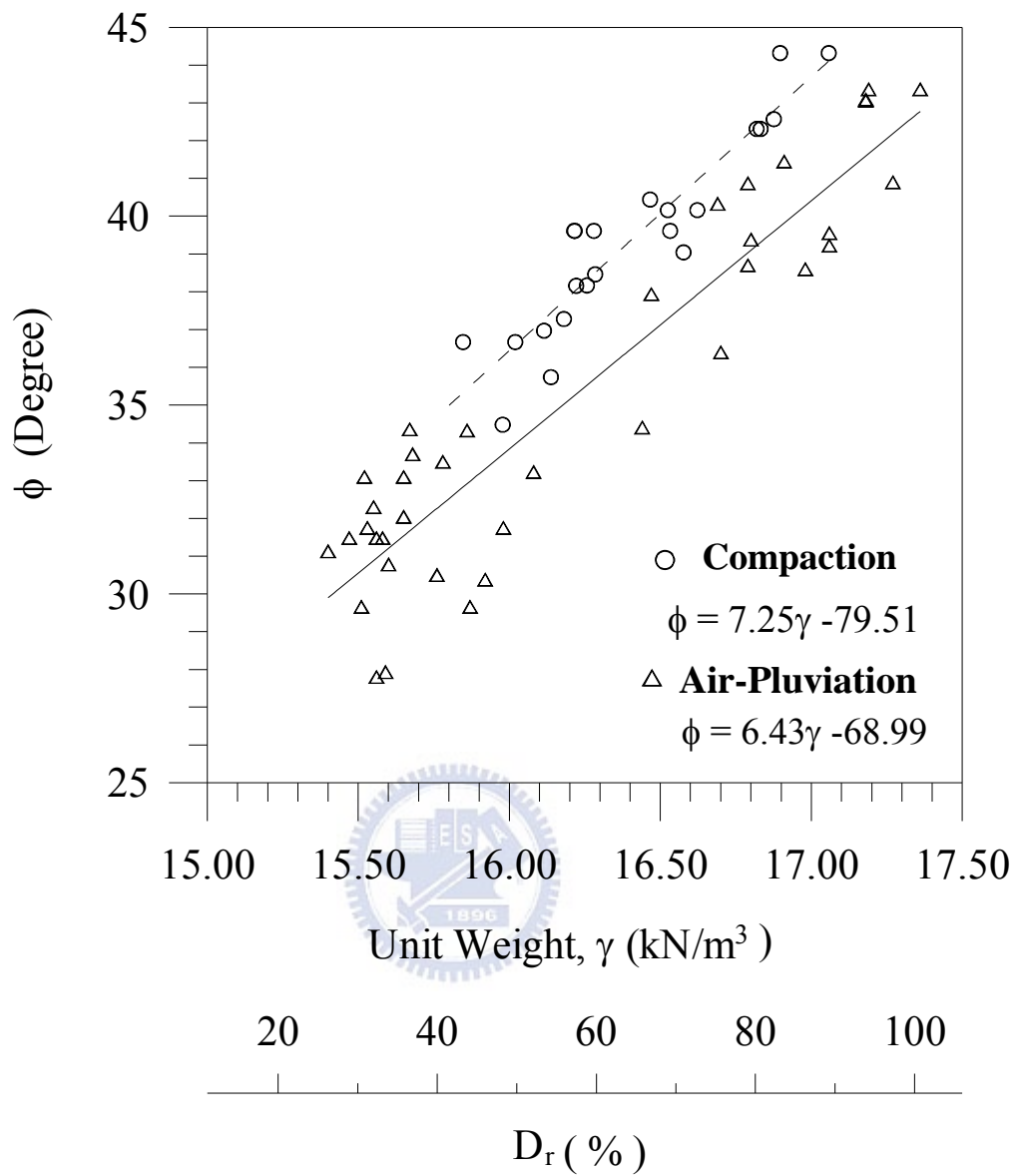


Fig. 4.3. Relationship between unit weight γ and internal friction angle (after Chang, 2000)

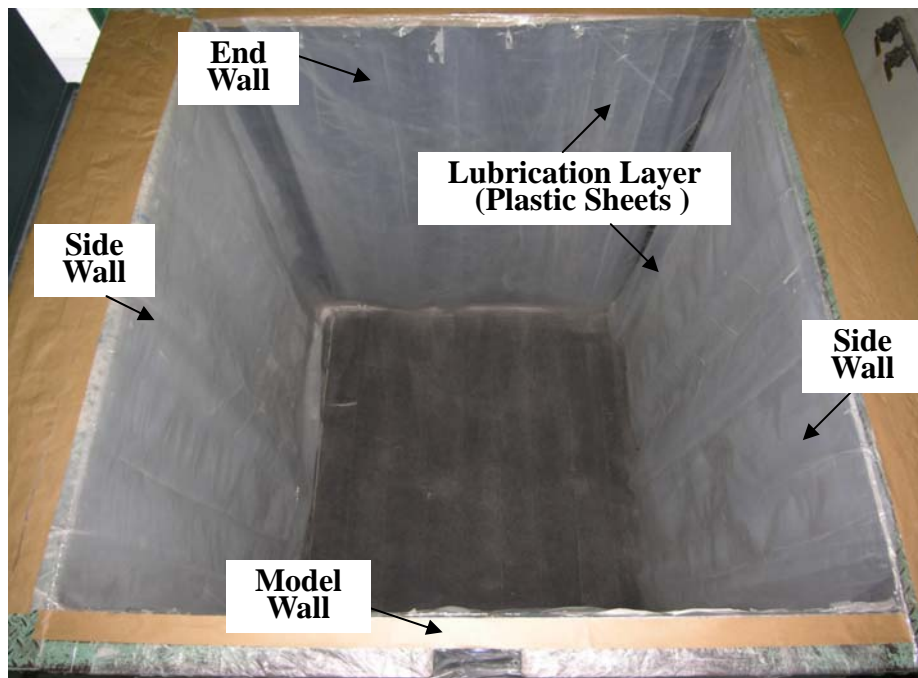
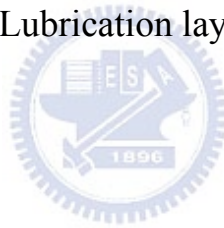


Fig. 4.4. Lubrication layers on four walls



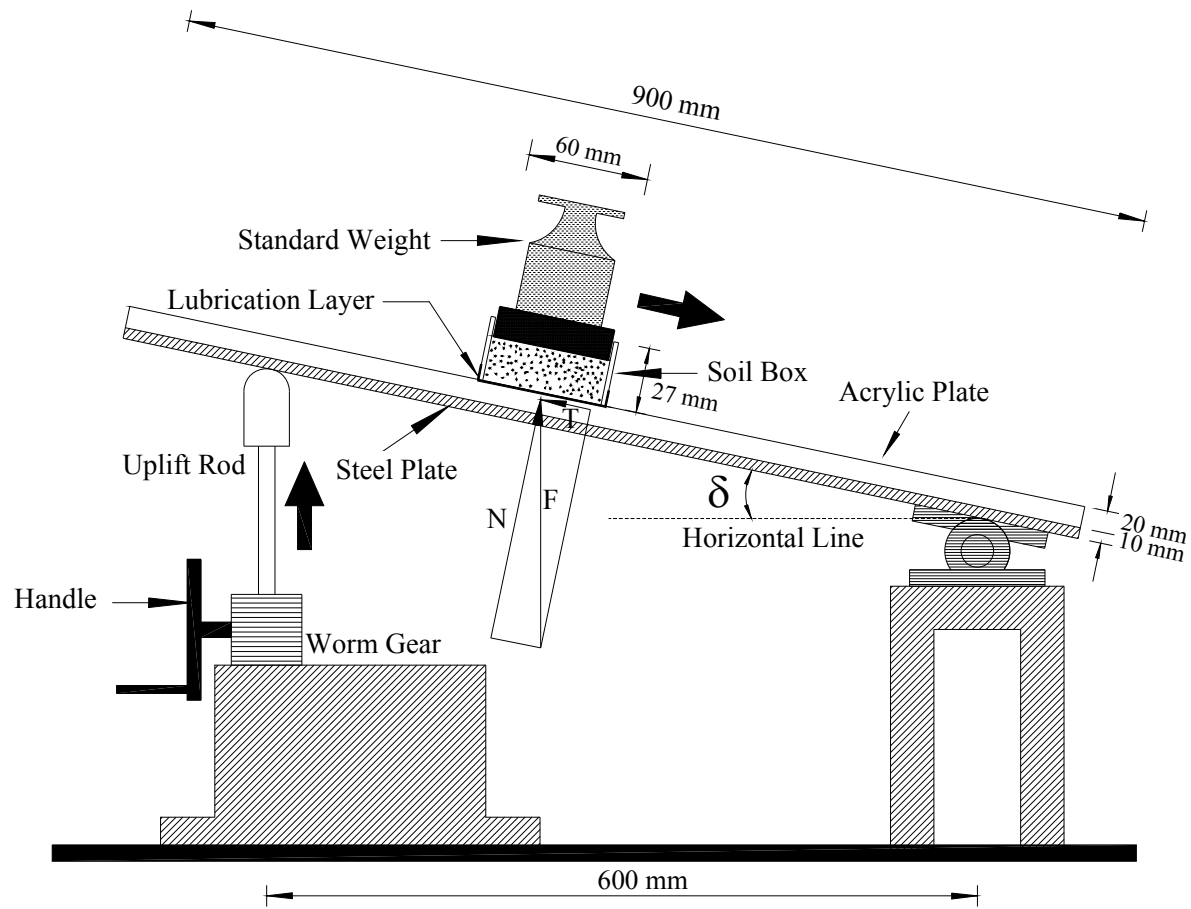


Fig. 4.5. Schematic diagram of sliding block test (after Fang et al., 2004)

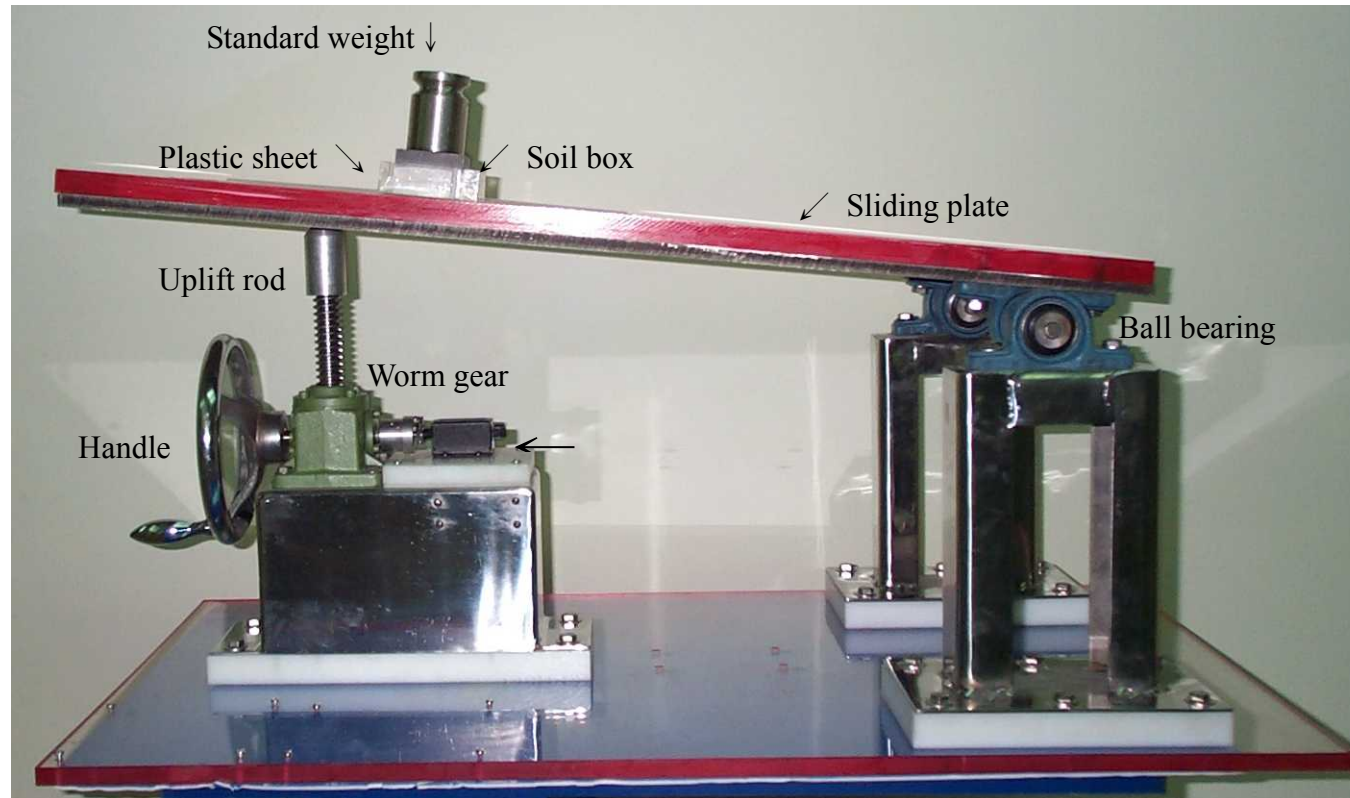


Fig. 4.6. Sliding block test apparatus (after Fang et al., 2004)

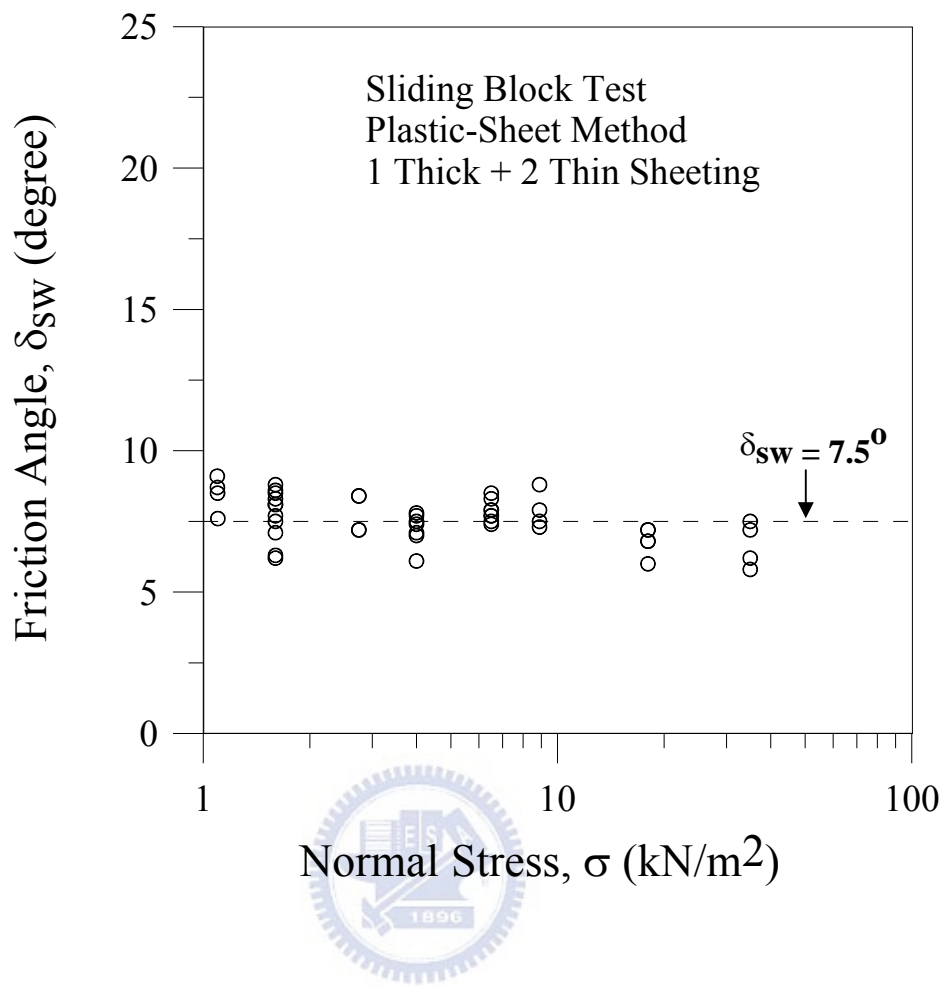
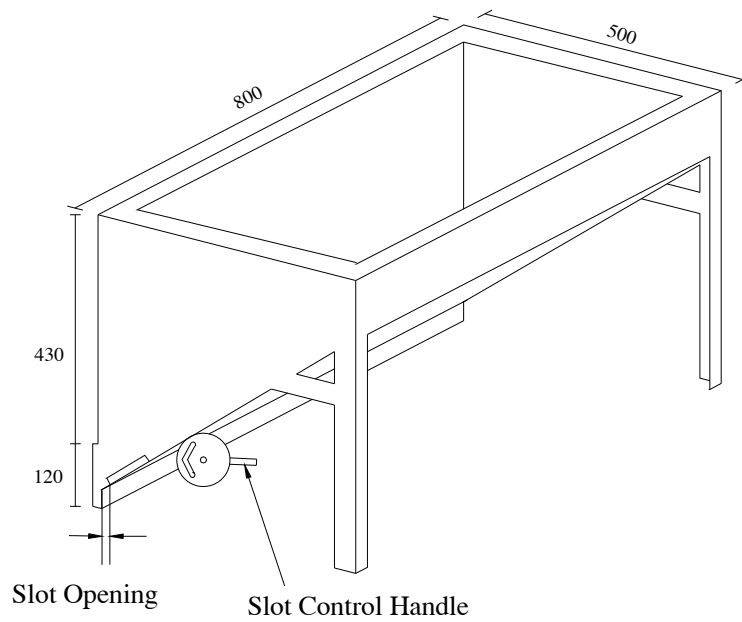


Fig. 4.7. Variation of interface angle with normal stress (after Fang et al., 2004)



(a)



Unit:mm

(b)

Fig. 5.1. Soil hopper



Fig. 5.2. Pluviation of the Ottawa sand into soil bin

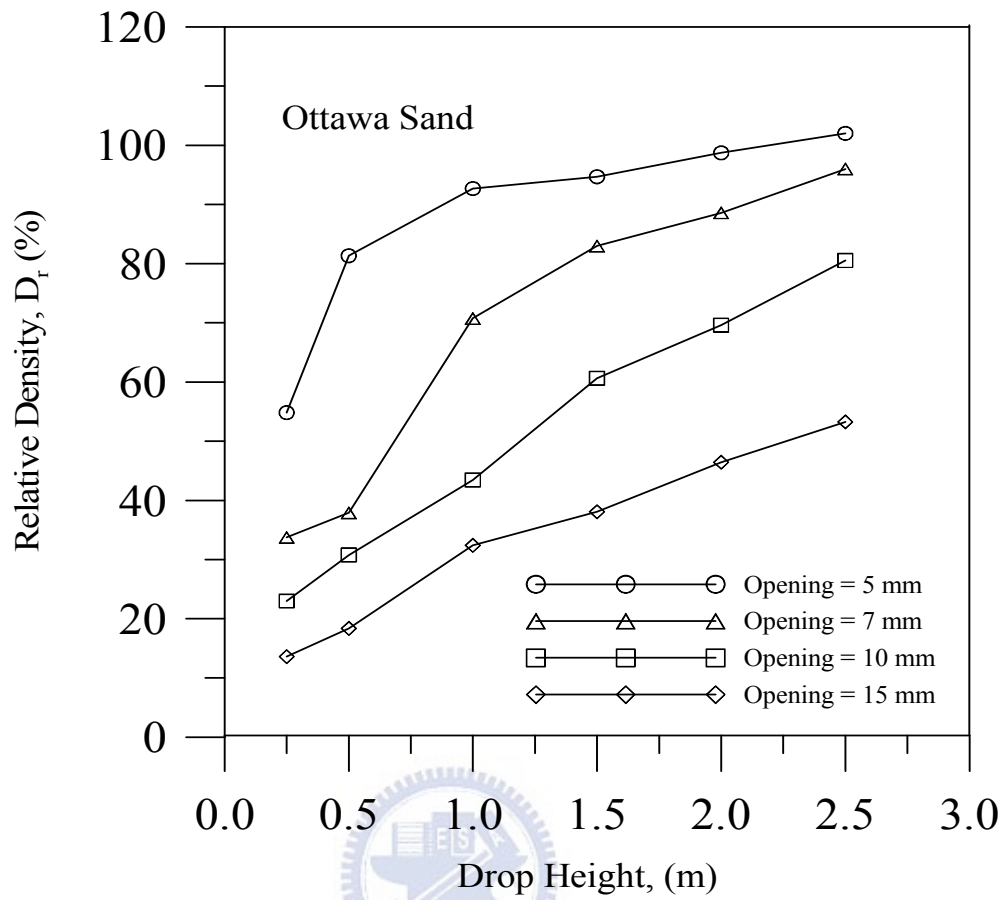
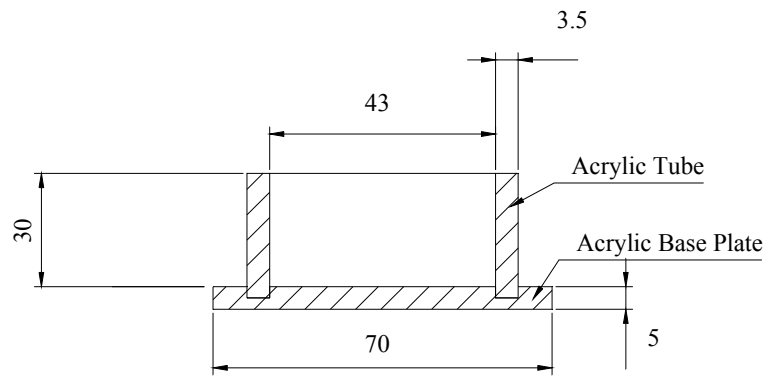
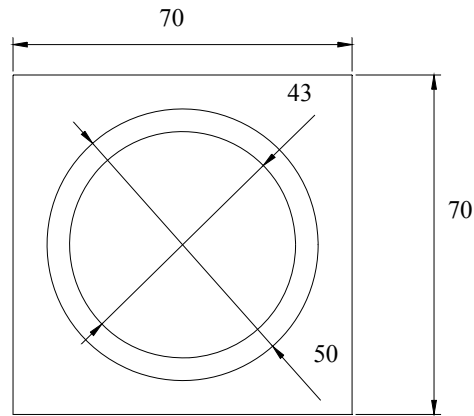


Fig. 5.3. Relationship between relation density and drop height
(after Ho, 1999)



Side-view



Top-view

unit : mm

Fig. 5.4. Soil-density cup (after Ho, 1999)

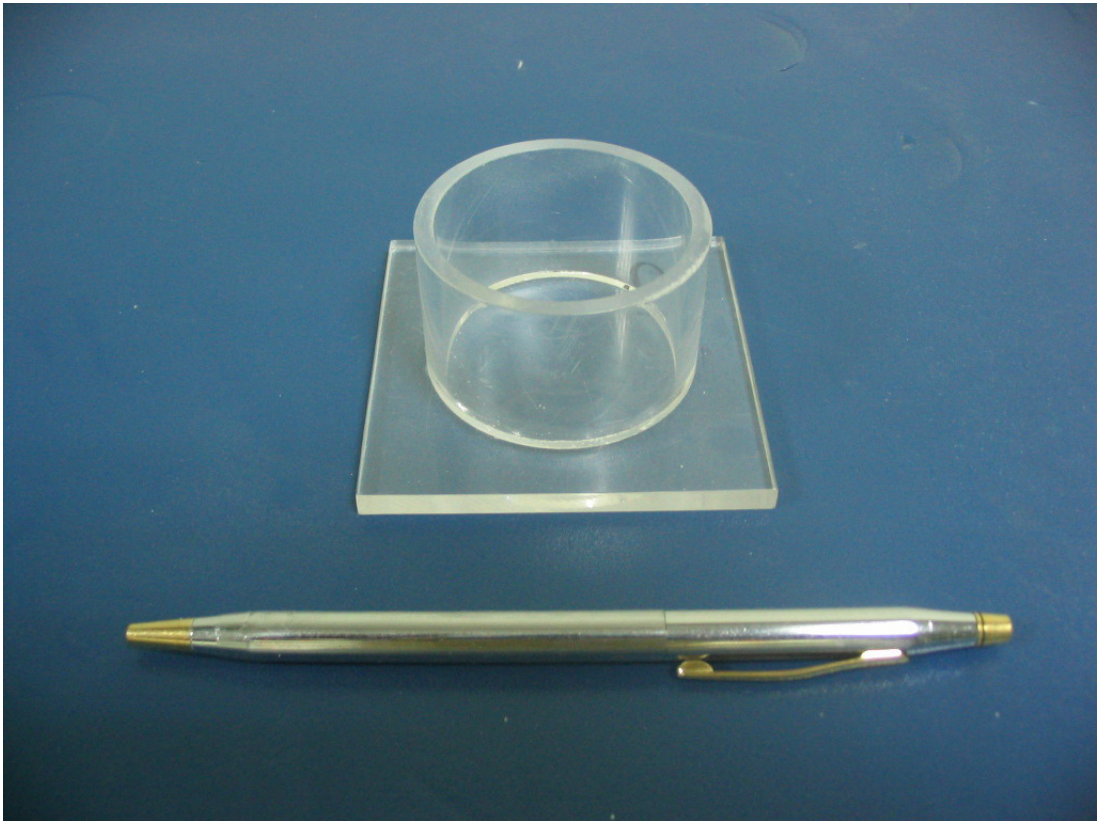


Fig. 5.5. Photo of soil-density cup

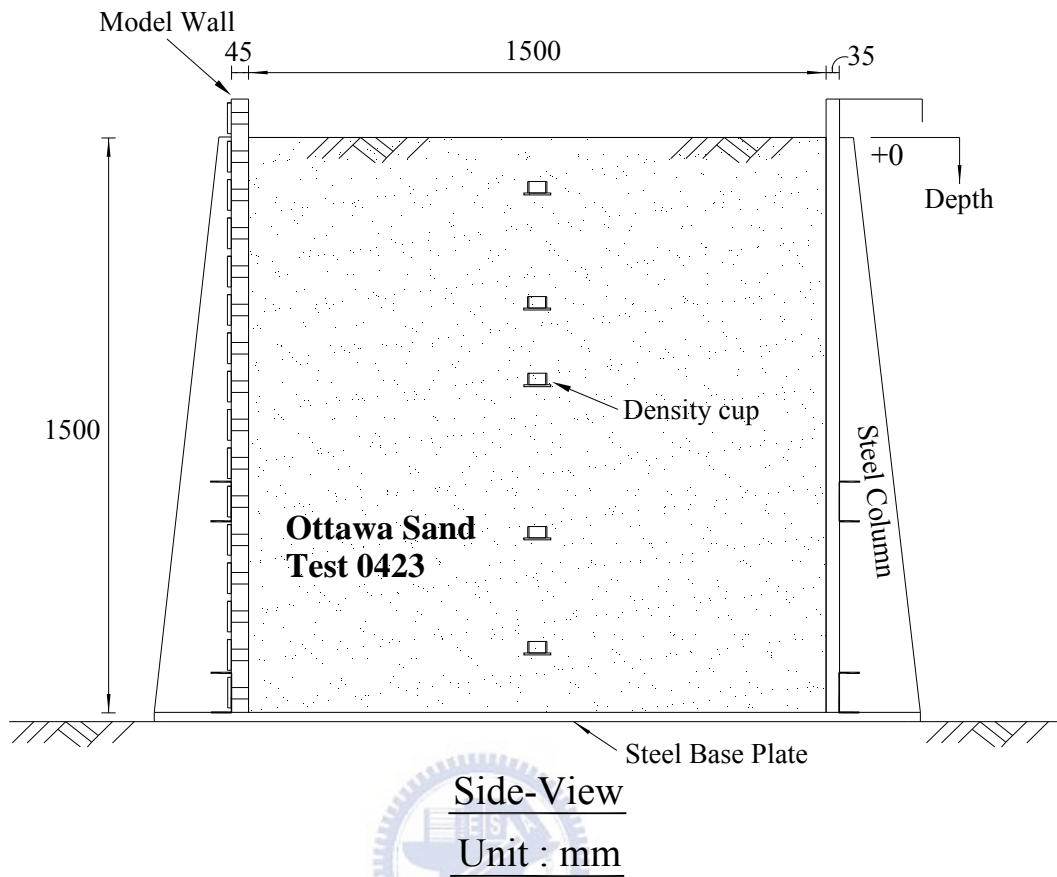
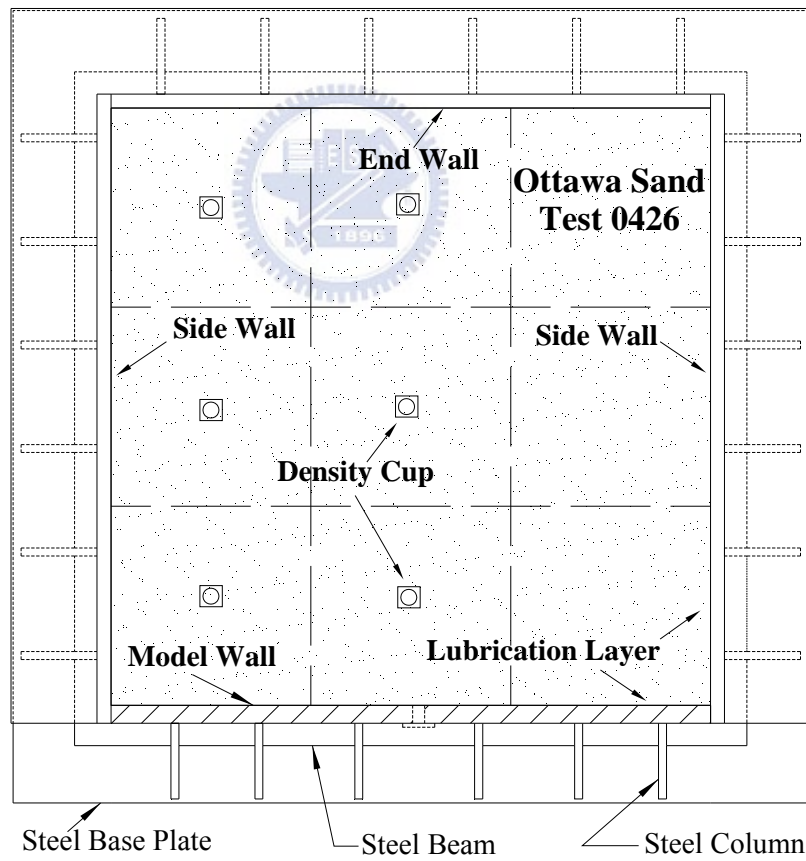


Fig. 5.6. Soil density cups buried at the different elevations



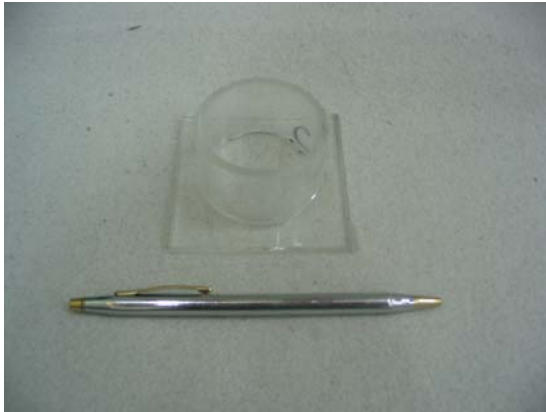
(a)



Top-View

(b)

Fig. 5.7. Locations of soil density cups at the same elevation



(a) Empty soil density cup



(b) Cup buried in sand



(c) Density cup dug out



(d) Measurement of cup and soil mass

Fig. 5.8. Procedures of soil density control test

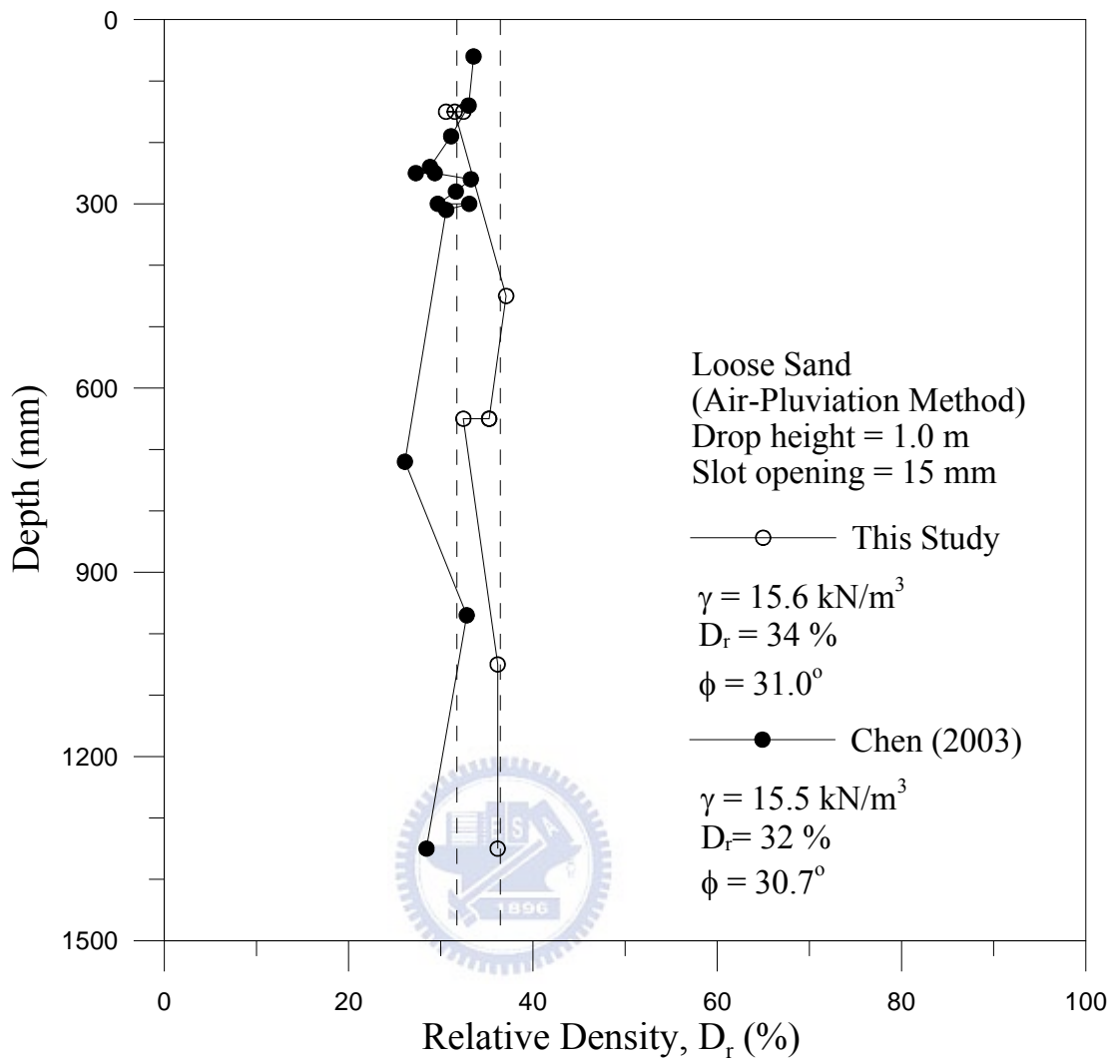
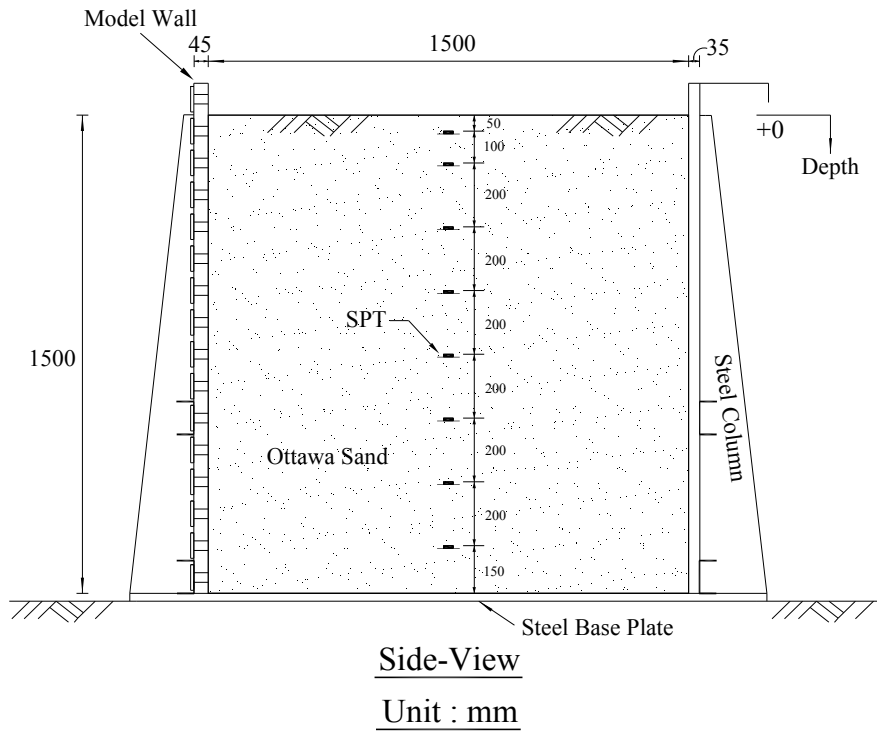
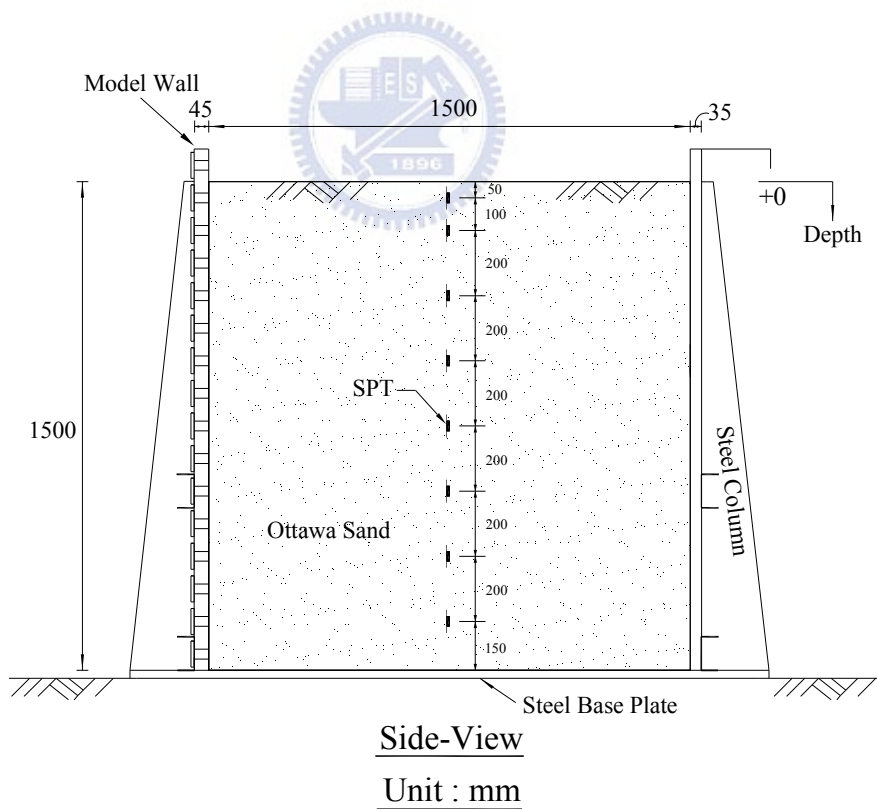


Fig. 5.9. Distribution of soil density for loose sand



(a)



(b)

Fig. 5.10. (a) Locations of SPT to measure vertical earth pressure;
(b) Locations of SPT to measure horizontal earth pressure

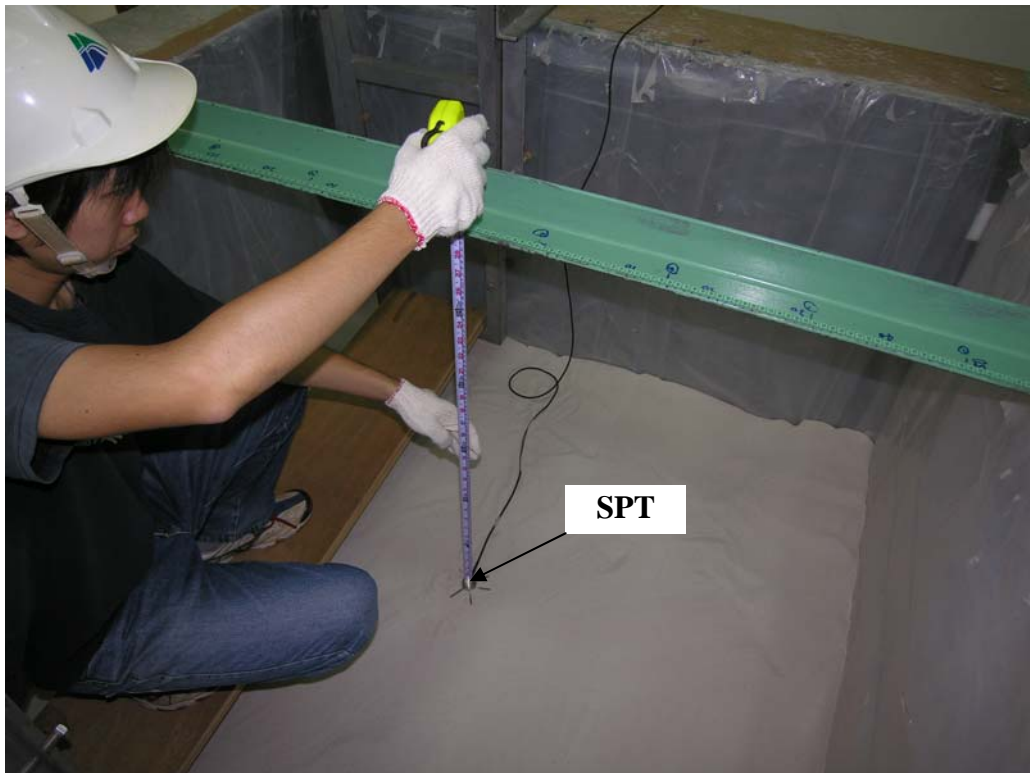
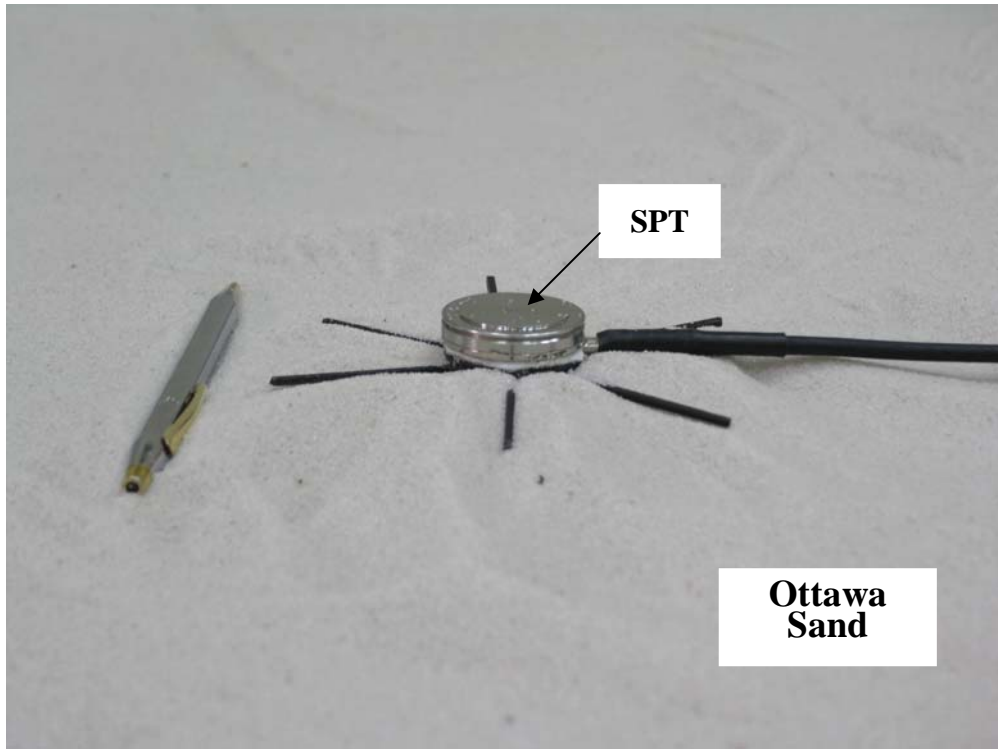
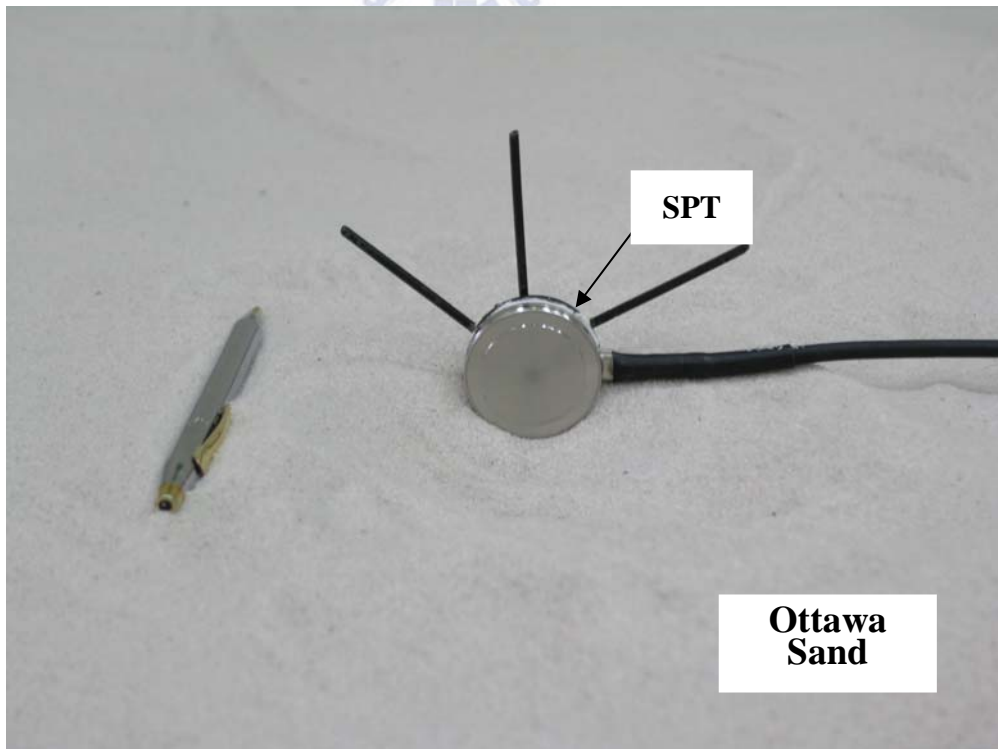


Fig. 5.11. Positioning of soil pressure transducer in the backfill



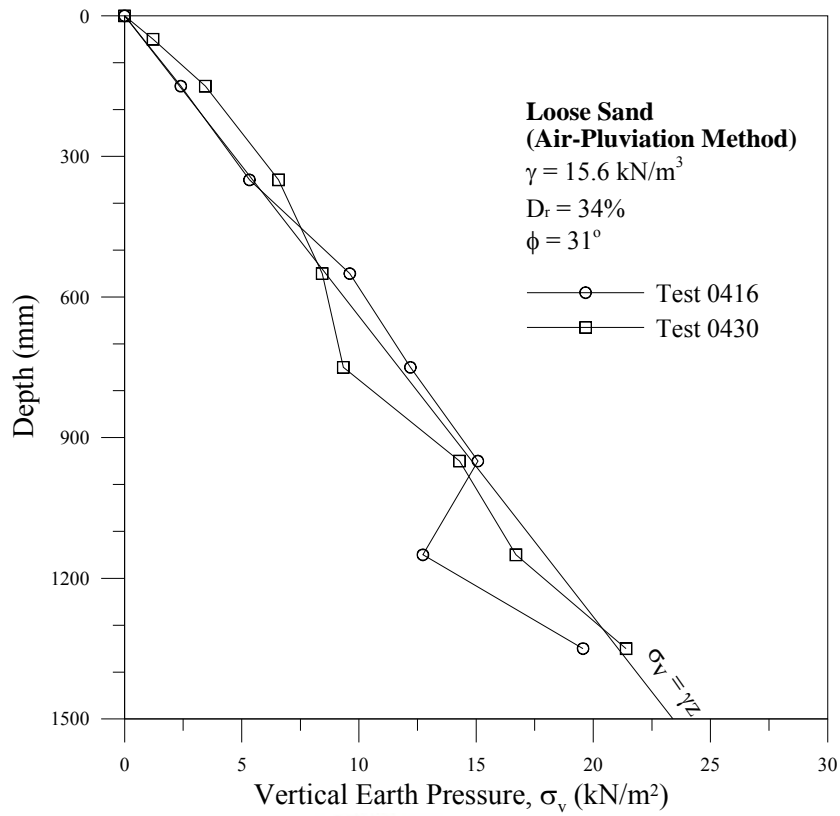


(a)

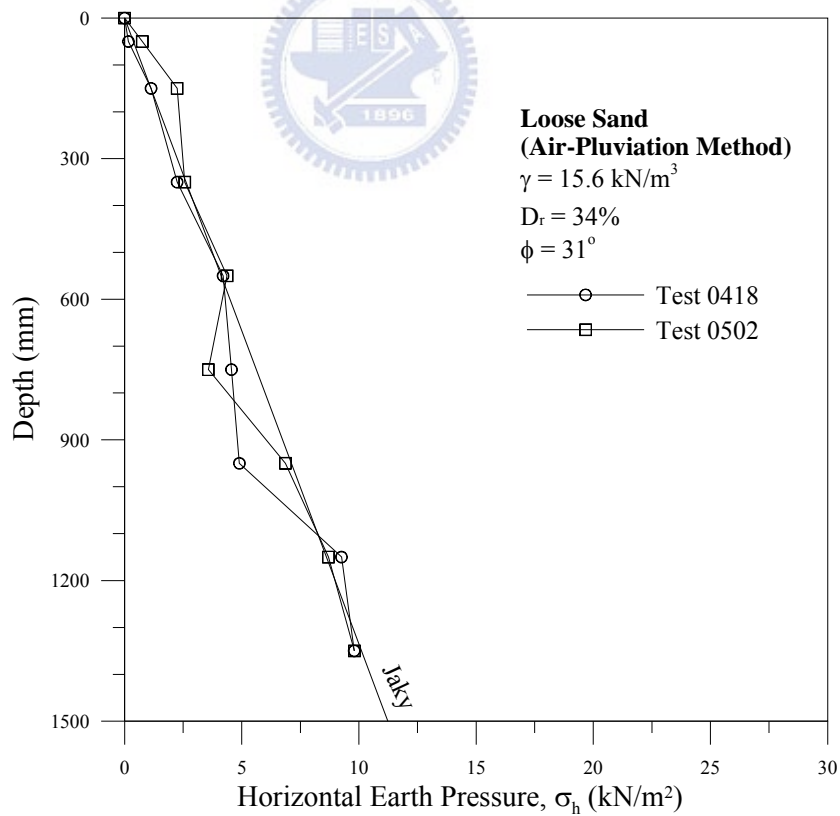


(b)

Fig. 5.12. (a) SPT placed in soil bin to measure σ_v
(b) SPT placed in soil bin to measure σ_h



(a)



(b)

Fig. 5.13. (a) Distributions of vertical earth pressure;
 (b) Distributions of horizontal earth pressure

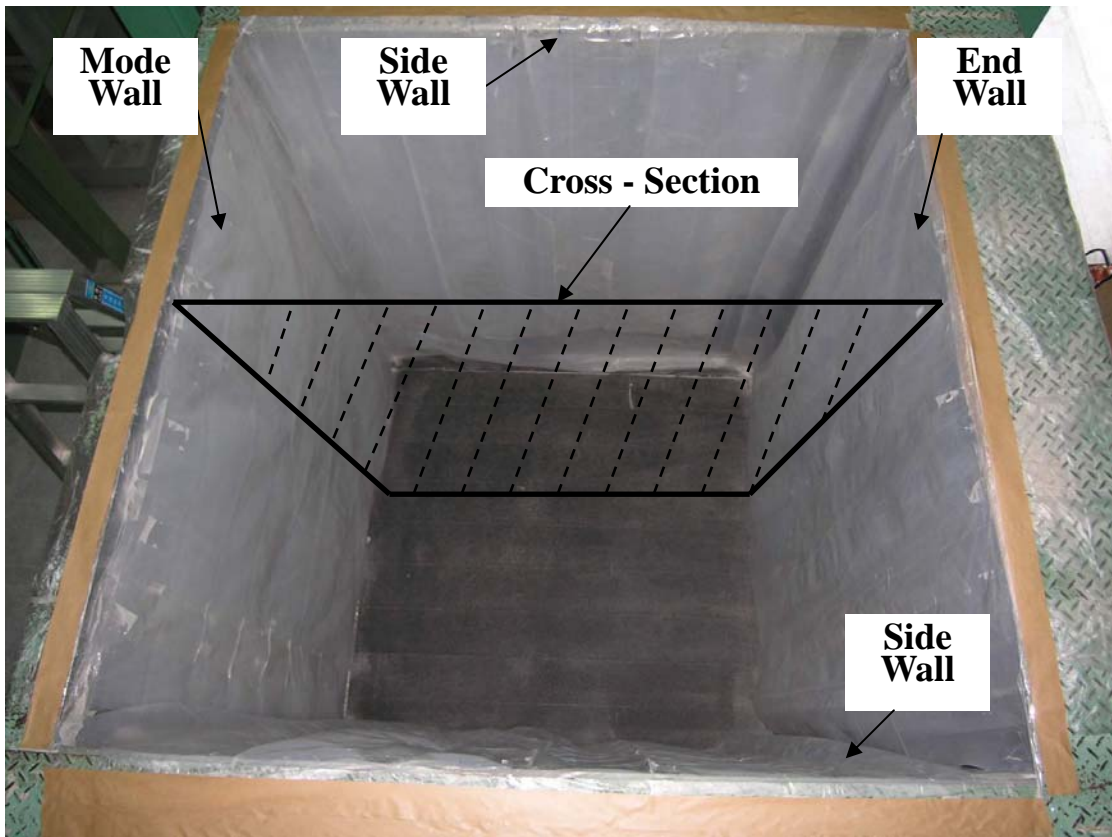


Fig. 6.1. Major cross-section of measurement in this study

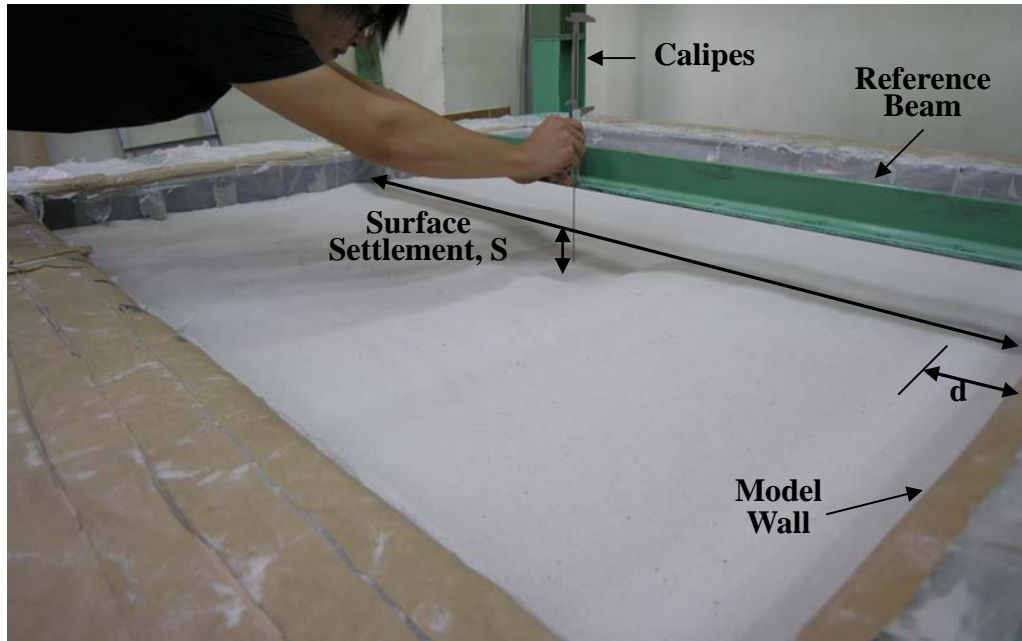


Fig. 6.2. Measurement of surface settlement



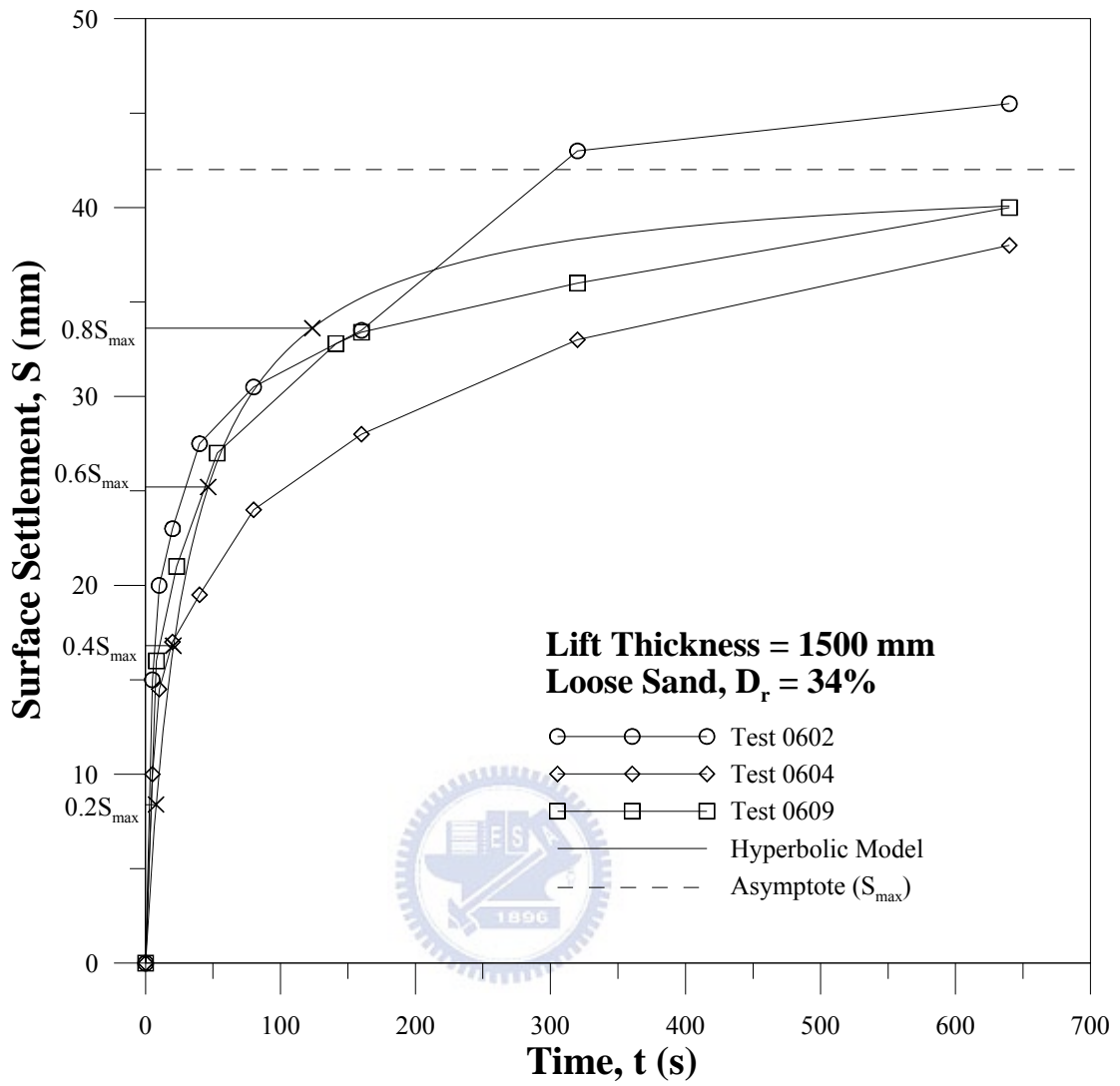


Fig. 6.3. Hyperbolic model to estimate surface settlement S as a function of compaction time

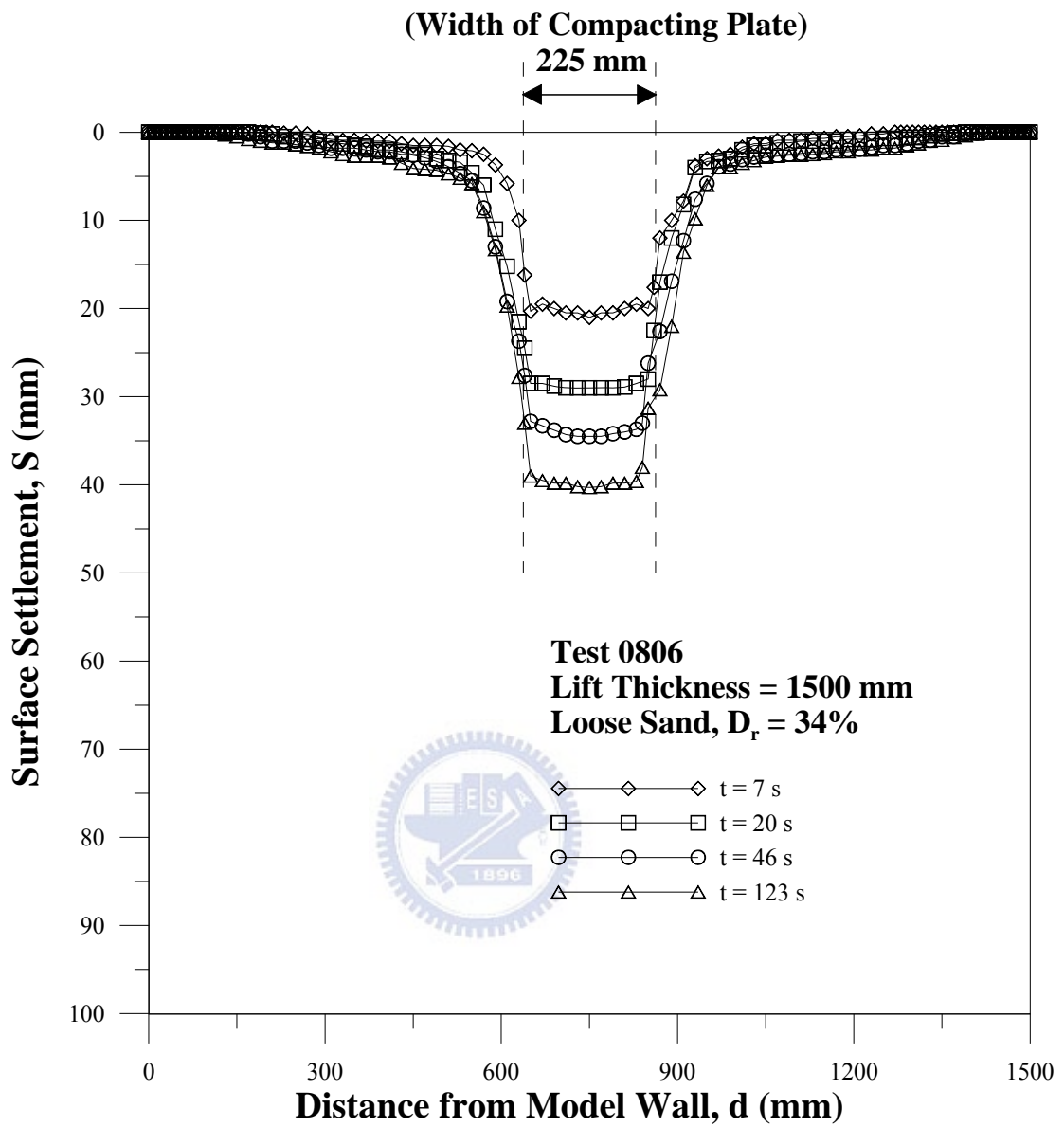


Fig. 6.4. Variation of surface settlement due to compaction

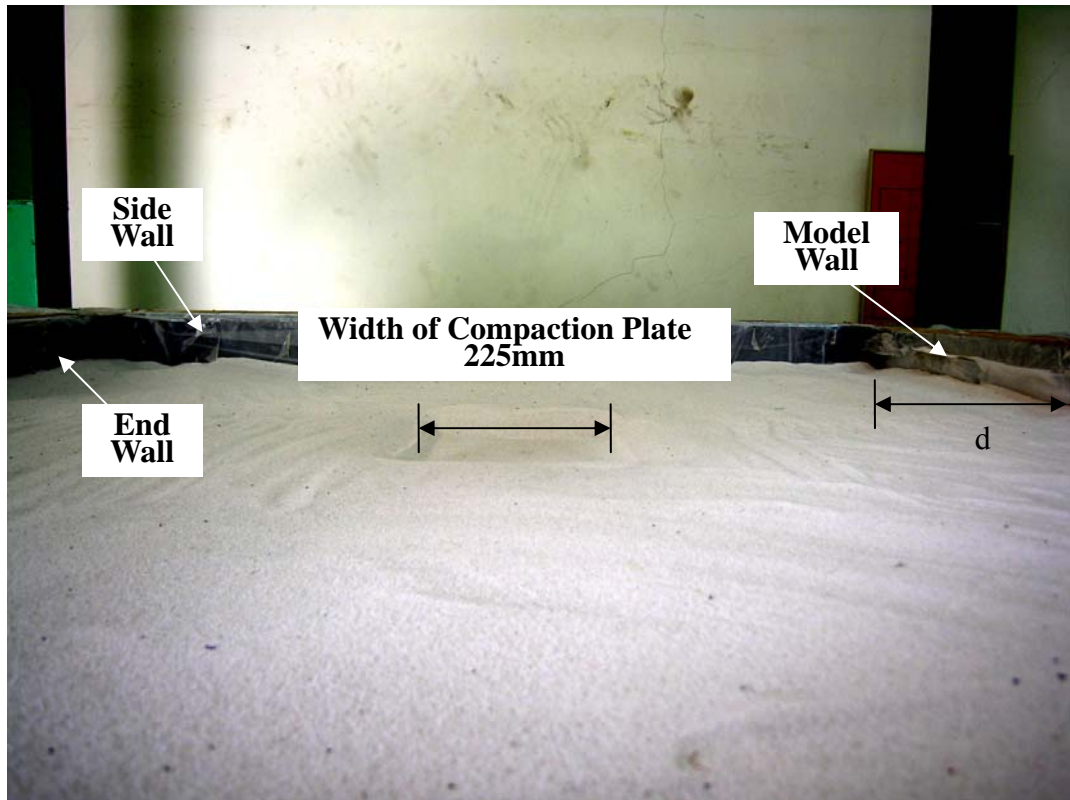
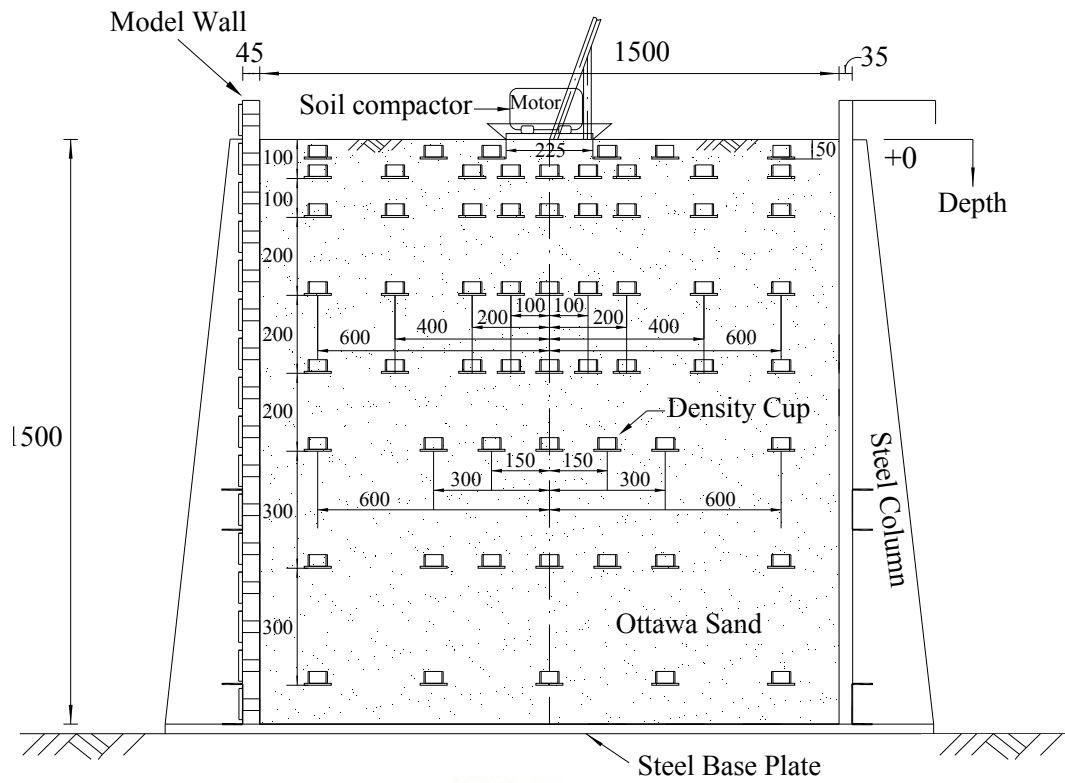


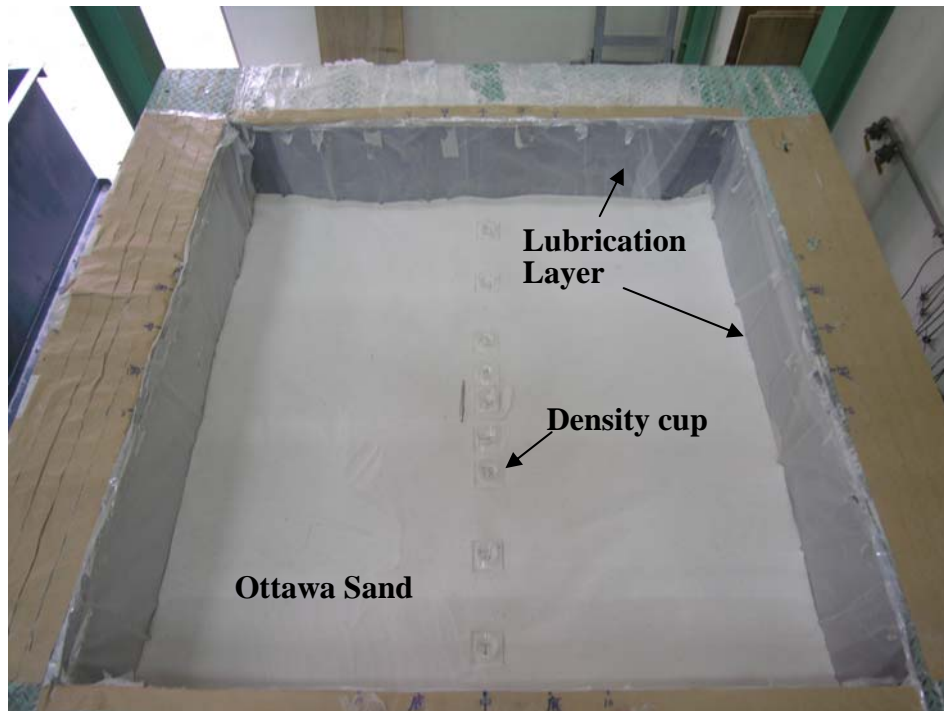
Fig. 6.5. Surface settlement after due to 123 s of compaction



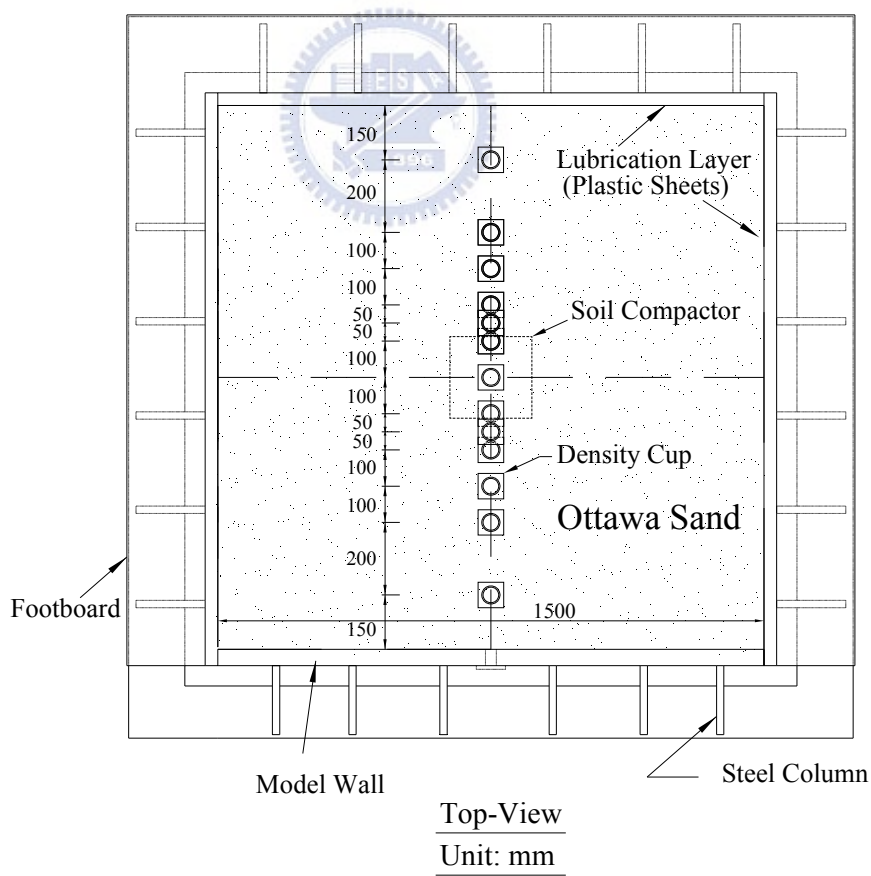
Side-View

Unit : mm

Fig. 6.6. Location of soil density cups in the backfill (side-view)



(a)



(b)

Fig. 6.7. Location of soil density cups (top-view)

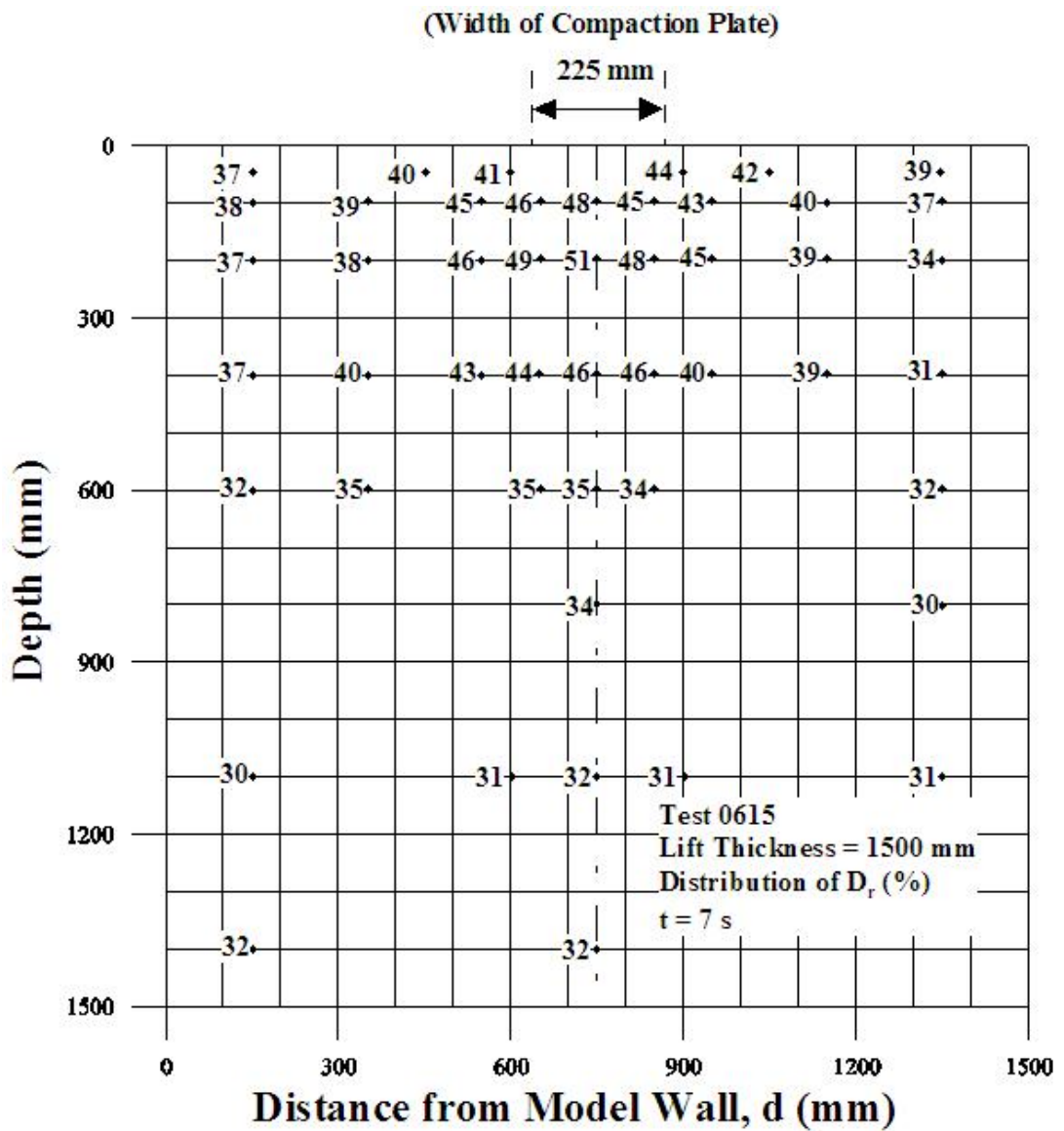


Fig. 6.8. Relative density measured at grid points after 7 s of point compaction

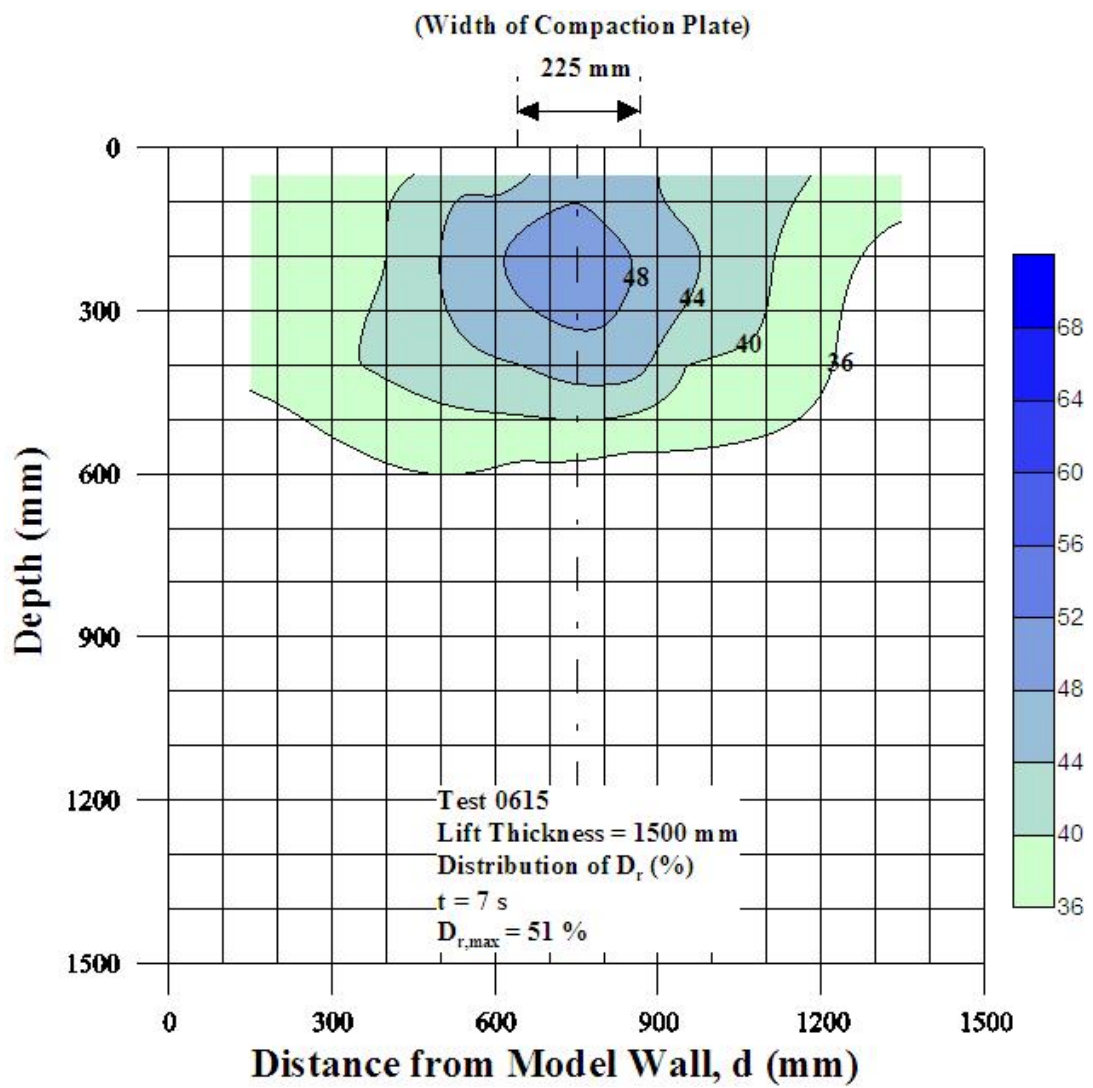


Fig. 6.9. Distribution of relative density after 7 s of point compaction

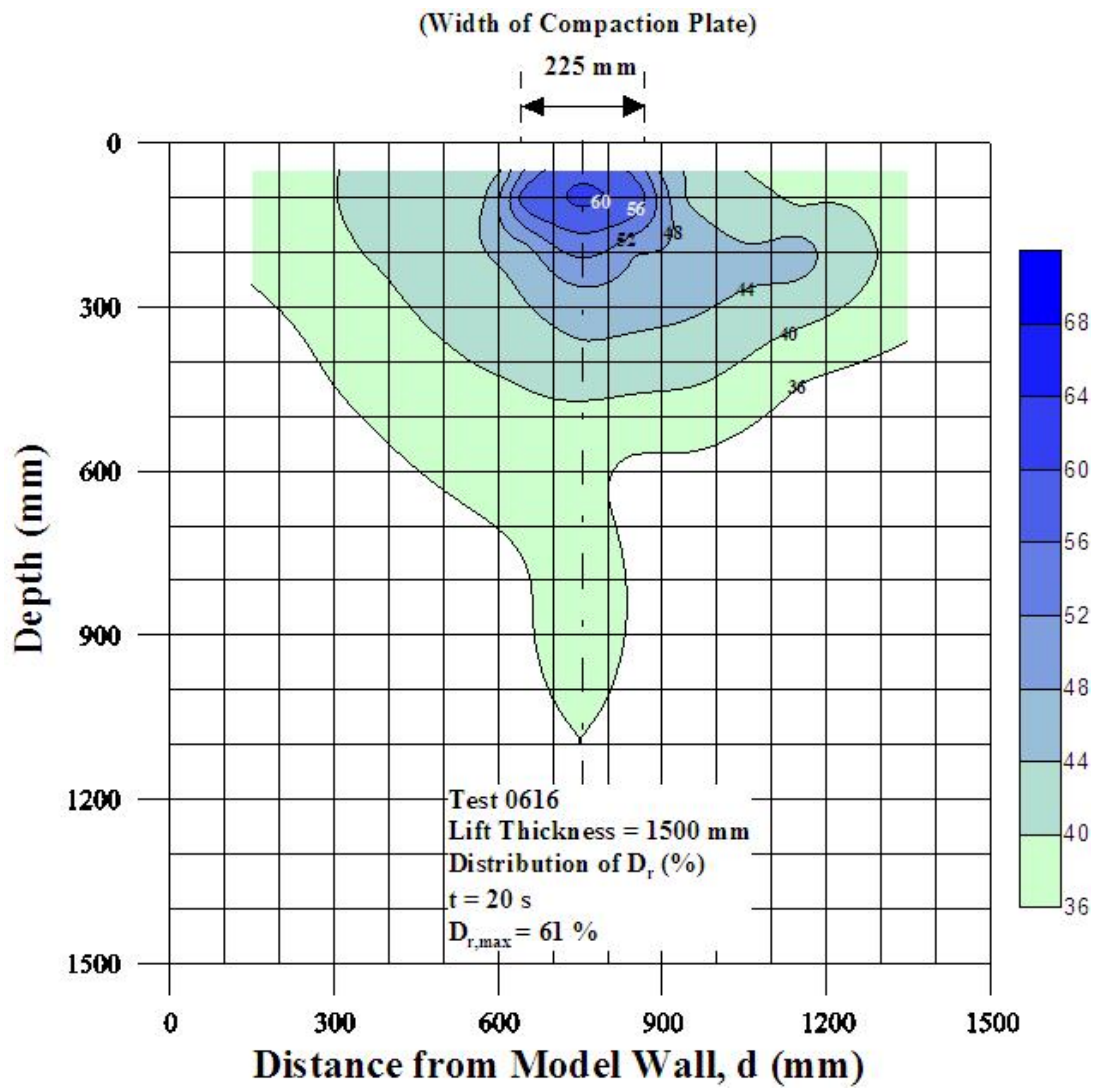


Fig. 6.10. Distribution of relative density after 20 s of point compaction

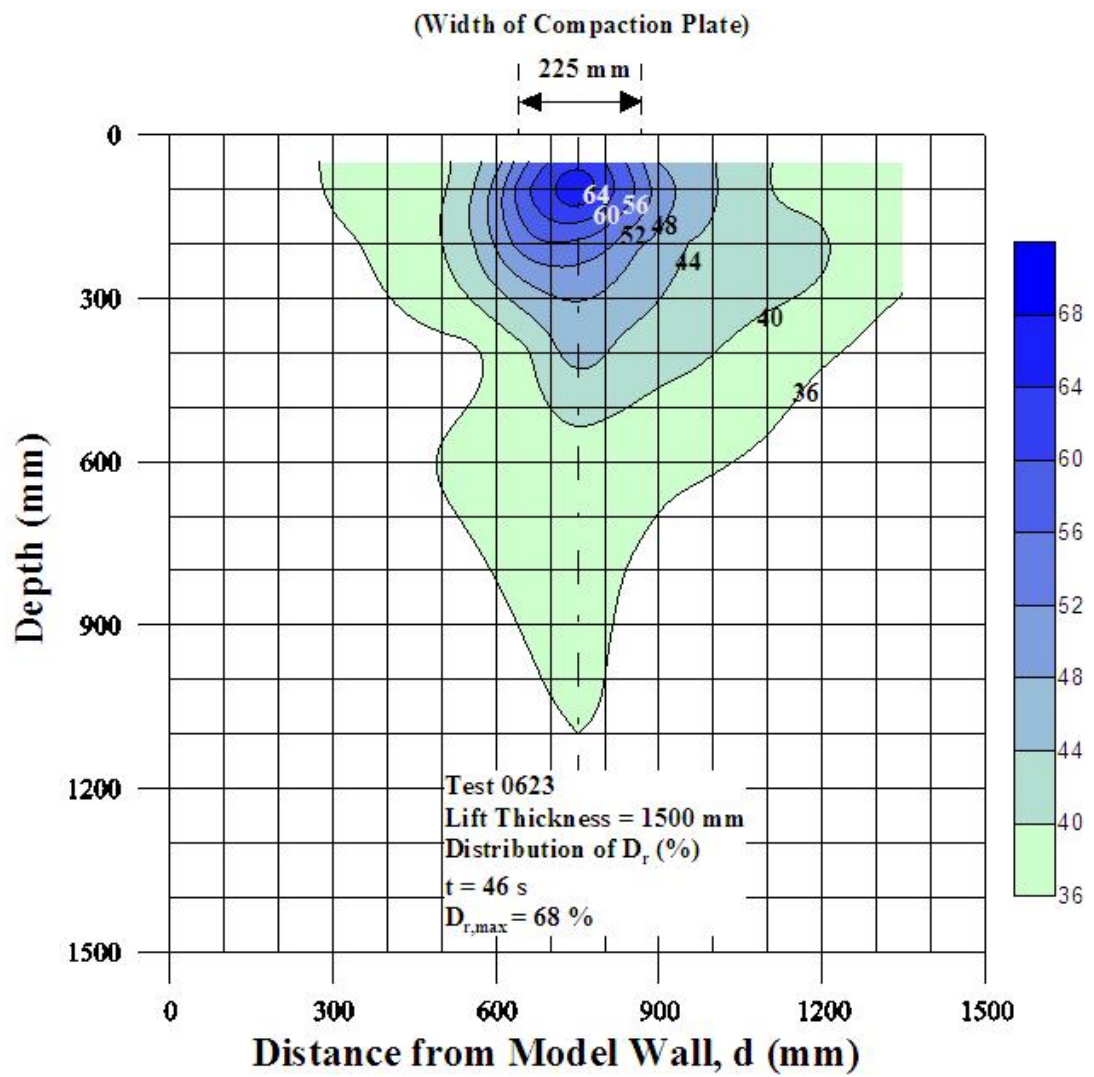


Fig. 6.11. Distribution of relative density after 46 s of point compaction

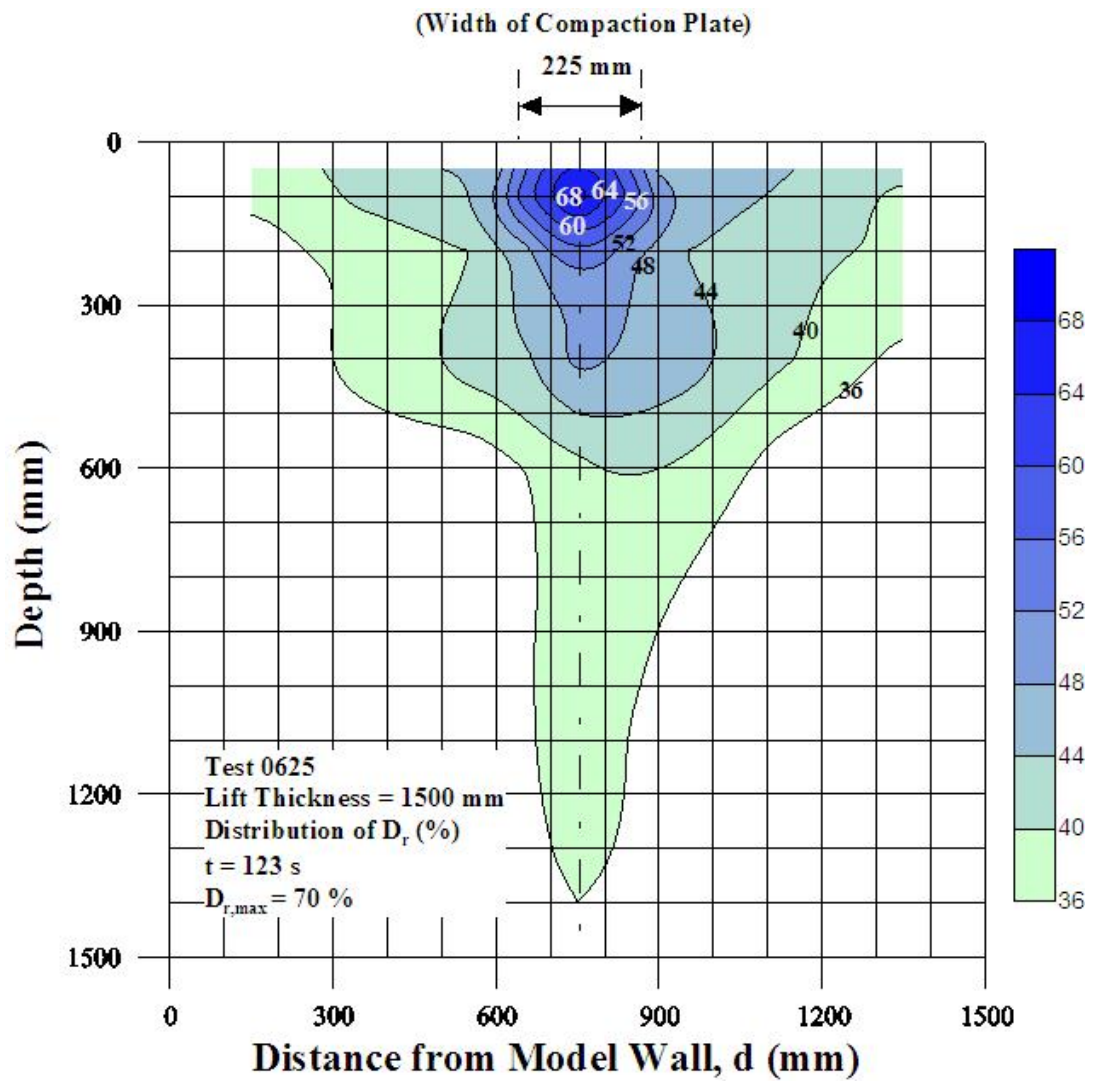


Fig. 6.12. Distribution of relative density after 123 s of point compaction

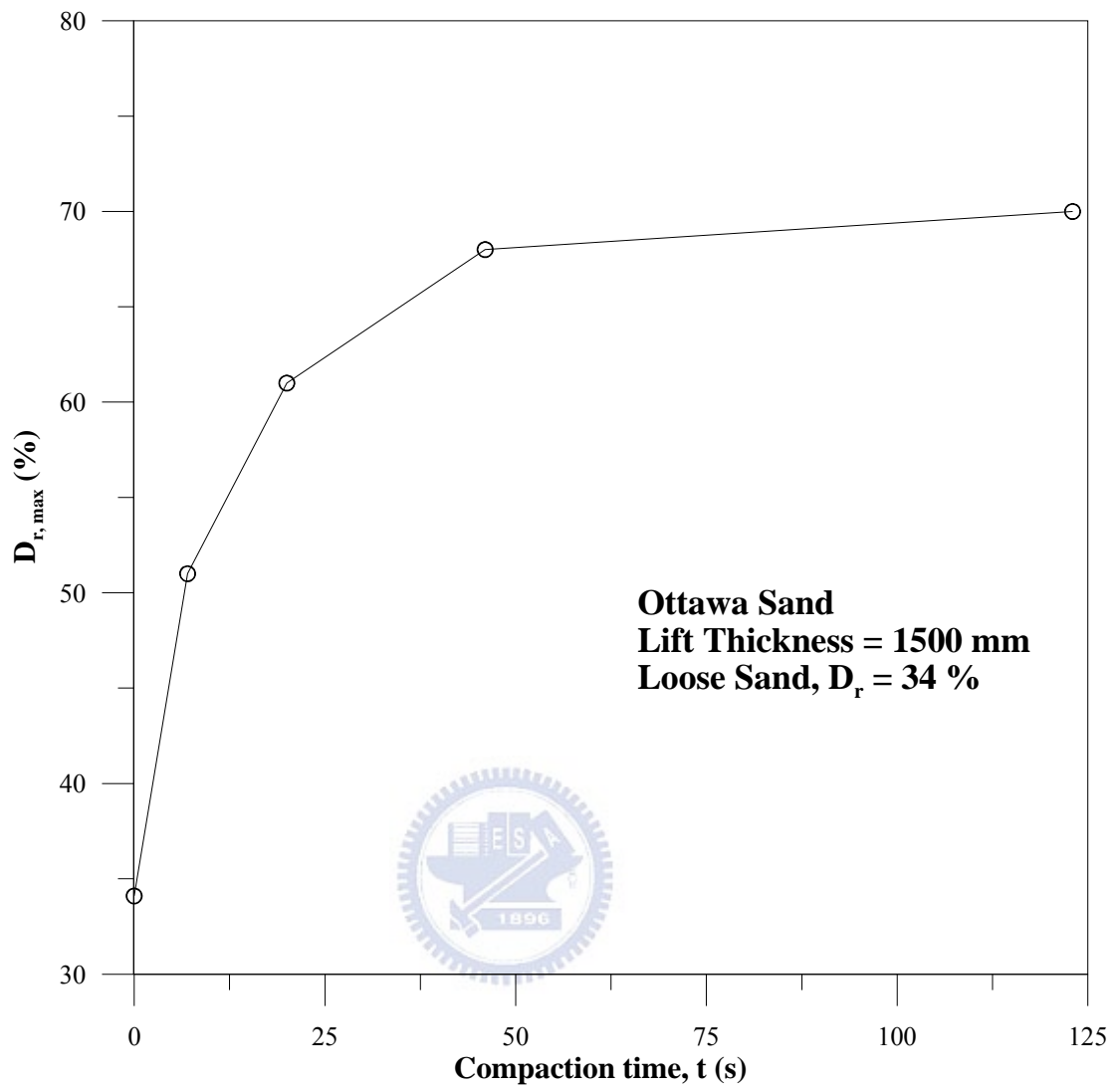


Fig. 6.13. Relationship between relative density and compaction time

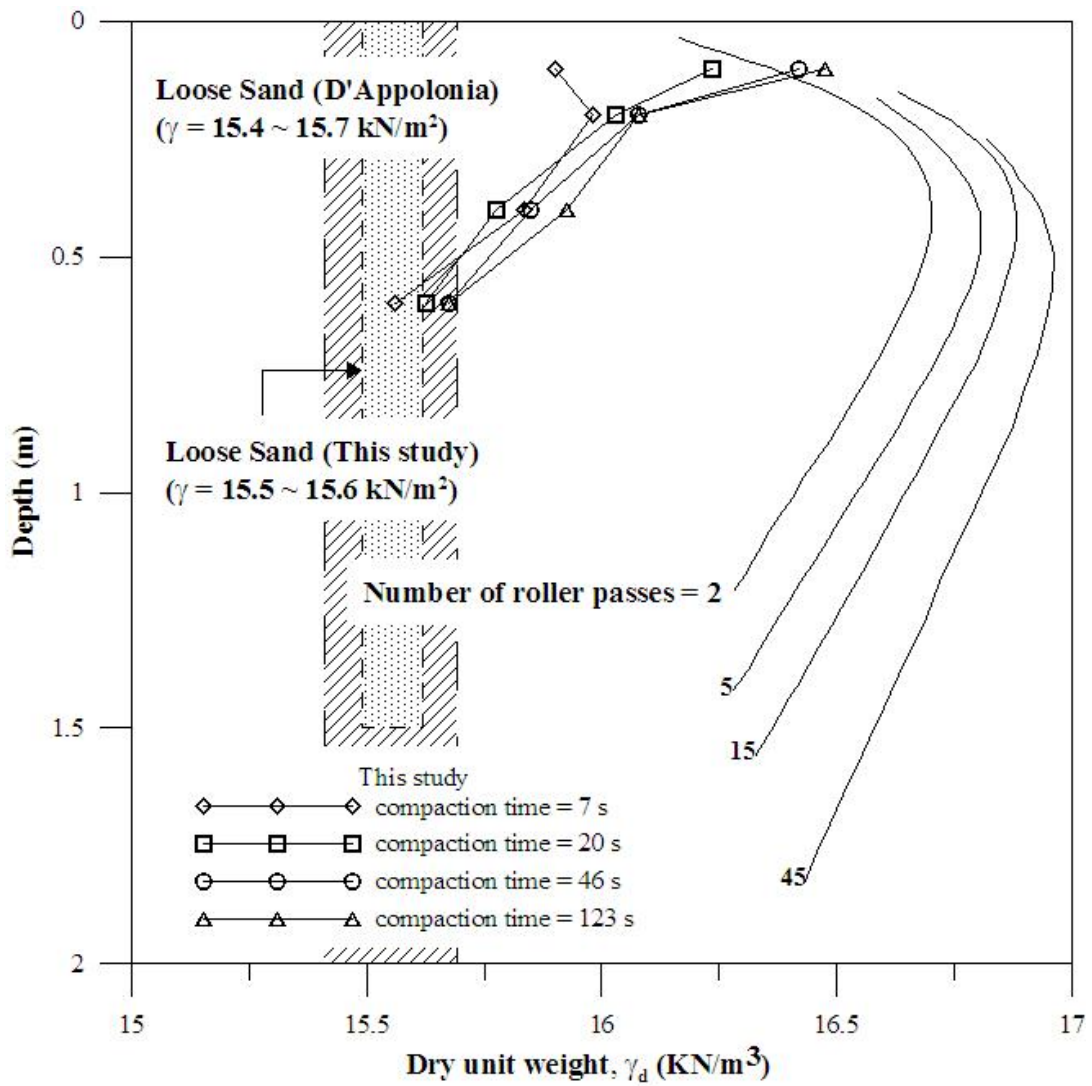


Fig. 6.14. Comparison of distribution of soil unit weight after compaction

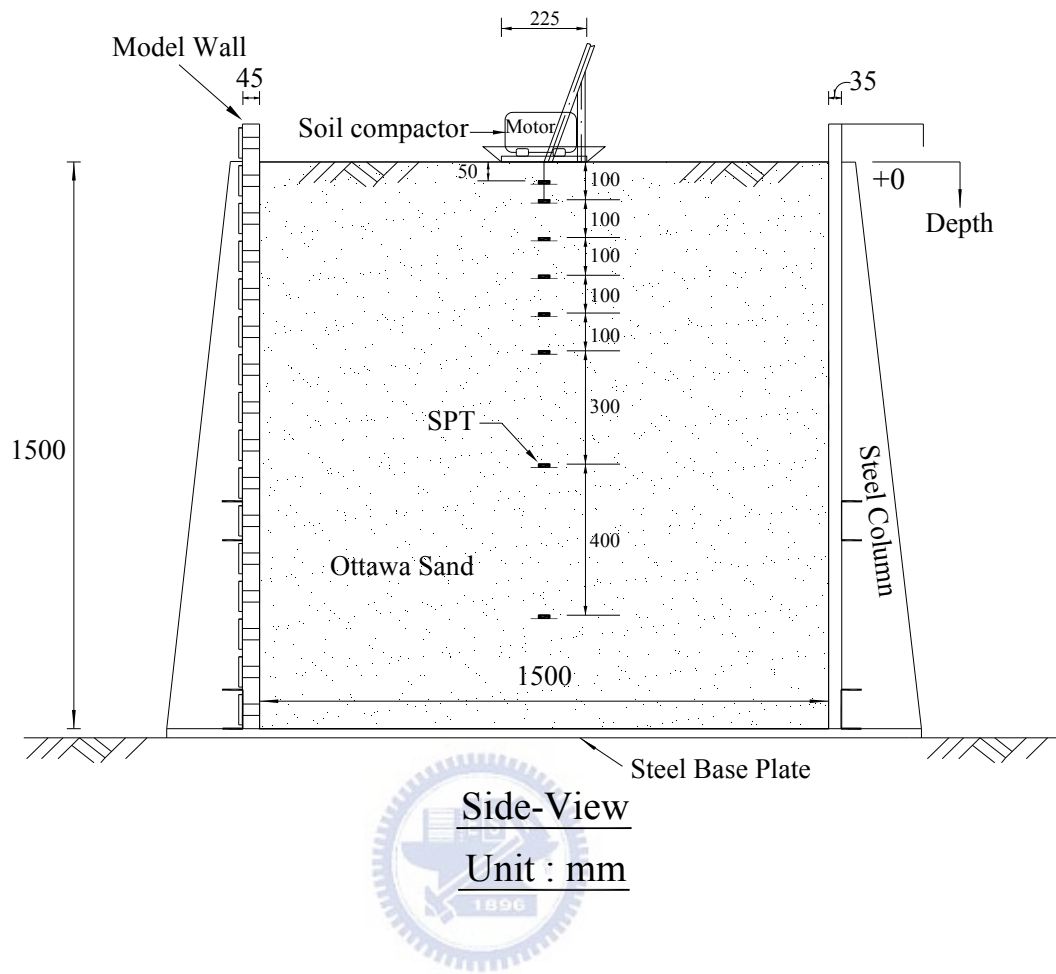


Fig. 7.1. Location of SPT to measure σ_v under the center of compactor (side view)

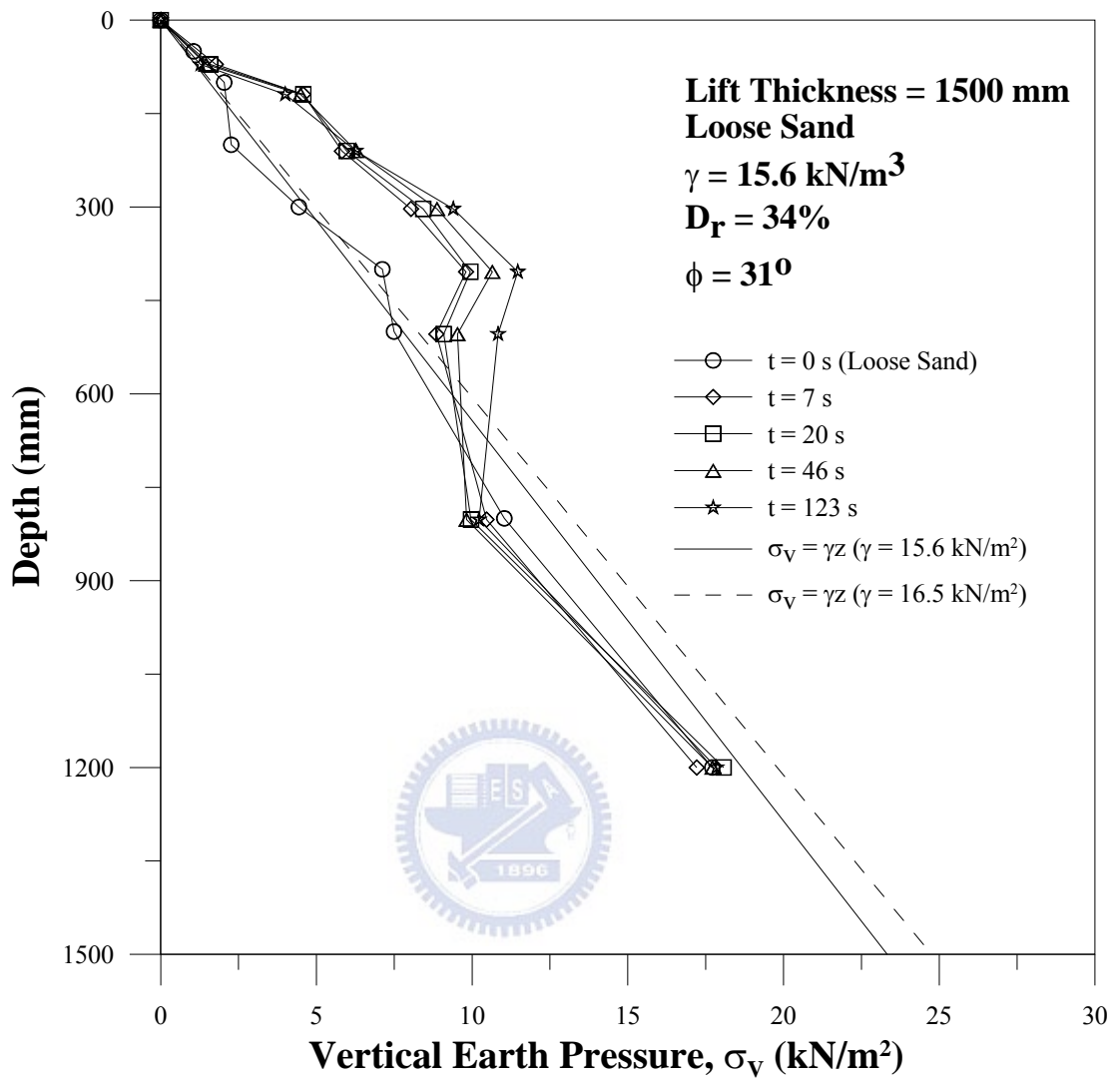


Fig. 7.2. Distributions of σ_v under compactor

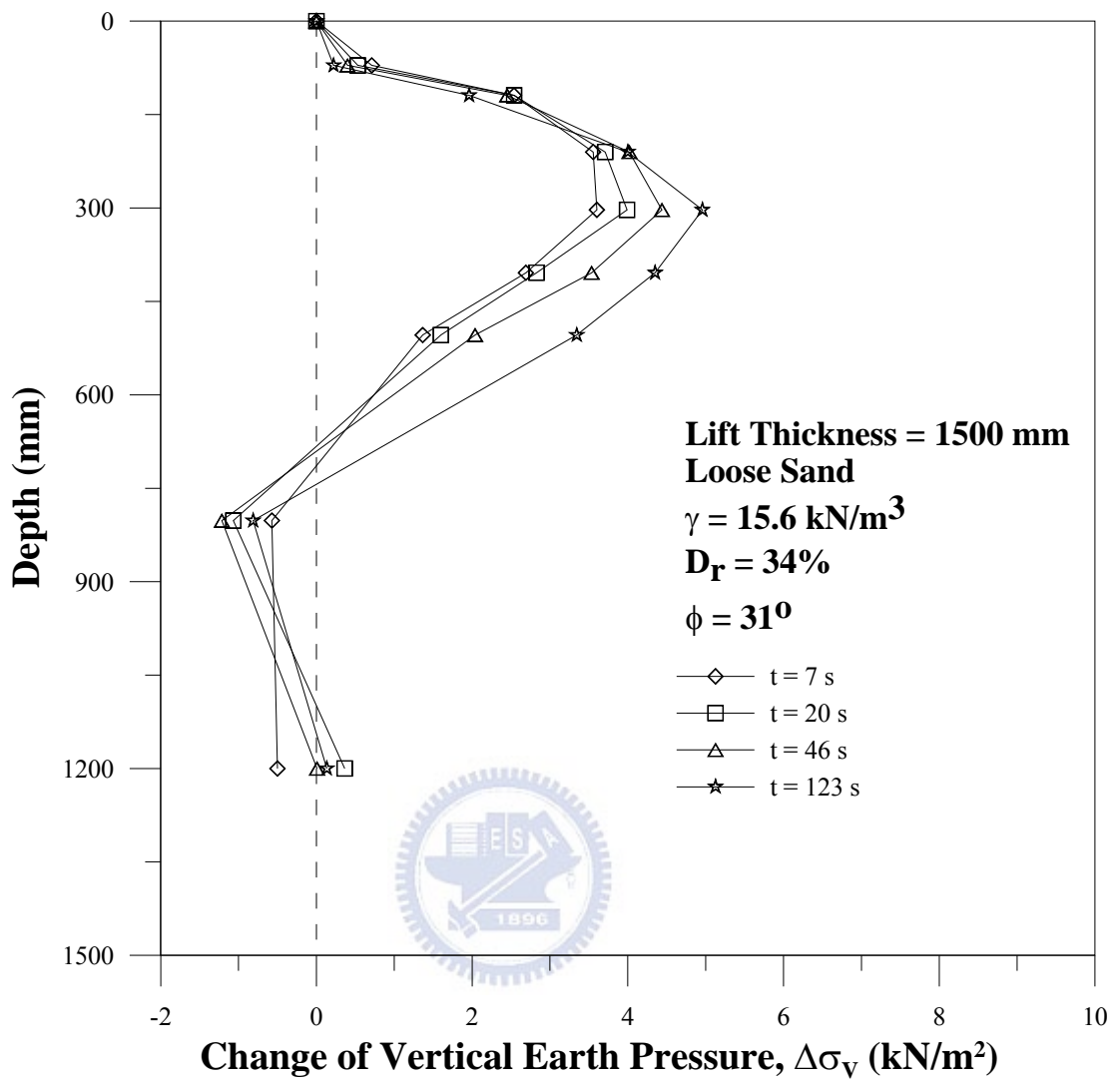


Fig. 7.3. Change of vertical earth pressure under compactor

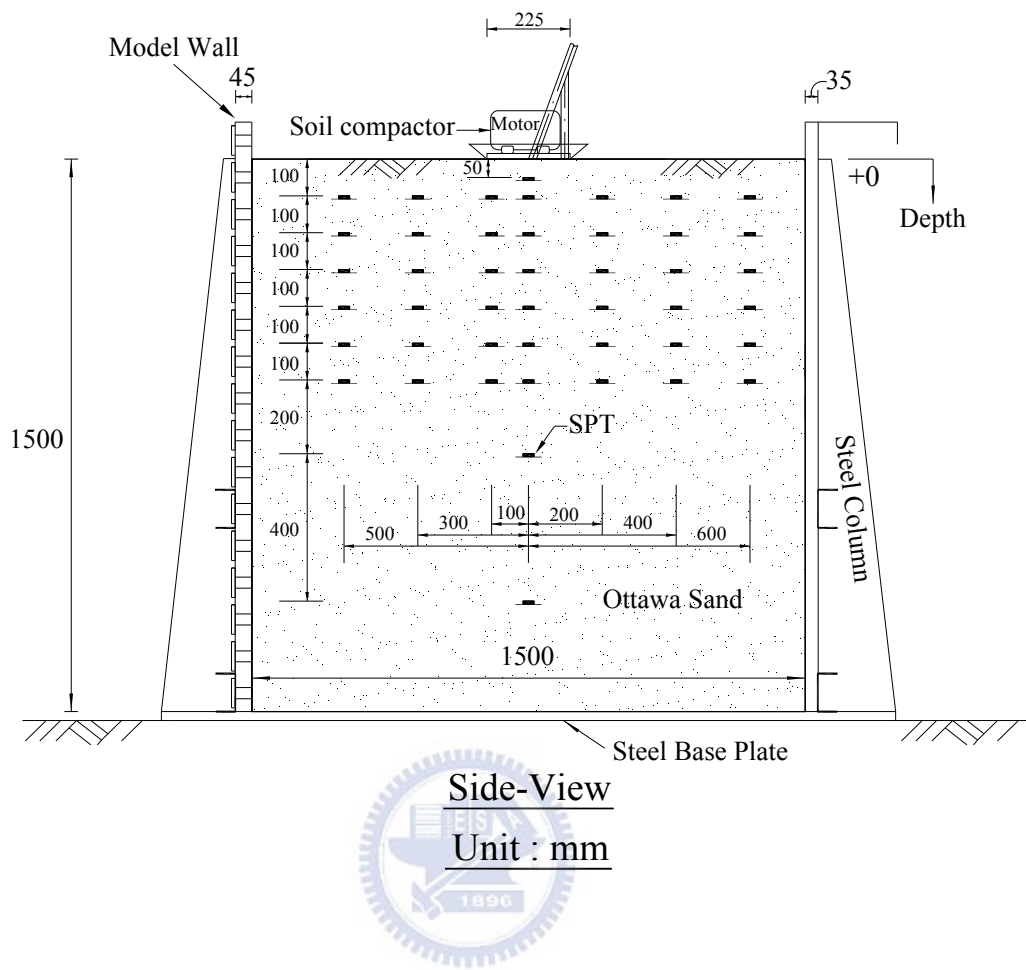


Fig. 7.4. Location of SPT to measure $\Delta\sigma_v$ (side view)

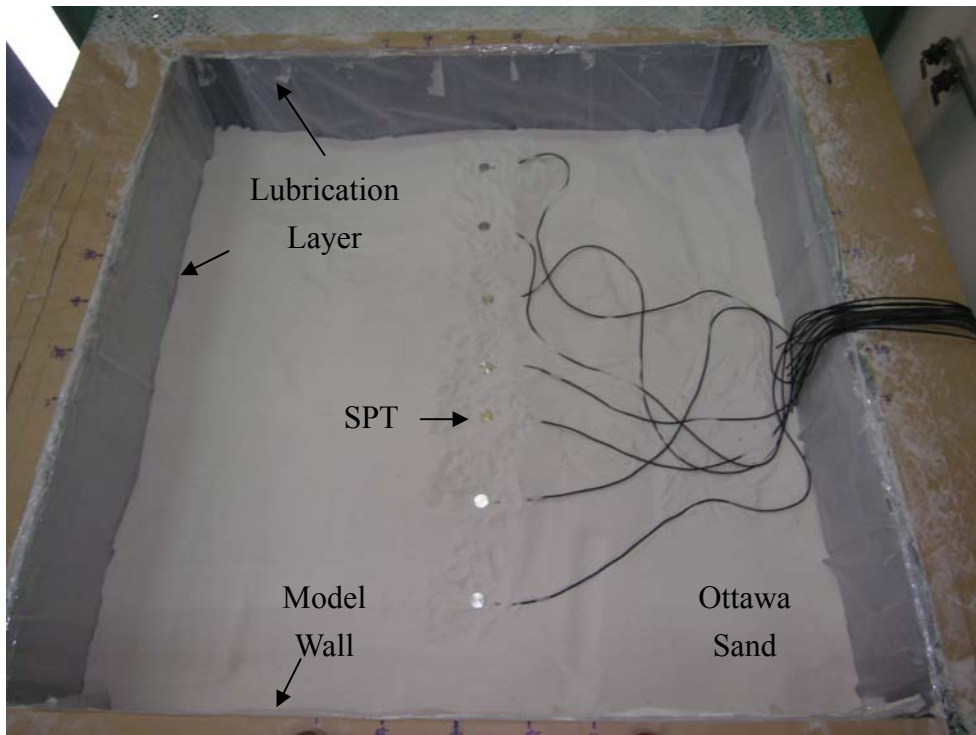
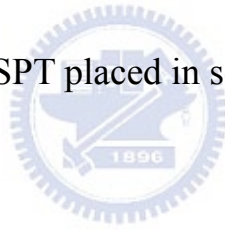


Fig. 7.5. SPT placed in soil bin (top view)



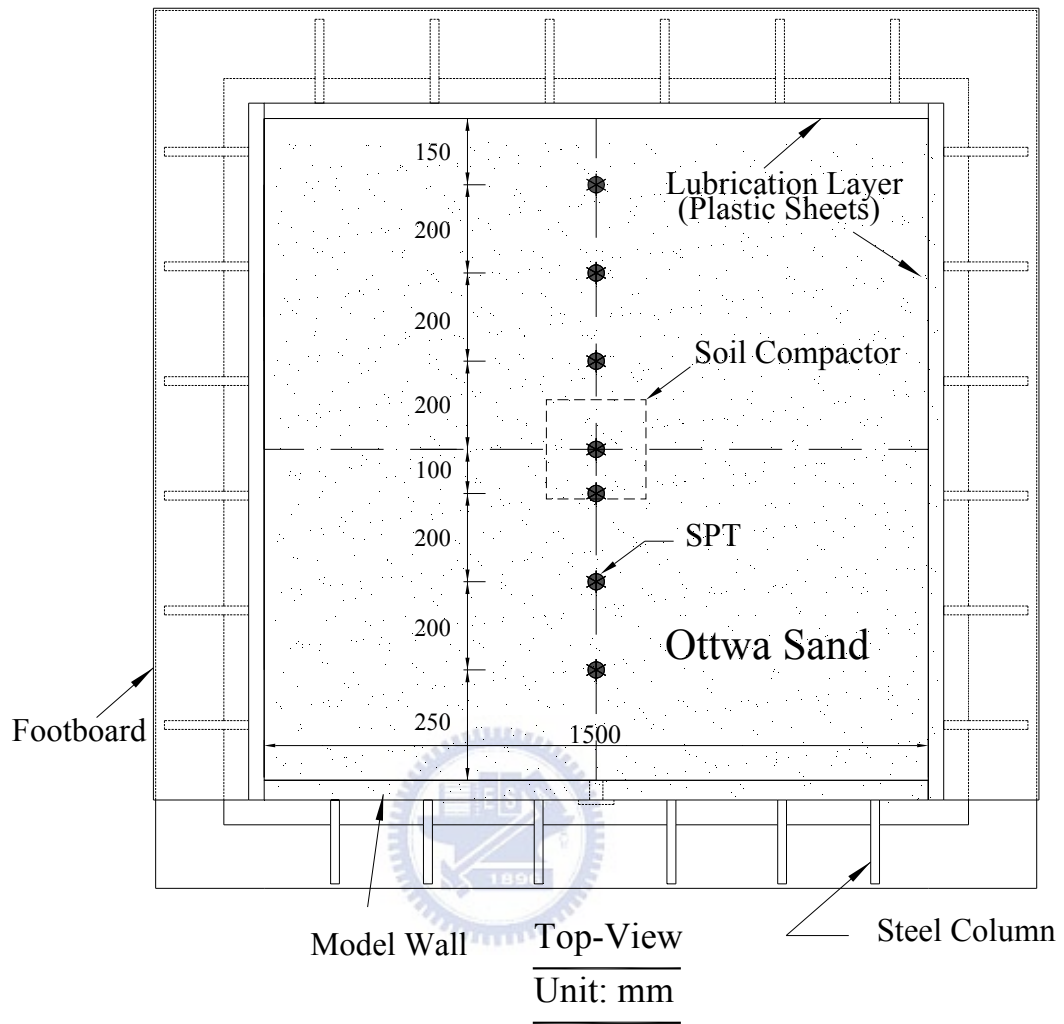


Fig. 7.6. Location of SPT to measure $\Delta\sigma_v$ (top view)

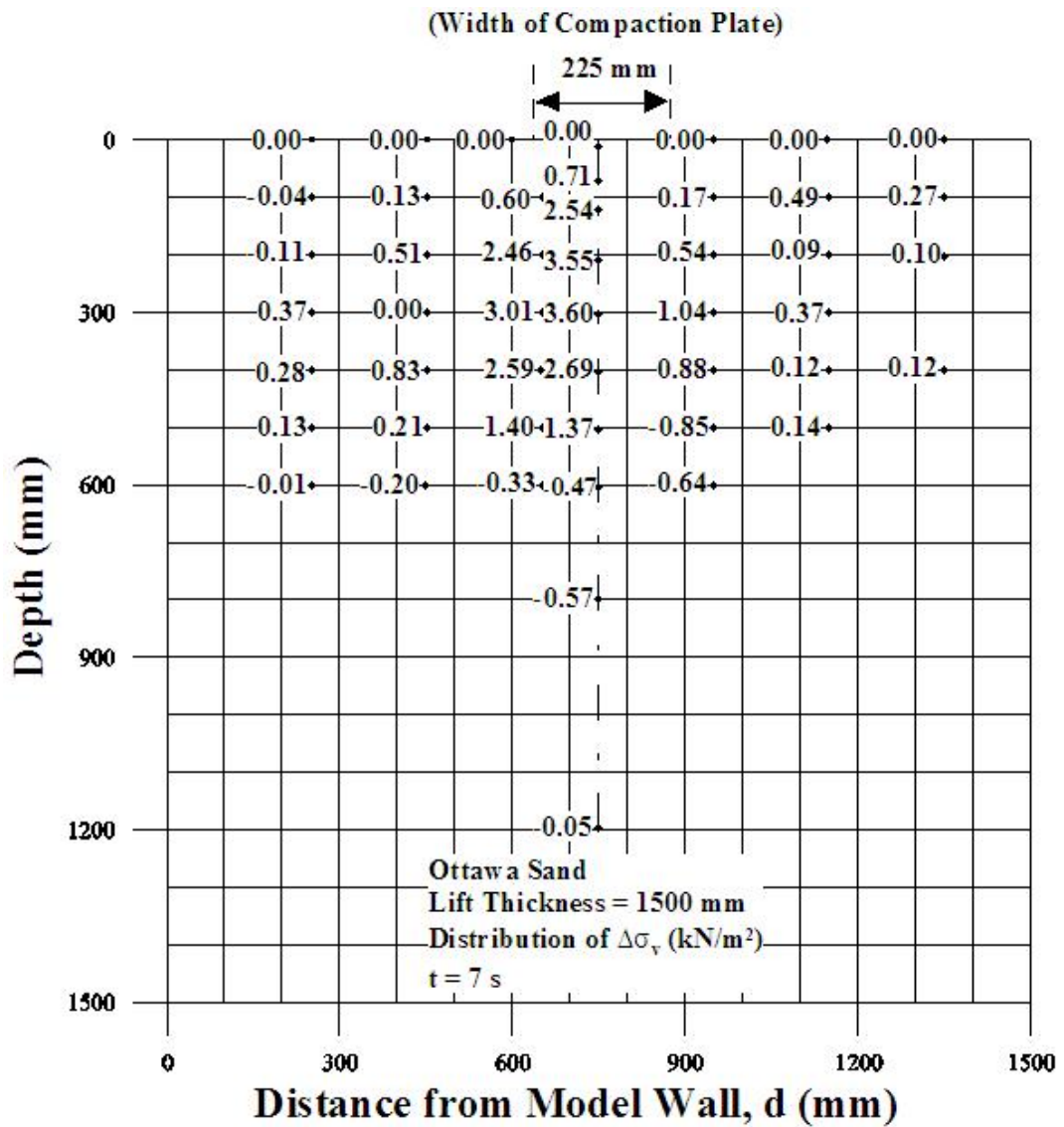


Fig. 7.7. $\Delta\sigma_v$ after 7 s of point compaction measured at grid points

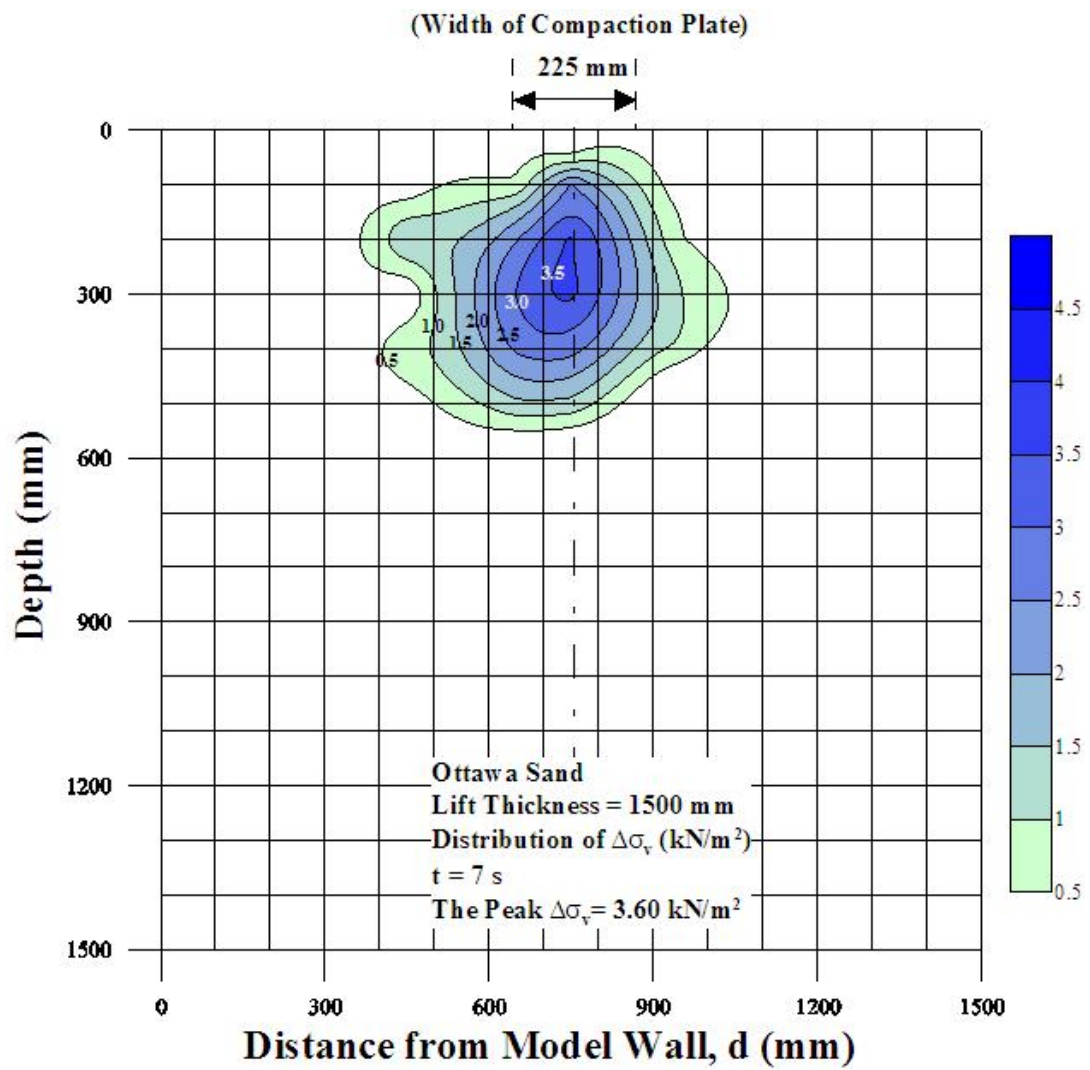


Fig. 7.8. Distribution of $\Delta\sigma_v$ after 7 s of compaction

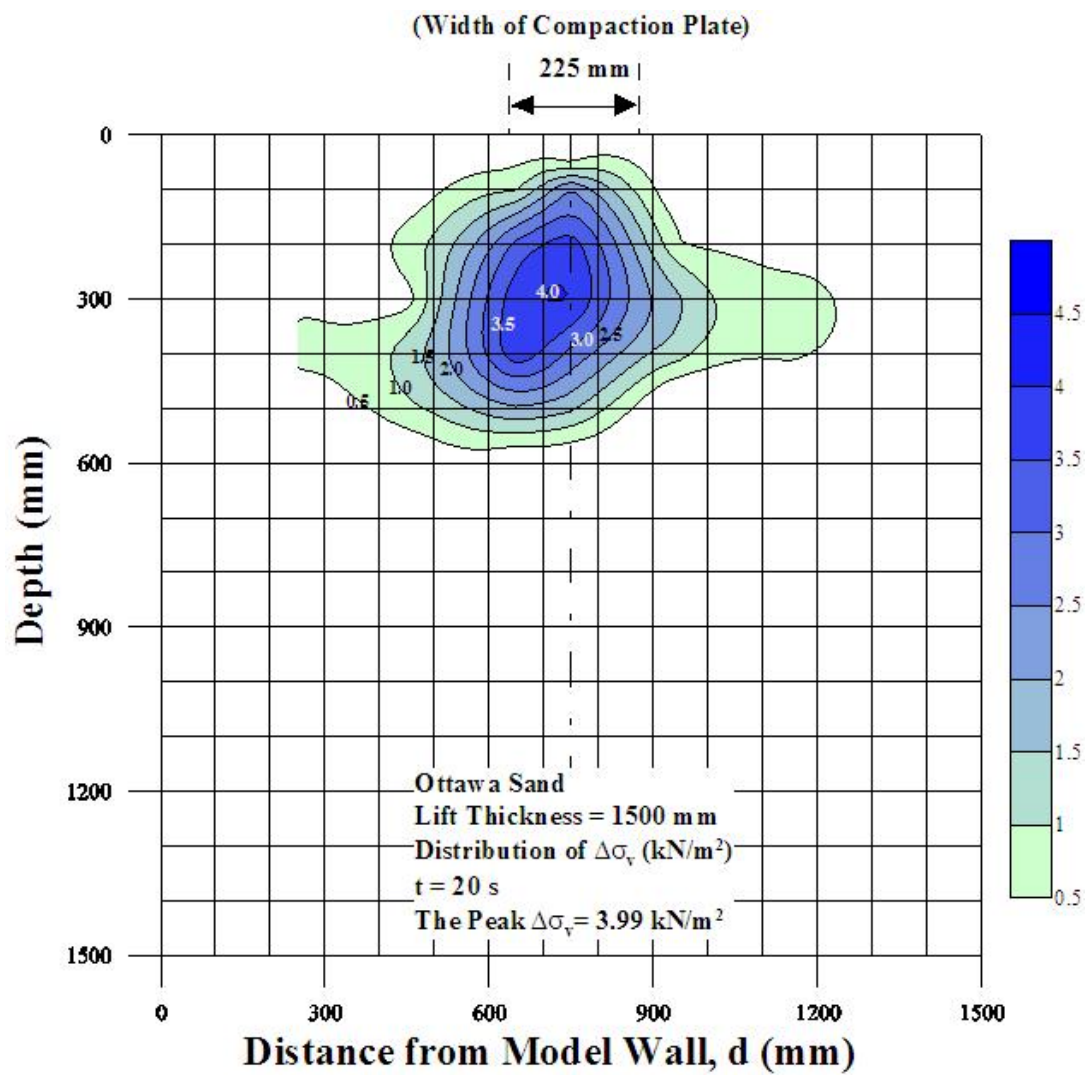


Fig. 7.9. Distribution of $\Delta\sigma_v$ after 20 s of compaction

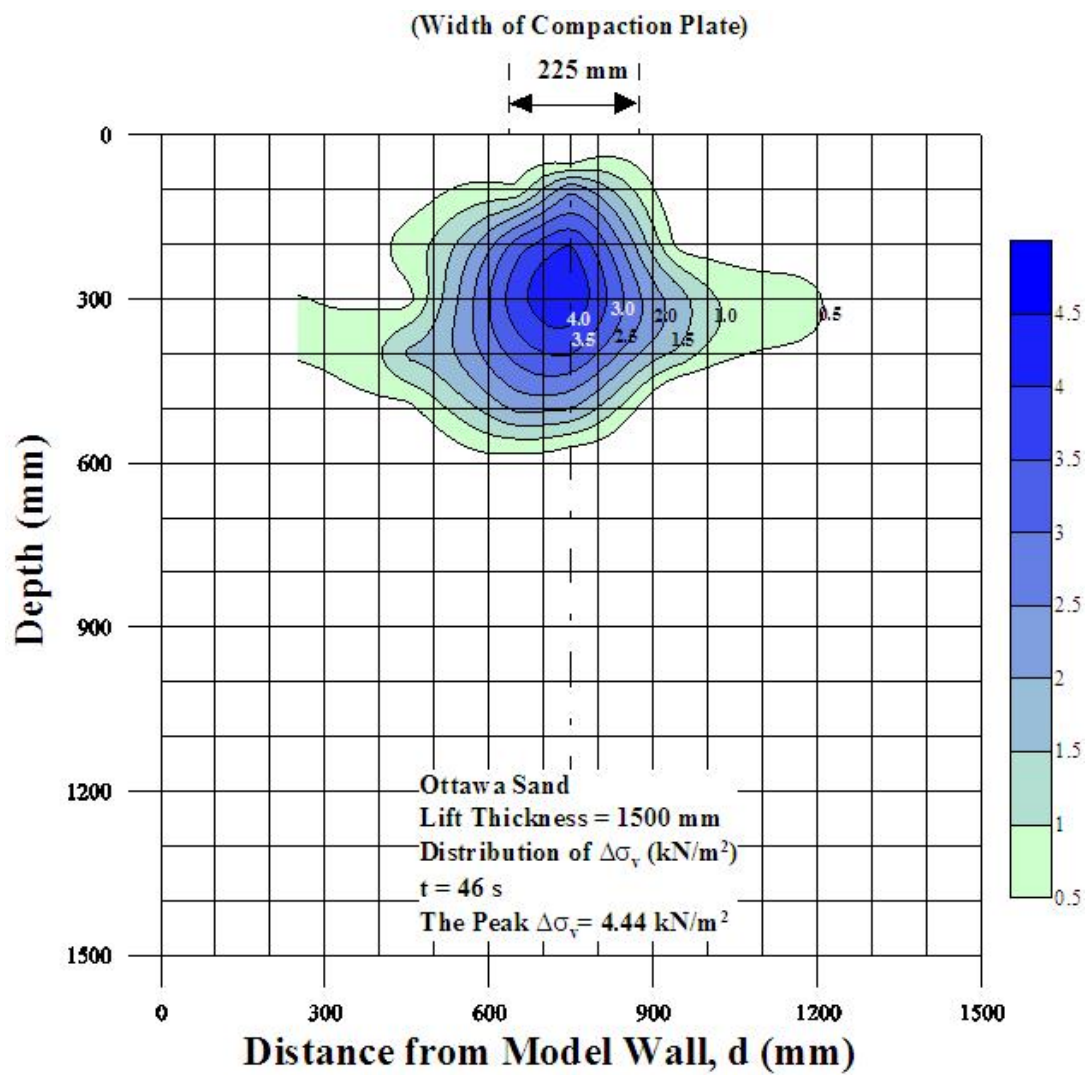


Fig. 7.10. Distribution of $\Delta\sigma_v$ after 46 s of compaction

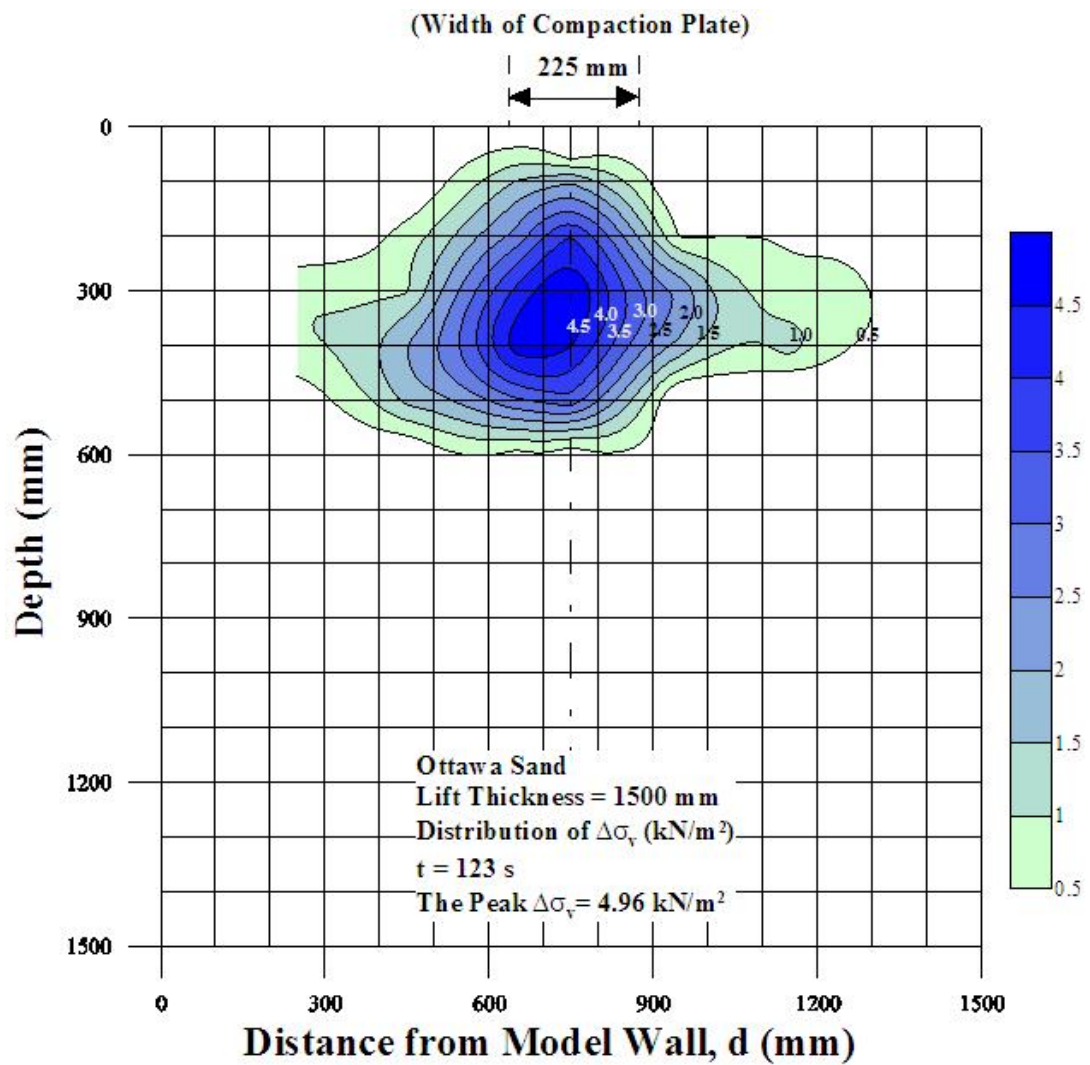


Fig. 7.11. Distribution of $\Delta\sigma_v$ after 123 s of compaction

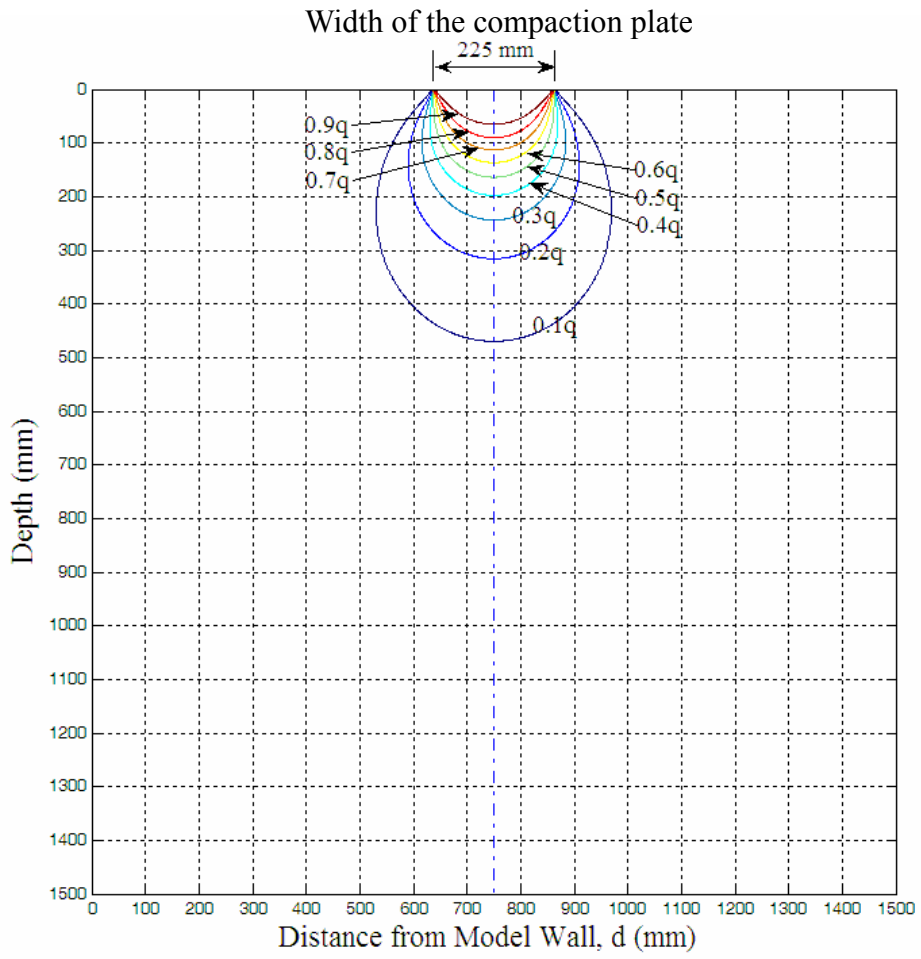
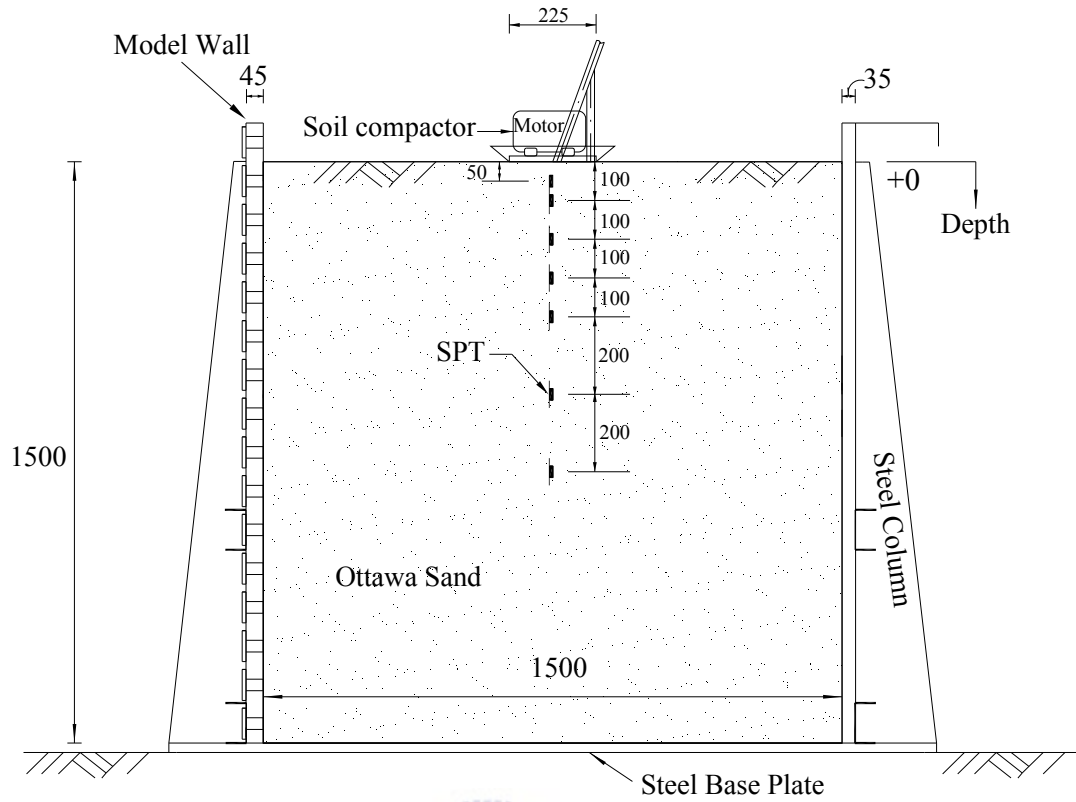


Fig. 7.12. Vertical earth pressure due to the surface Square loading q by Holl's elastic equation



Side-View

Unit : mm

Fig. 8.1. Location of SPT to measure σ_h under compactor (side view)

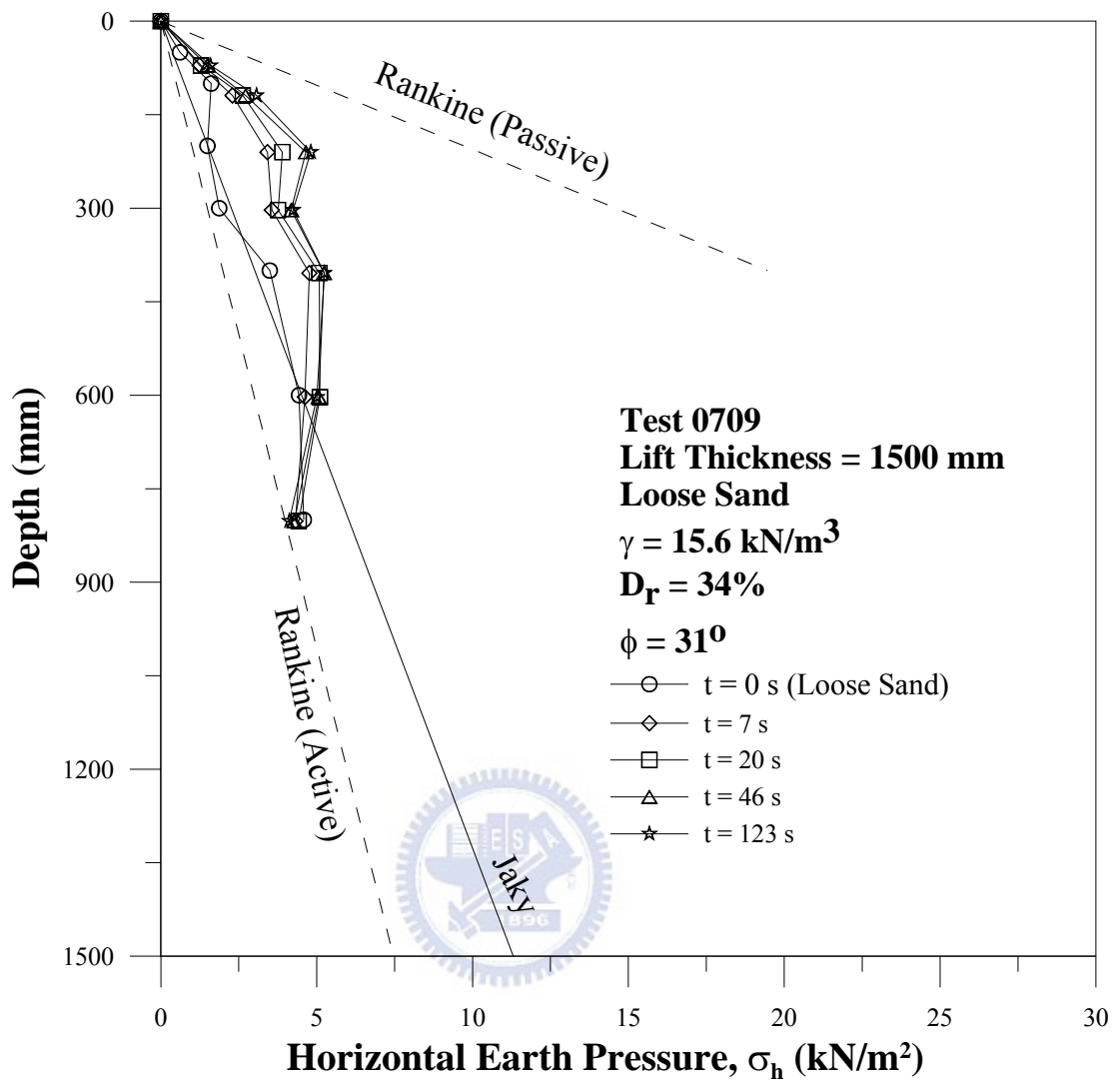


Fig. 8.2. Distributions of σ_h under compactor

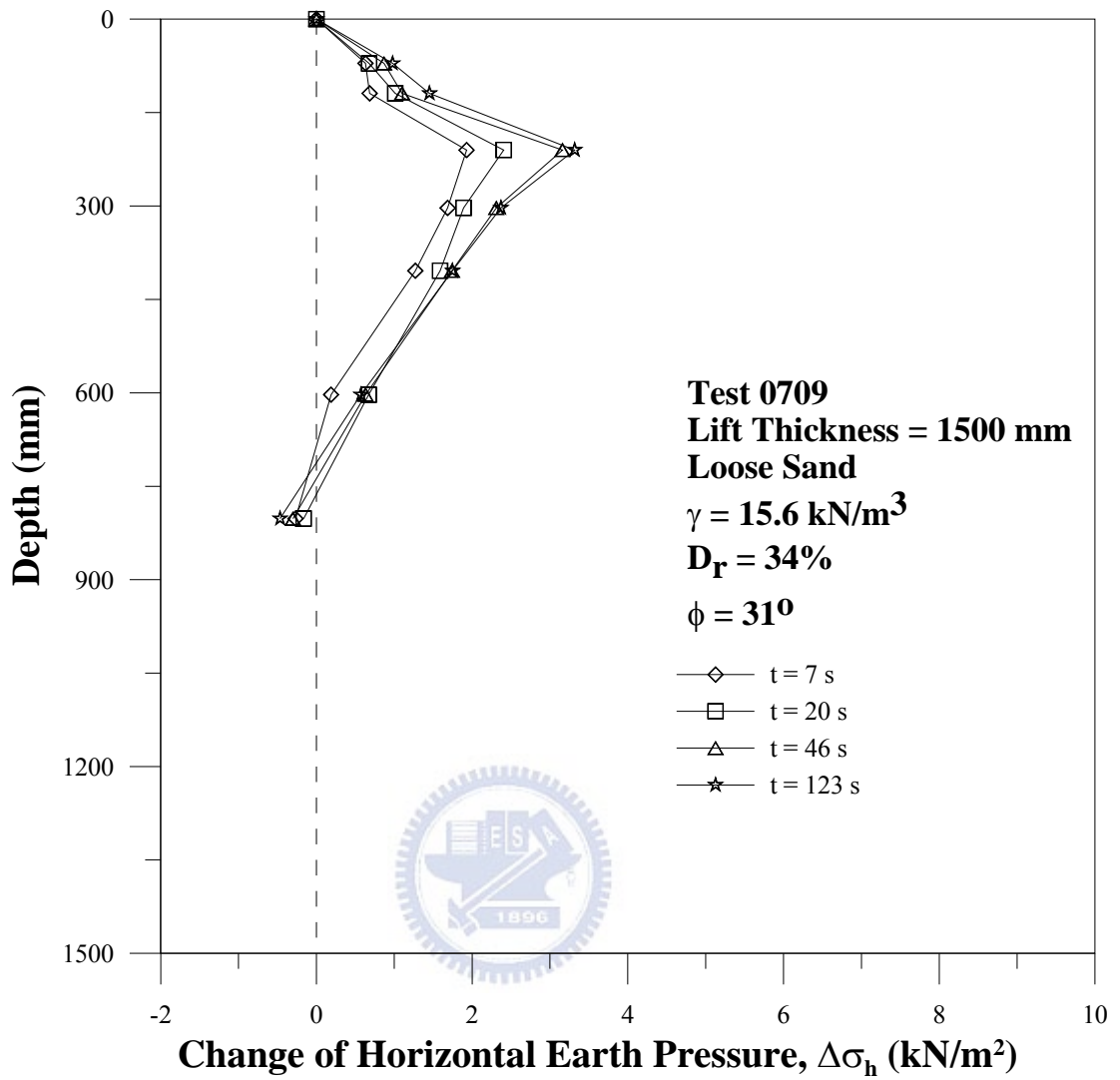


Fig. 8.3. Change of horizontal earth pressure under compactor

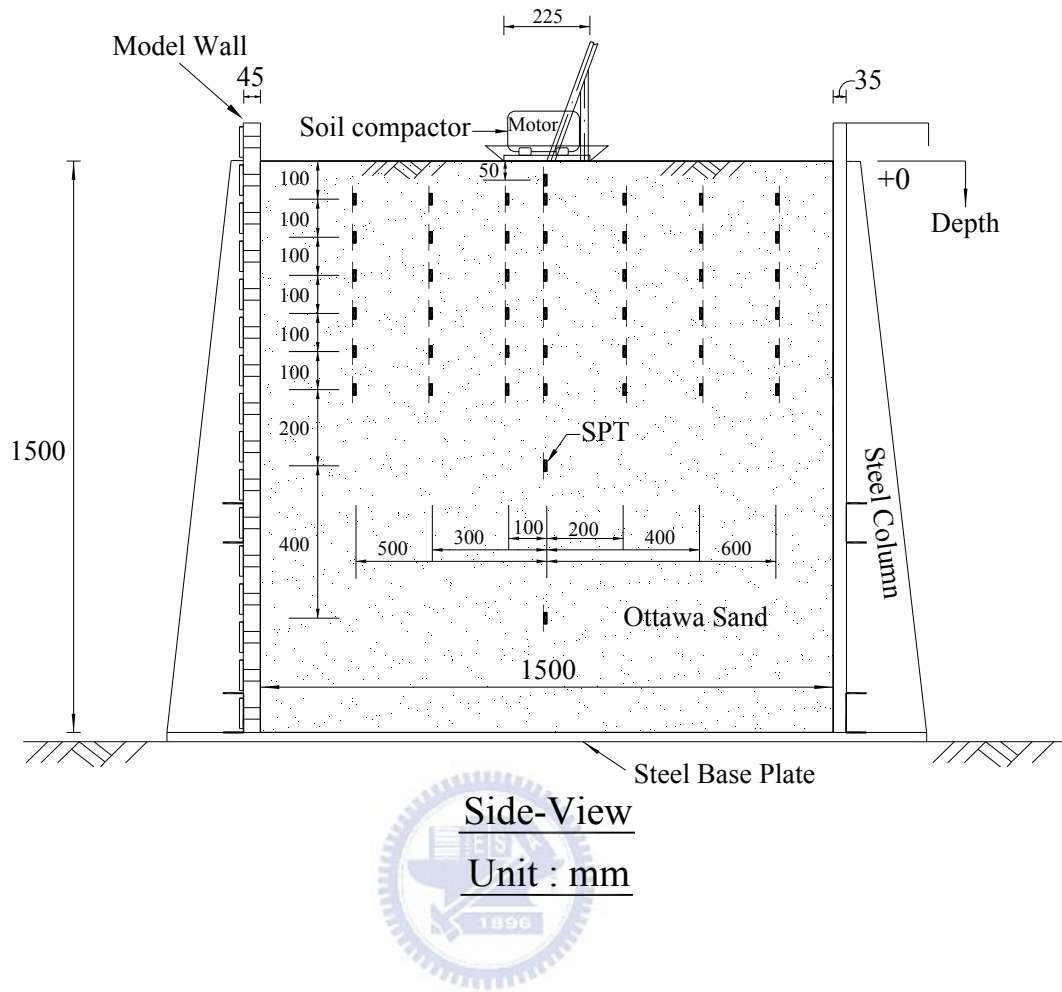


Fig. 8.4. Location of SPT to measure $\Delta\sigma_h$ (side view)

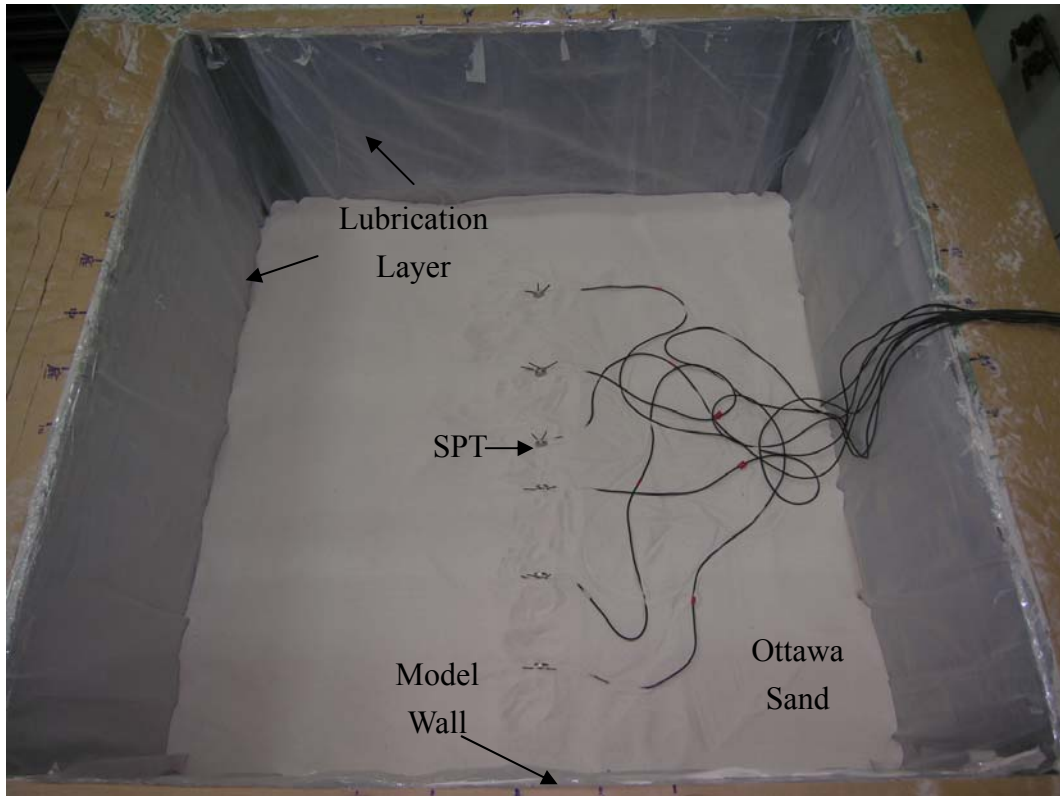


Fig. 8.5. SPT placed in soil bin (top view)



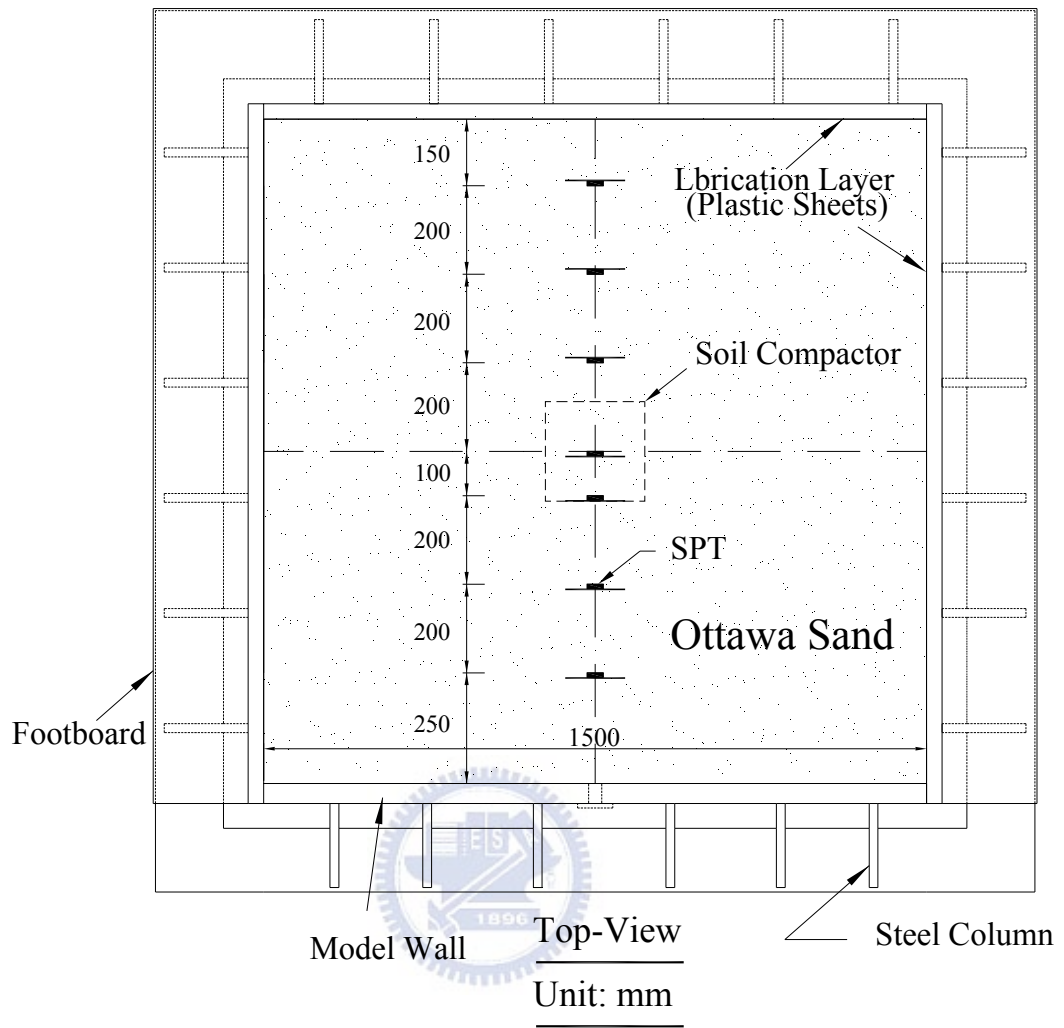


Fig. 8.6. Location of SPT to measure $\Delta\sigma_h$ (top view)

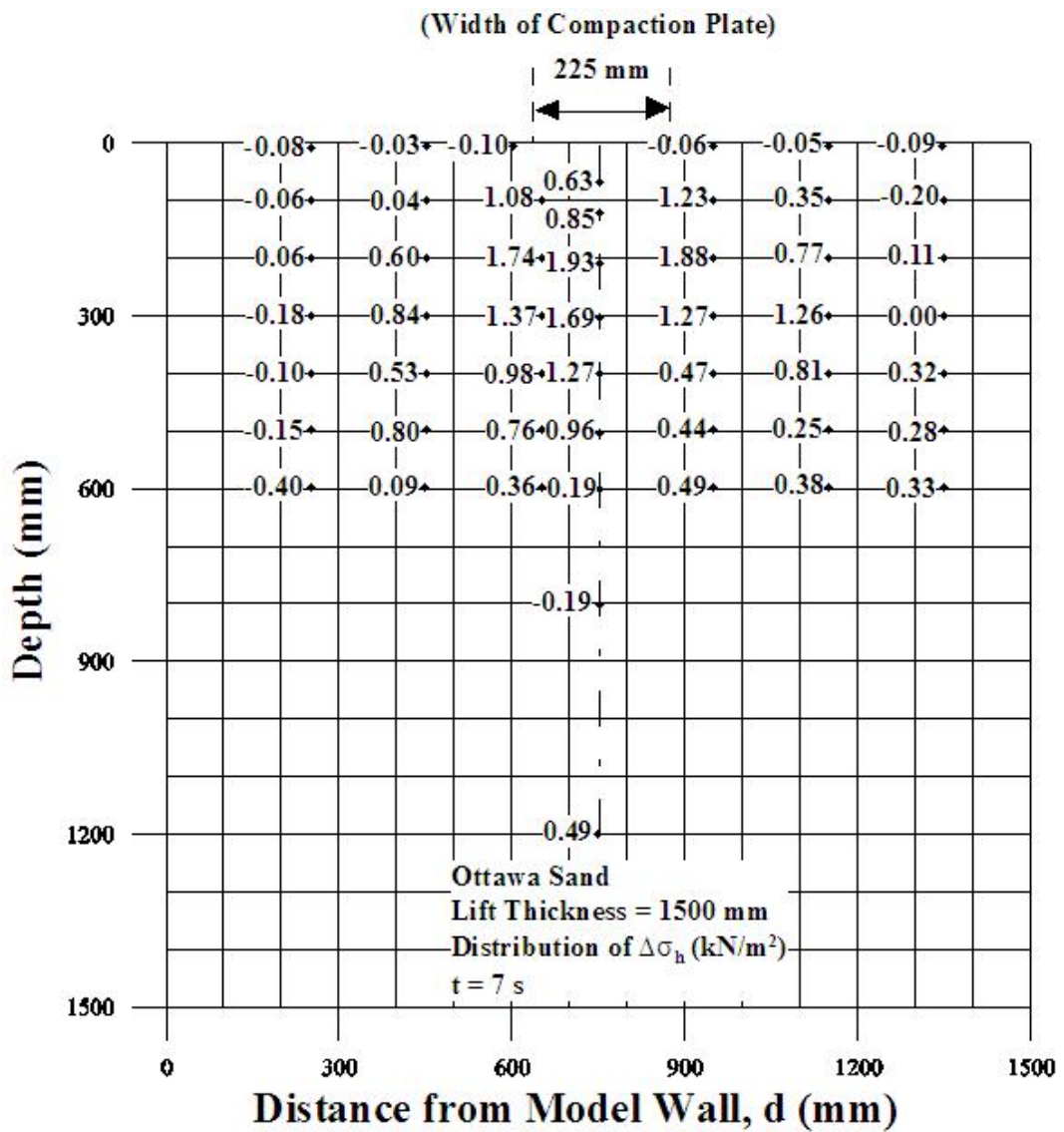


Fig. 8.7. $\Delta\sigma_h$ after 7 s of point compaction measured at grid points

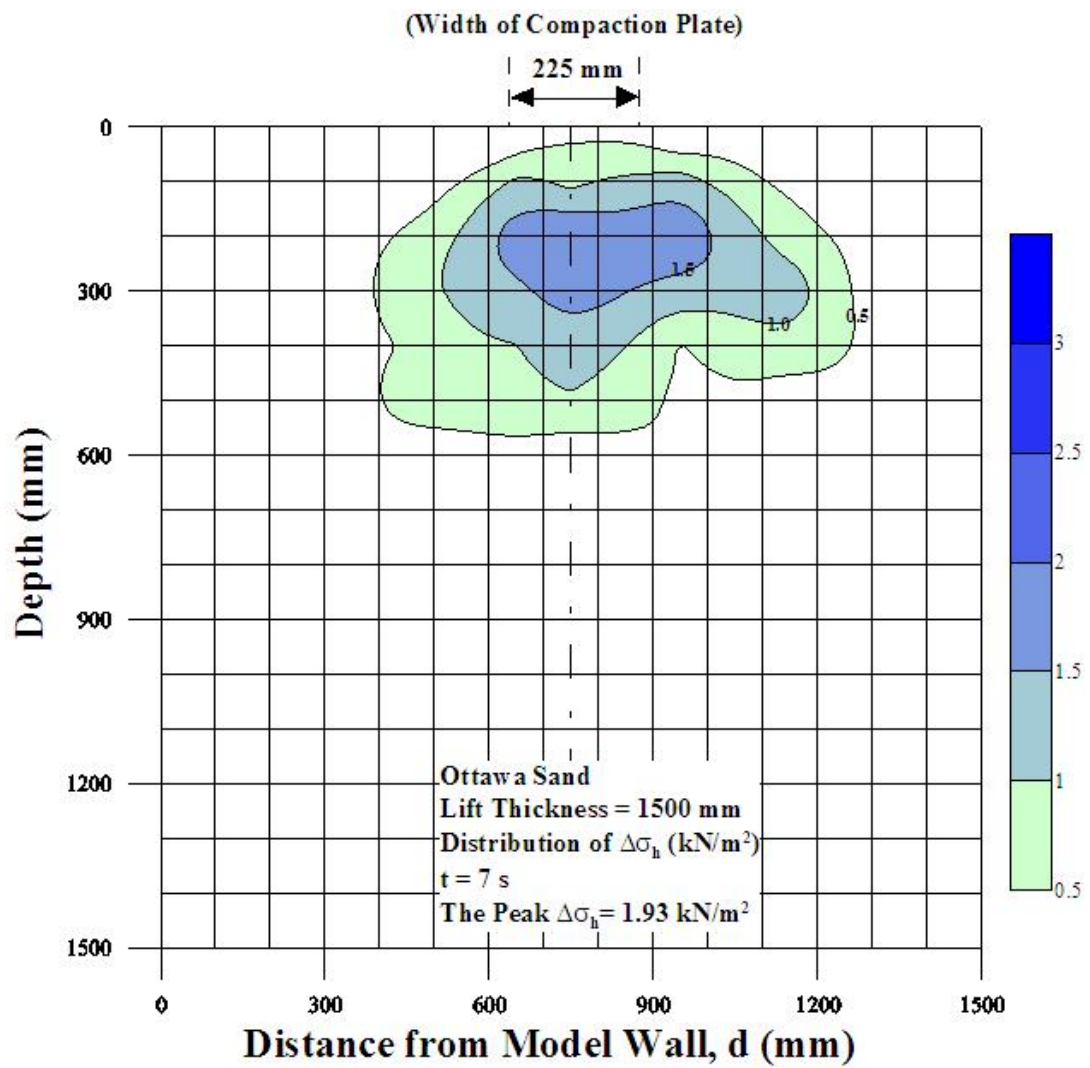


Fig. 8.8. Distribution of $\Delta\sigma_h$ after 7 s of compaction

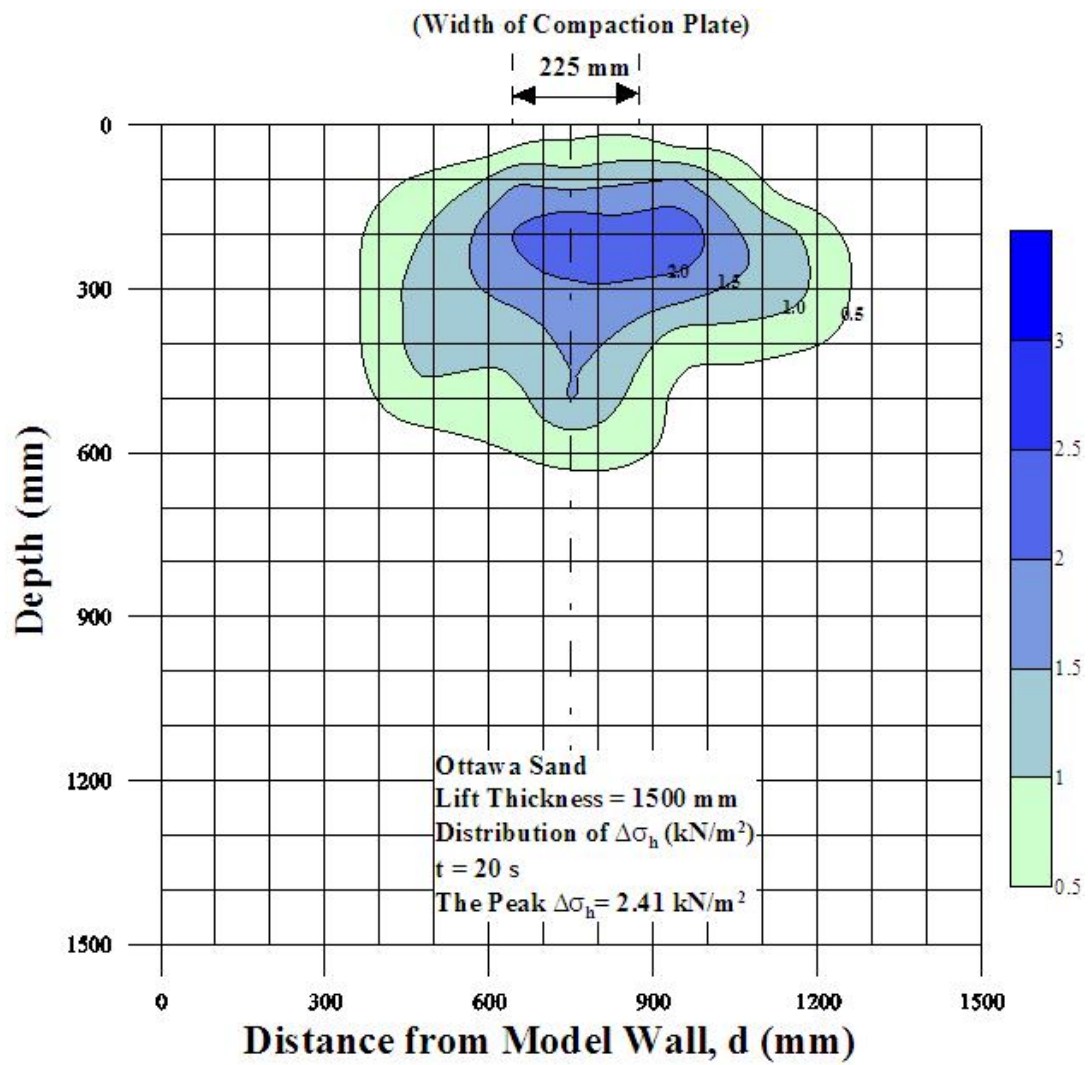


Fig. 8.9. Distribution of $\Delta\sigma_h$ after 20 s of compaction

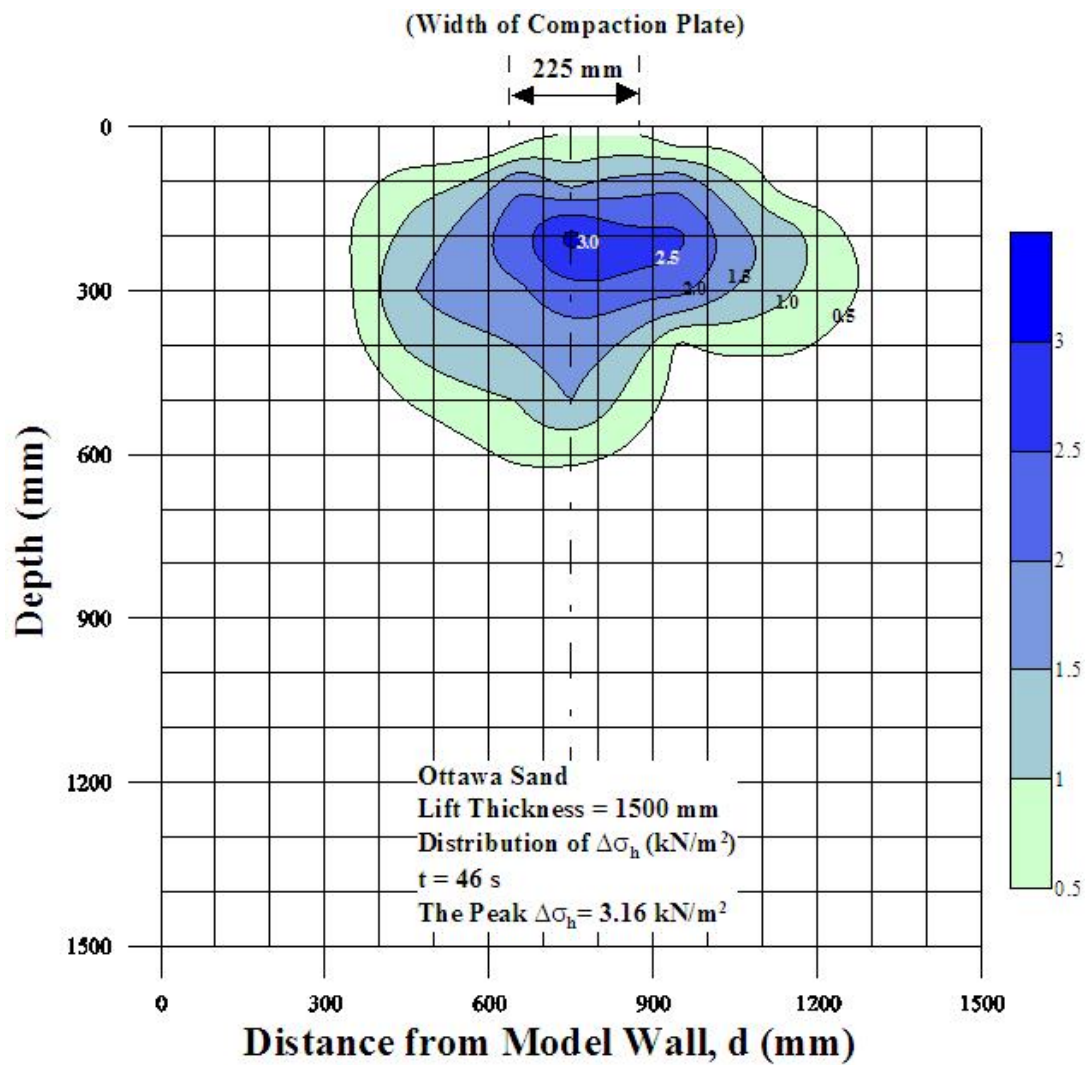


Fig. 8.10. Distribution of $\Delta\sigma_h$ after 46 s of compaction

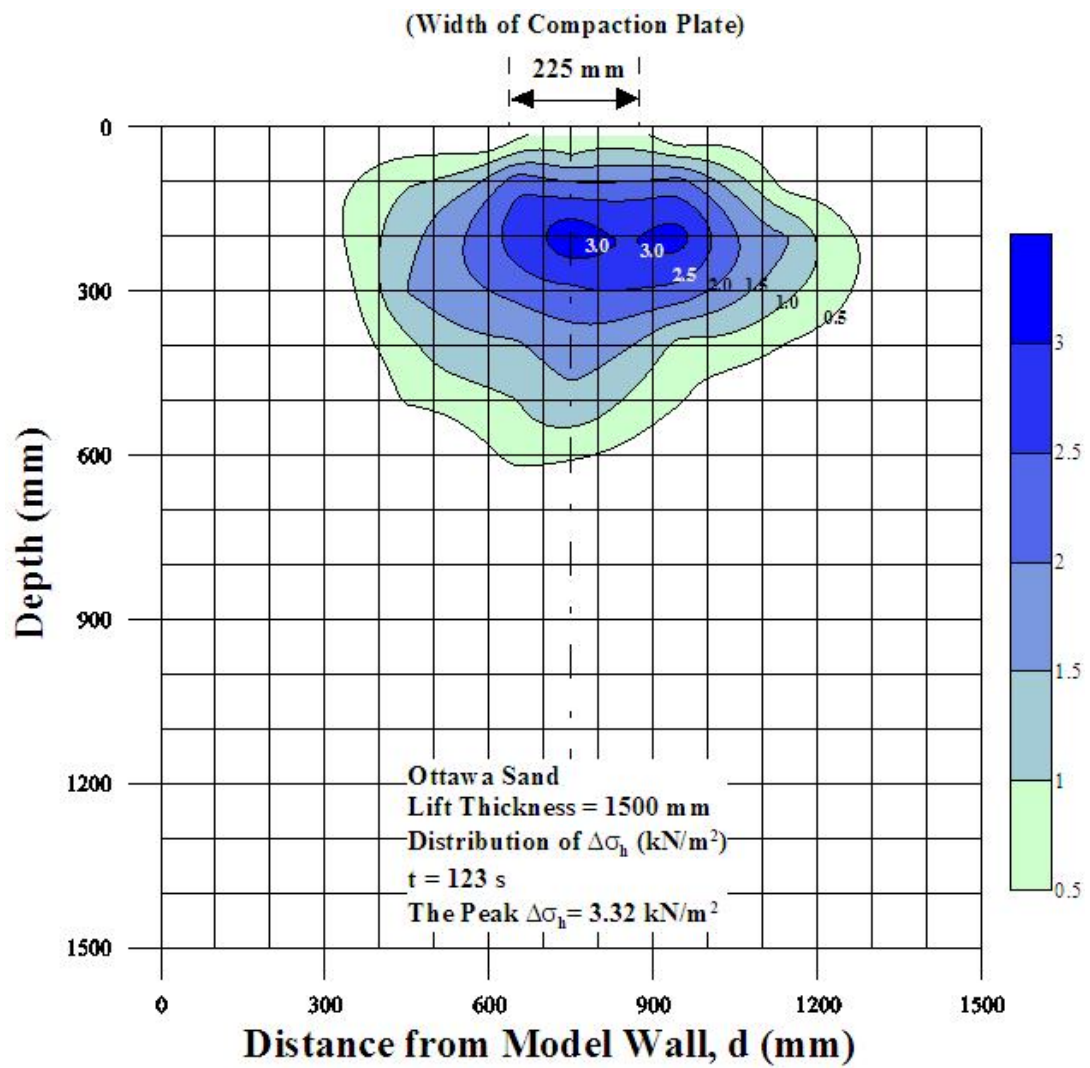


Fig. 8.11. Distribution of $\Delta\sigma_h$ after 123 s of compaction

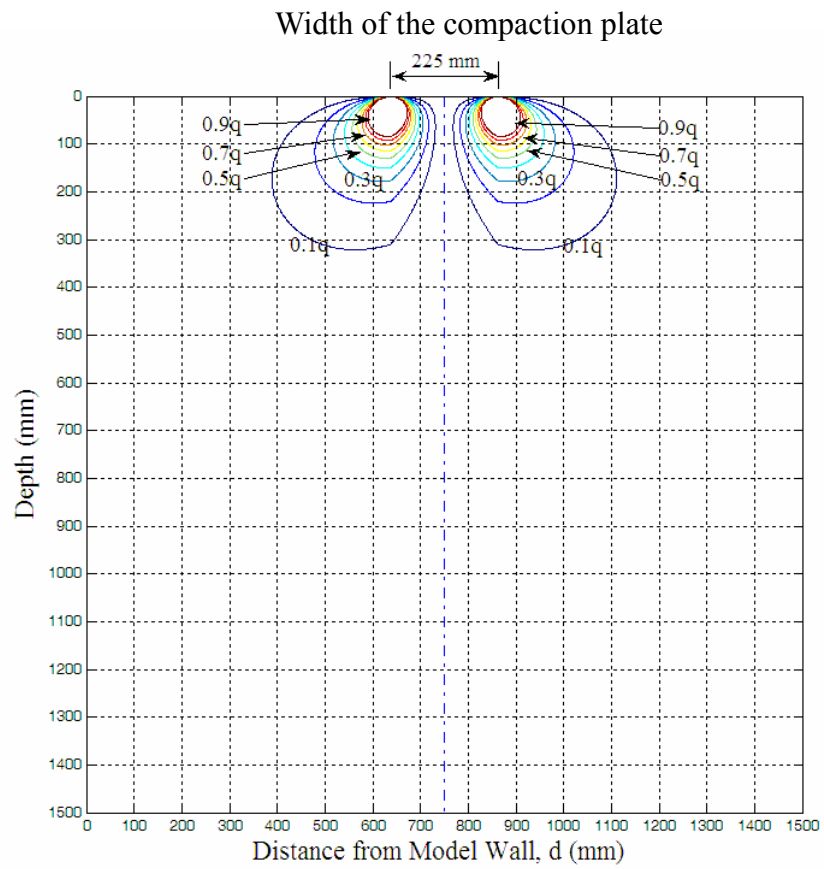


Fig. 8.12. Horizontal earth pressure due to the surface loading q by Holl's elastic equation

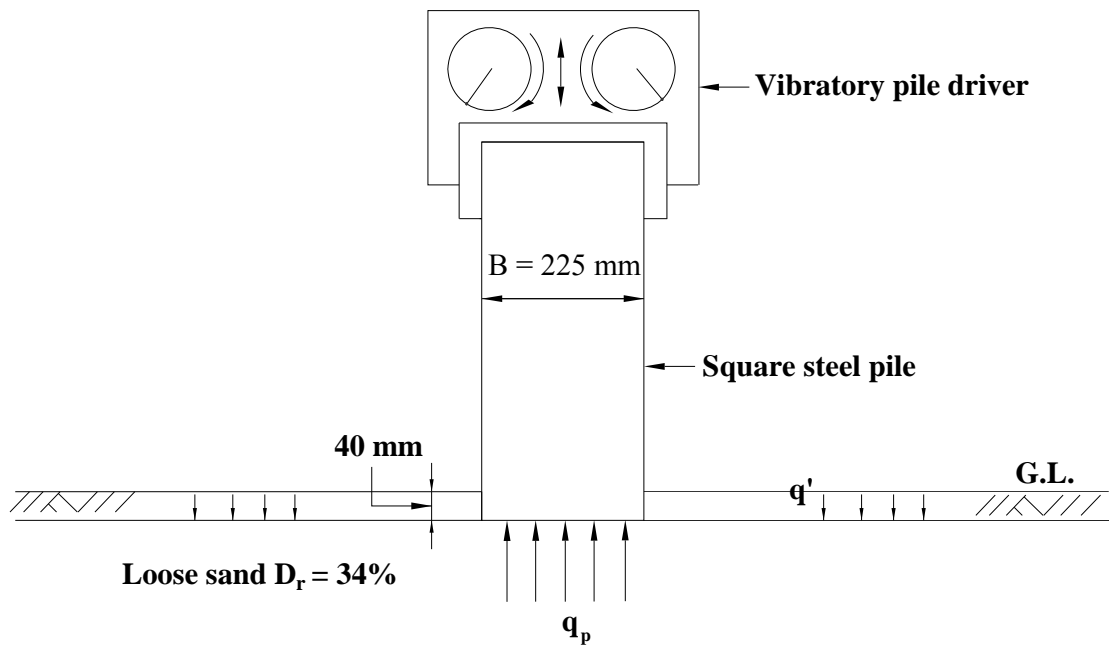
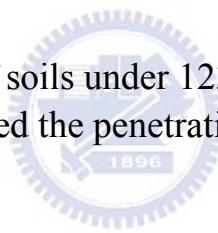


Fig. 8.13. Mechanism of soils under 123 seconds vibratory compaction liked the penetration of pile



Appendix A

CALIBRATION OF SOIL PRESSURE TRANSDUCERS

To investigate the vertical and horizontal earth pressure in the backfill, the strain-gage type of soil pressure transducers (SPT) were used. The soil pressure transducer type BE-2KCM17 manufactured by KYOWA has an effective diameter of 22 mm and was embedded in the backfill to monitor the earth pressure variation in the soil mass. Since the pressure acts between soil particles and the transducer is quite different from the pressure that acts between liquid and transducer, it is necessary to calibrate the transducer in an environment similar to that for the actual testing condition. The system was designed for the calibration of in soil transducers. The system consists of the calibration device, air-pressure control system, signal conditioner, and data acquisition system, as indicated in Fig. A.1. The typical photograph of the system is shown in Fig. A.2.

Dunnicliff (1988) described that, if measurement accuracy must be maximized, each cell should be calibrated in a large calibration chamber, using the soil in which it will be embedded. The chamber should be at least 3 times, and preferably 5 times the diameter of the cell. Following Dunnicliff's recommendation, the calibration devices shown in Fig. A.3 is a shallow cylindrical chamber with an inner diameter of 400 mm and a height of 30 mm and is made of a solid steel plate, which is the same material as the model retaining wall.

To avoid point load effects, Weiler and Kulhawy (1982) concluded that the ratio of the active diaphragm to the mean soil grain size, d/D_{50} , needs to be greater than or

equal to 10. In this study, the diameters of active diaphragm of the transducers, BE-2KCM17 is 22 mm. The mean soil grain size of Ottawa sand is $D_{50} = 0.36$ mm. The ratio $d/D_{50} = 61$ is apparently greater than the required ratio of 10. In this study, the eccentric, non-uniform and point load conditions will not occur during calibration.

To calibrate the in-soil transducer, as indicated in Fig. A.1, a thin layer of sand was placed into the chamber to form a sand bed then the soil pressure transducer was placed on the sand bed. On top of the transducer, a 10 mm-thick sand layer was placed in the calibration device. Then the 0.2 mm-thick rubber membrane was placed over the sandy layer. As indicated in Fig. A.1, a uniformly distributed air-pressure was applied on the membrane, carried-over through the soil particles, and transmitted to the transducer.

In Fig. A.1, rubber O-rings were arranged to prevent air leakage between the chamber and the cap. It should be noted that the air pressure applied for the calibration of transducer should be consistent with the operating pressure range for model wall experiments. For this study, the transducers calibrated for the pressure range of $0 \sim 9.81 \text{ kN/m}^2$ or $0 \sim 98.1 \text{ kN/m}^2$ were mainly measured the horizontal and vertical earth pressure in the soil mass, respectively. To reduce the effect of sidewall friction, the thickness of sand layer in the chamber should be limited, so that the side-friction between the sand the sidewall of the chamber could be minimized.

The typical calibration test results is shown in Fig. A.3 to Fig. A.10. It is obvious that the output voltage of the transducer measured by the data acquisition system increases linearly with increasing applied pressure. Table A.1 and A.2 summarizes of the calibration factors of soil pressure transducers used in this study.

Table A.1. Soil Pressure Transducer Calibration Factors

Type	Transducer No.	Dynamic Strain Amplifier		Capacity (kN/m ²)	Calibration Function P=[Factor]*V (kN/m ²)
		No.	Calibration Setter($\mu \xi$)		
BE-2KCM17	090170001	1	283	98.1	P=38.222V
BE-2KCM17	090170002	2	275	98.1	P=38.012V
BE-2KCM17	090170003	3	302	98.1	P=37.284V
BE-2KCM17	090170004	4	288	98.1	P=37.816V
BE-2KCM17	090170005	5	282	98.1	P=38.097V
BE-2KCM17	090170006	6	289	98.1	P=37.472V
BE-2KCM17	090170007	7	300	98.1	P=38.343V
BE-2KCM17	090170008	8	269	98.1	P=37.534V

Calibration pressure range : 0~98.1 kN/m²

Table A.2. Soil Pressure Transducer Calibration Factors

Type	Transducer No.	Dynamic Strain Amplifier		Capacity (kN/m ²)	Calibration Function P=[Factor]*V (kN/m ²)
		No.	Calibration Setter($\mu \xi$)		
BE-2KCM17	9Z0080001	9	305	98.1	P=18.303V
BE-2KCM17	9Z0080002	10	340	98.1	P=17.684V
BE-2KCM17	9Z0080003	11	345	98.1	P=19.821V
BE-2KCM17	9Z0080004	12	350	98.1	P=18.510V
BE-2KCM17	9Z0080005	13	333	98.1	P=20.209V
BE-2KCM17	9Z0080006	14	316	98.1	P=19.923V
BE-2KCM17	9Z0080007	15	378	98.1	P=20.825V
BE-2KCM17	9Z0080008	16	325	98.1	P=19.552V

Calibration pressure range : 0~9.81 kN/m²

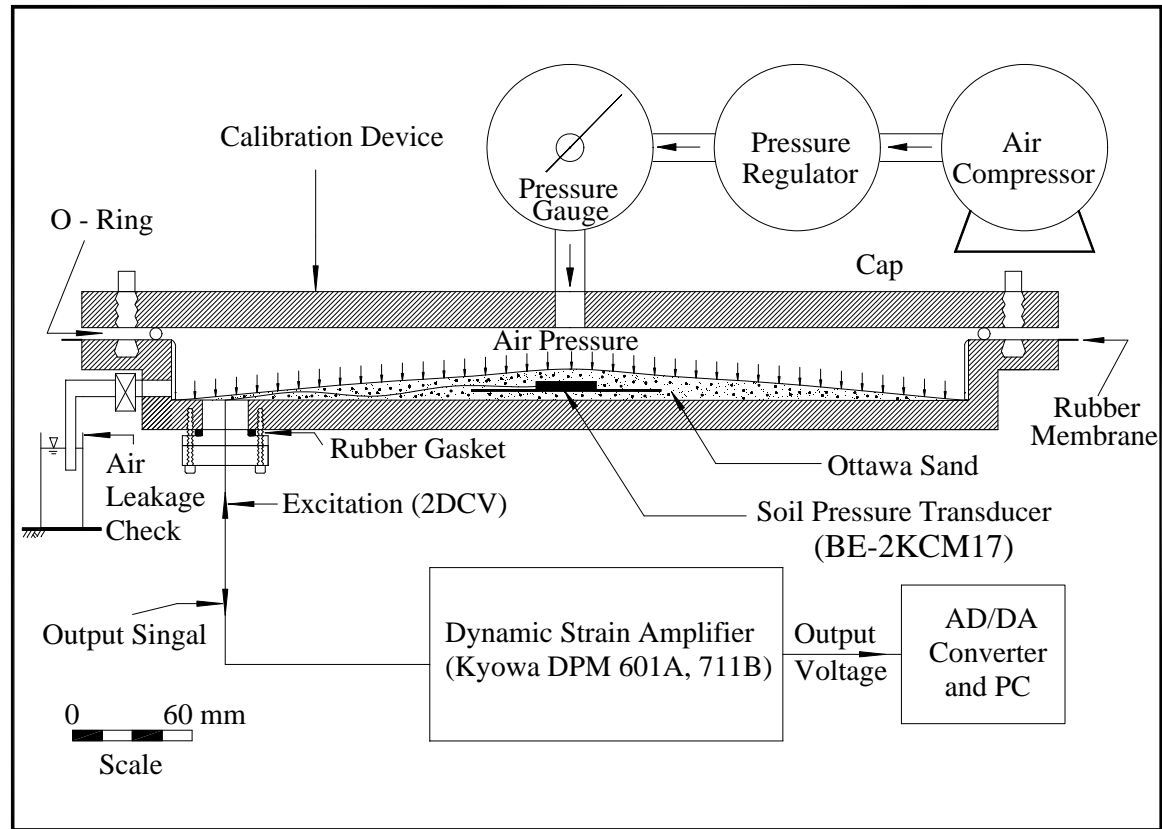


Fig. A1. Schematic diagram of in-soil soil pressure transducer calibration system

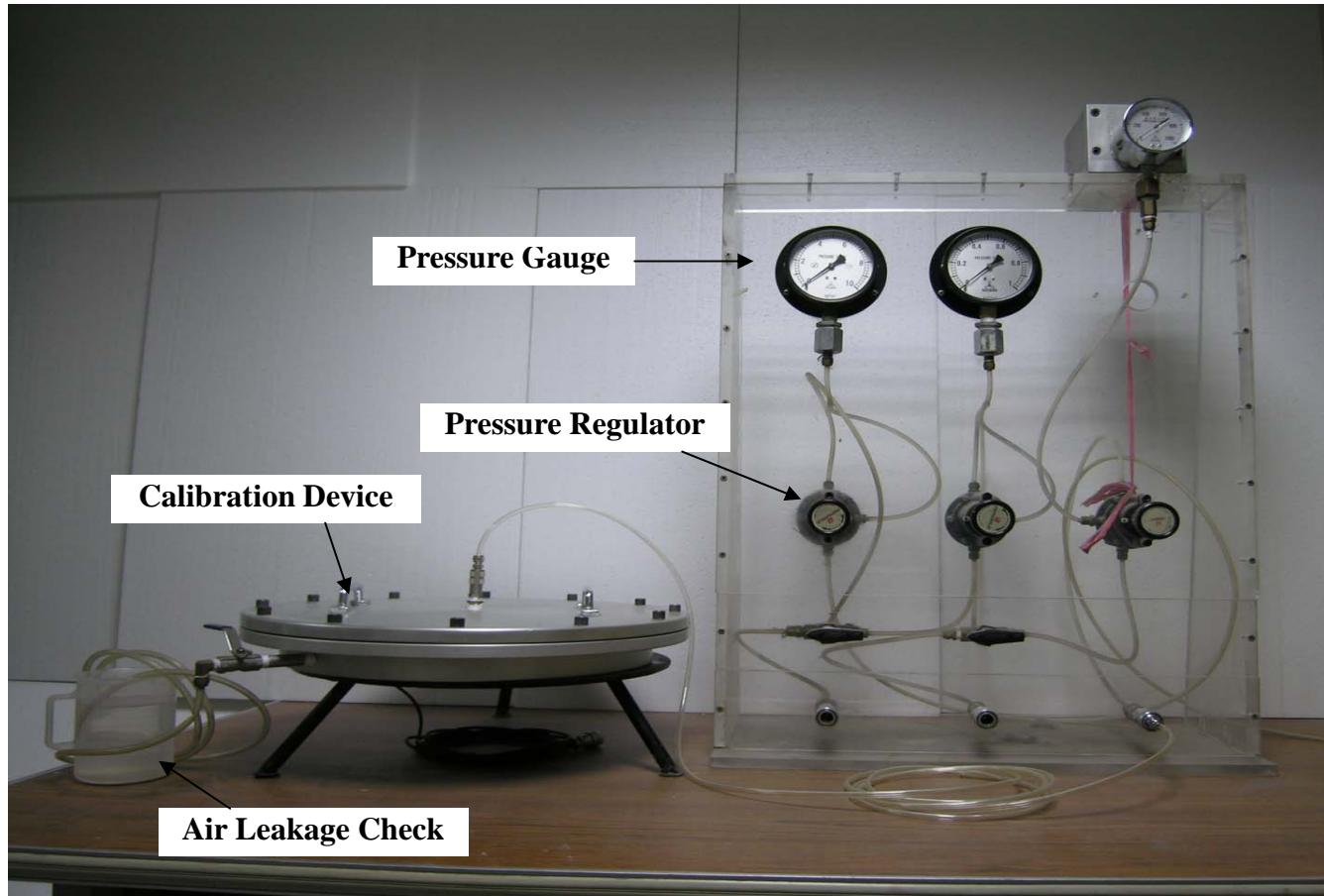


Fig. A.2. Photograph of soil pressure transducer calibration system

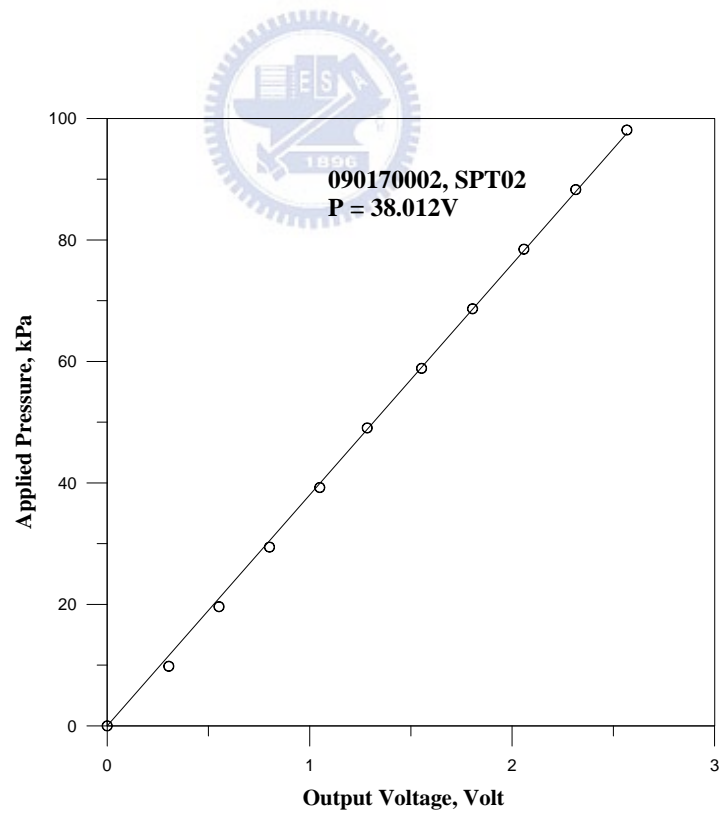
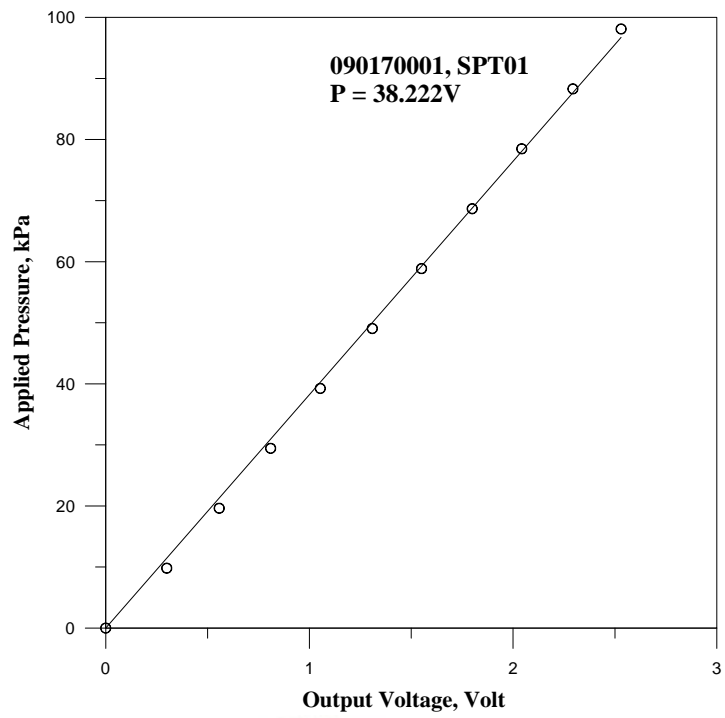


Fig. A.3. Applied pressure versus voltage output for soil pressure transducer SPT01 and SPT02

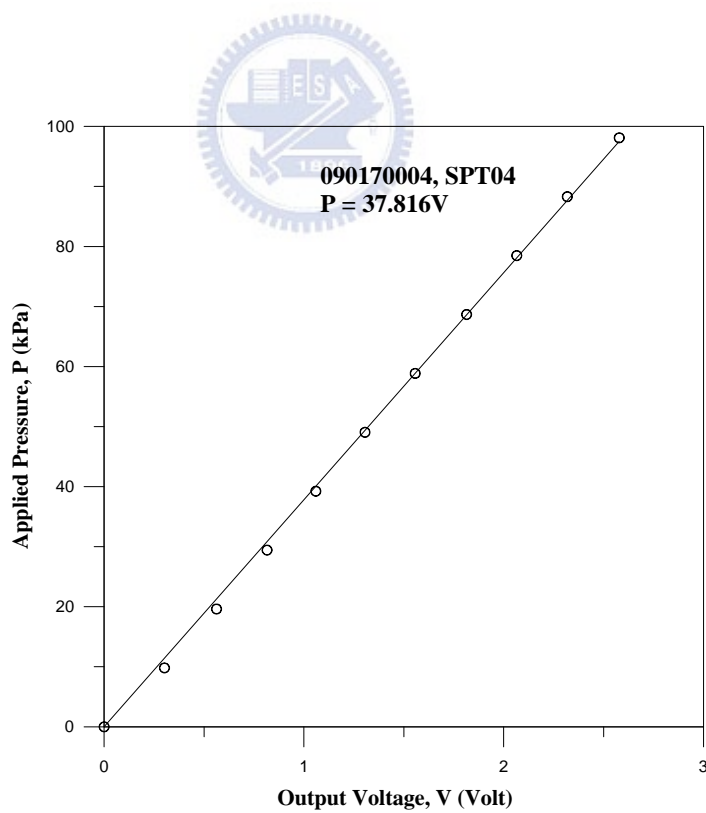
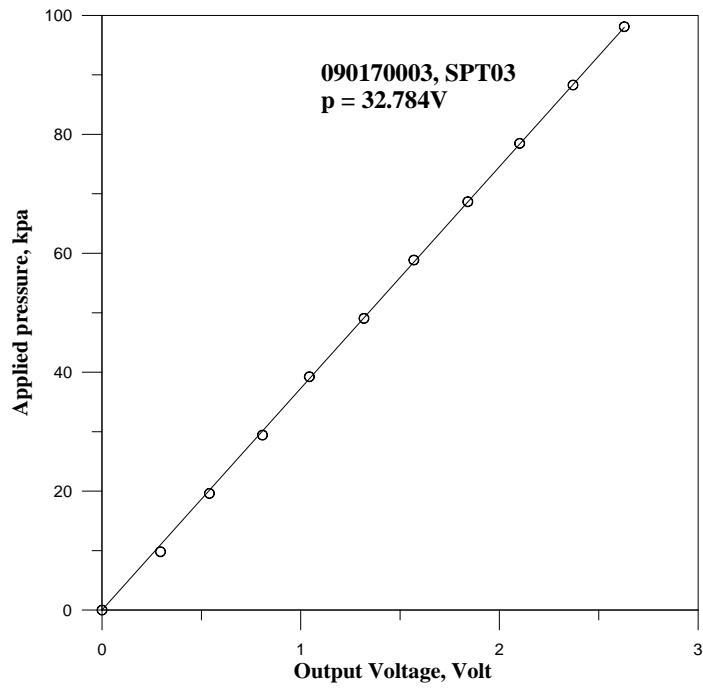


Fig. A.4. Applied pressure versus voltage output for soil pressure transducer SPT03 and SPT04

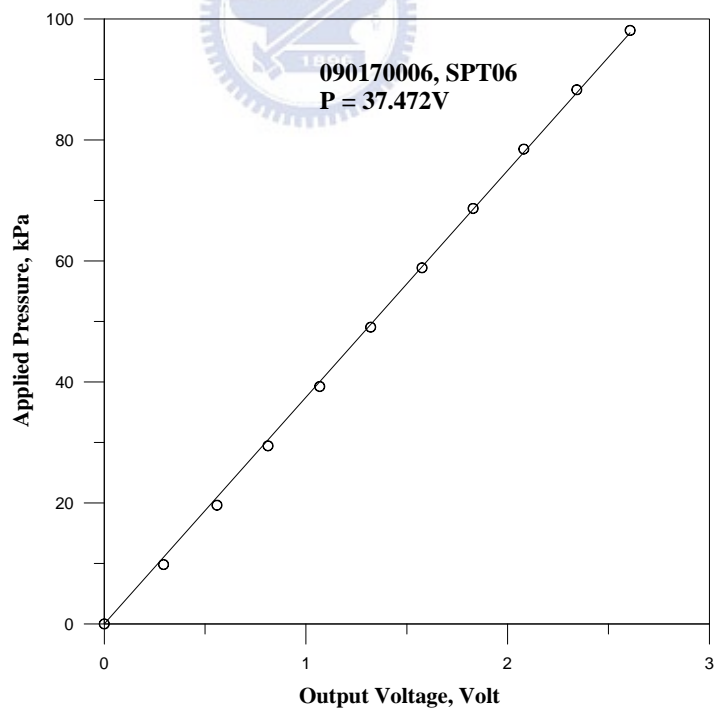
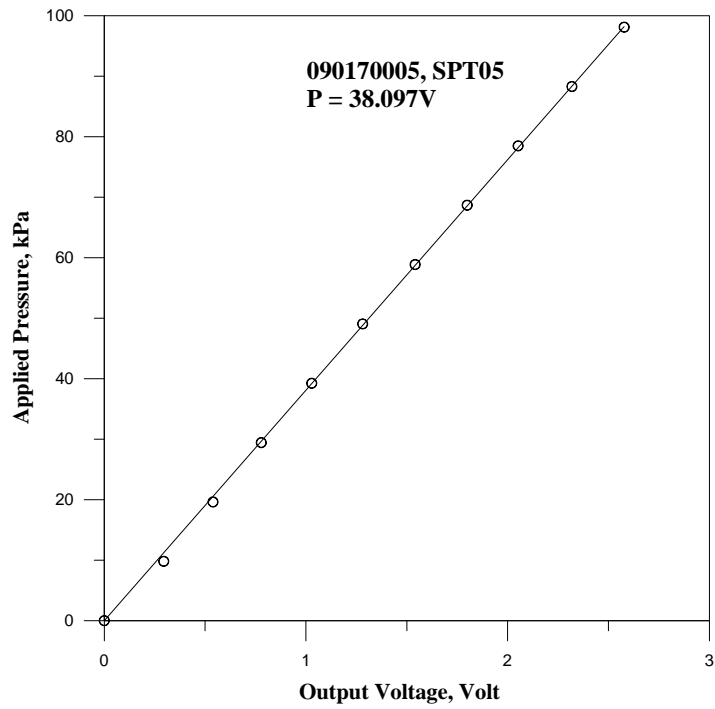


Fig. A.5. Applied pressure versus voltage output for soil pressure transducer SPT05 and SPT06

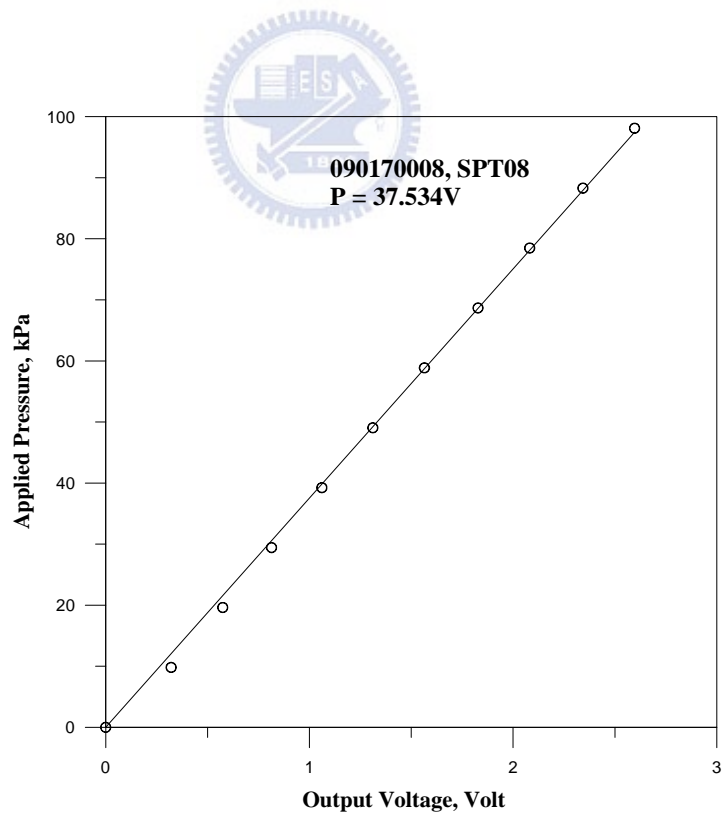
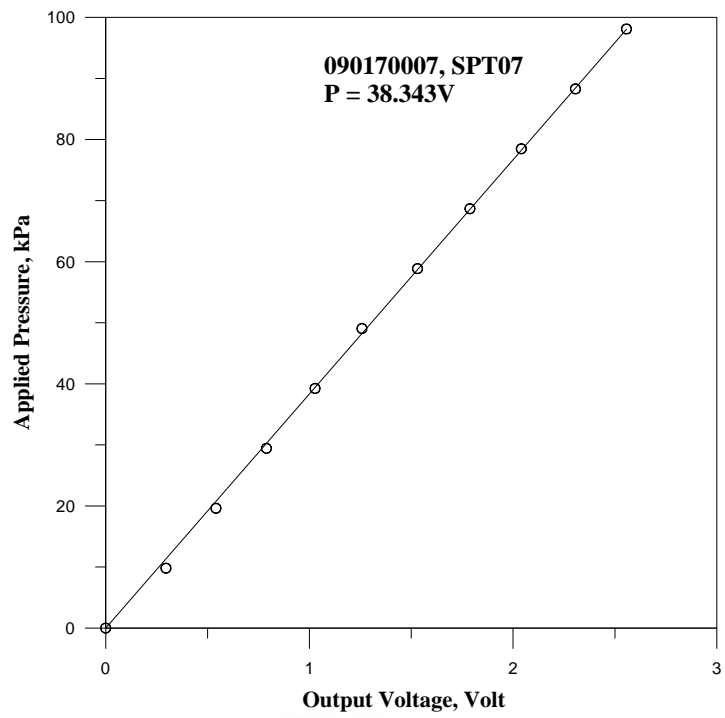


Fig. A.6. Applied pressure versus voltage output for soil pressure transducer SPT07 and SPT08

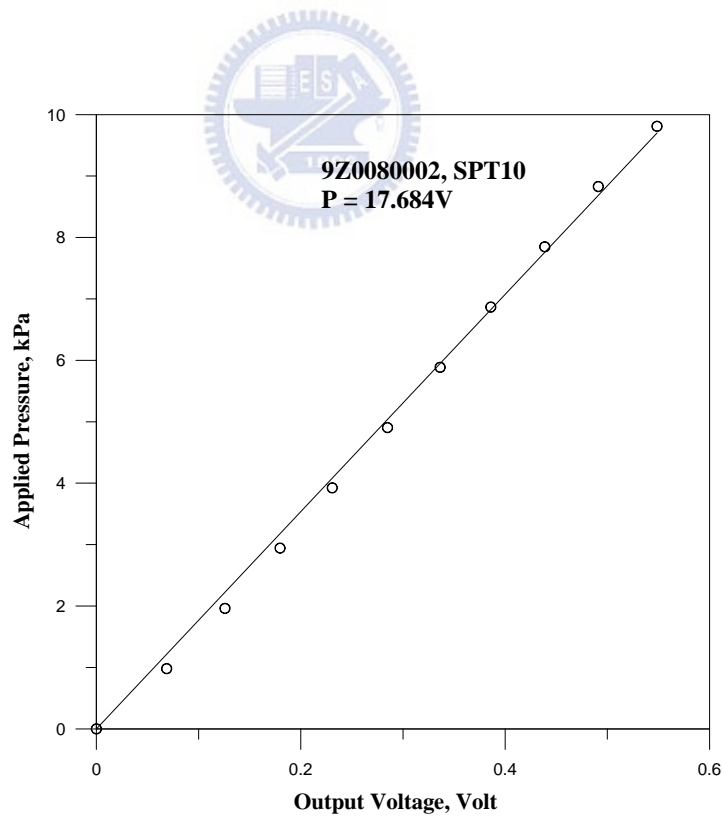
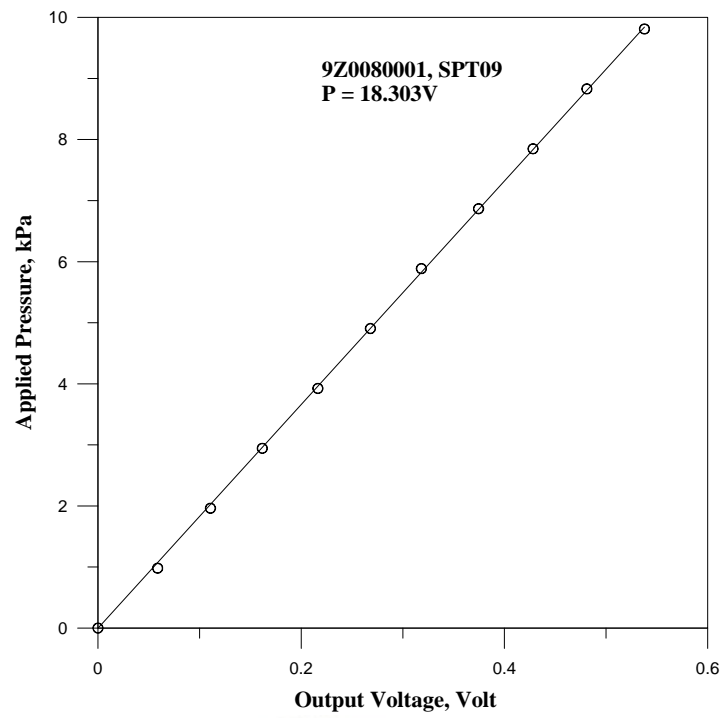


Fig. A.7. Applied pressure versus voltage output for soil pressure transducer SPT09 and SPT10

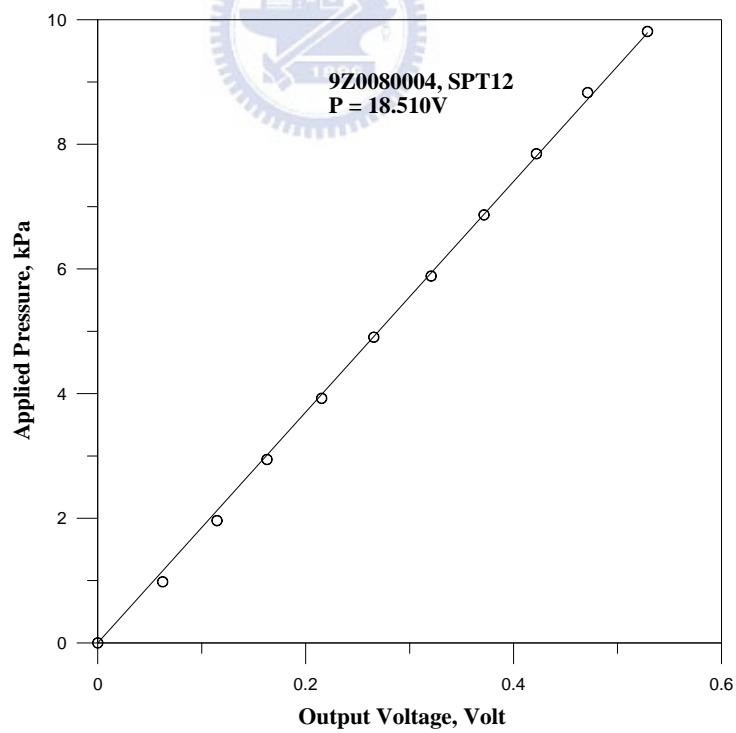
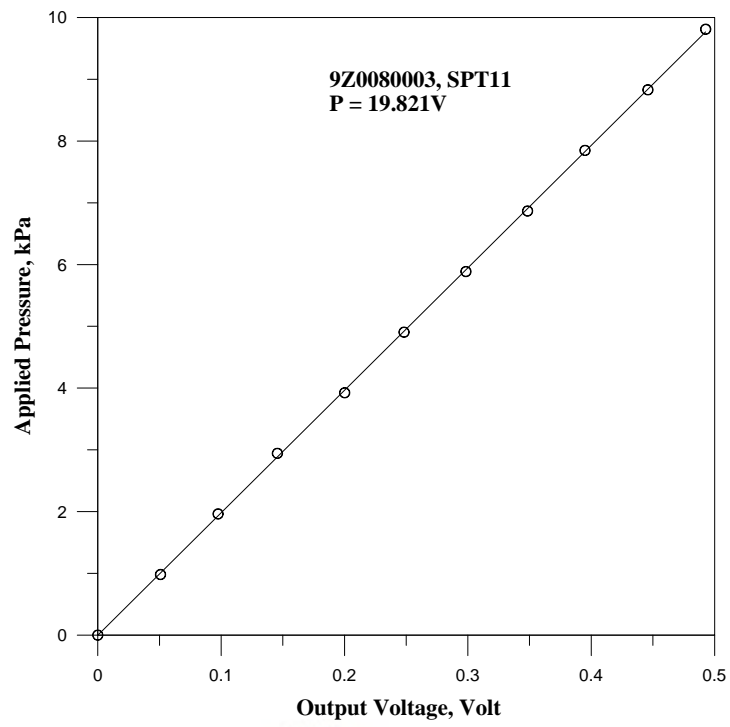


Fig. A.8. Applied pressure versus voltage output for soil pressure transducer SPT11 and SPT12

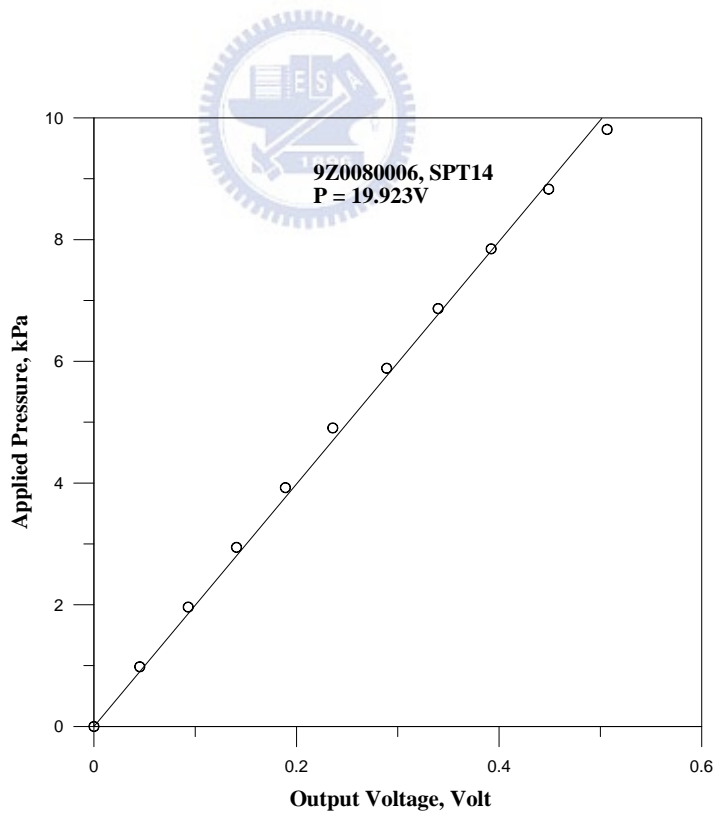
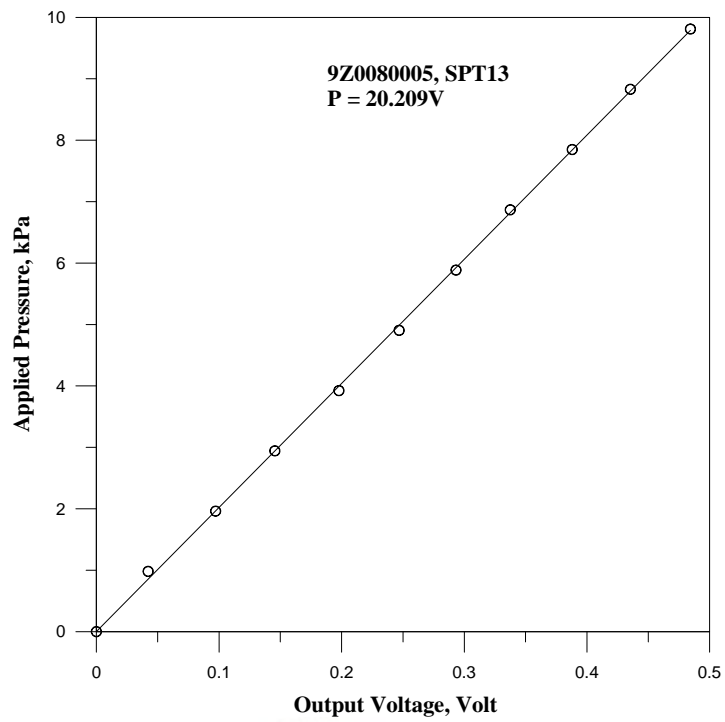


Fig. A.9. Applied pressure versus voltage output for soil pressure transducer SPT13 and SPT14

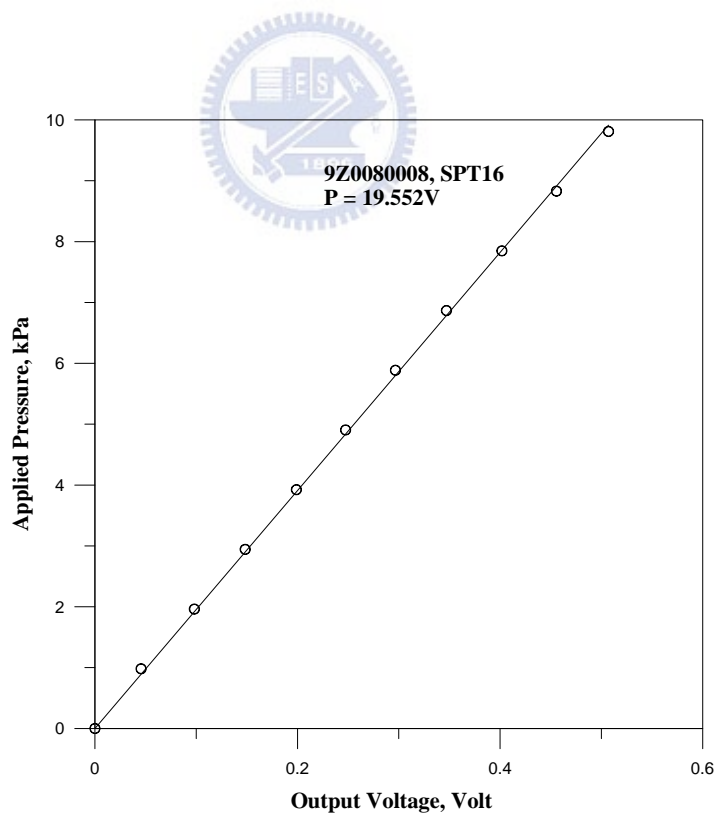
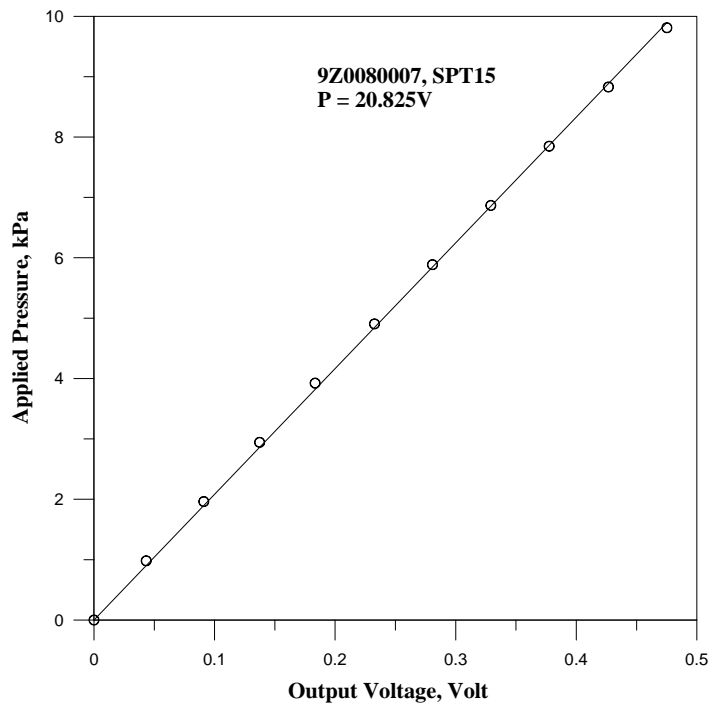


Fig. A.10. Applied pressure versus voltage output for soil pressure transducer SPT15 and SPT16

Appendix B

OPERATION OF SOFTWARE SURFER 8 AND GRAPHER 7 AND RELATIVE DENSITY MEASURED AT GRID POINTS AFTER POINT COMPACTION

This Appendix introduces the operating procedure of software Surfer 8, Grapher 7 and relative density measured at grid points after compaction. Surfer 8 interpolates with the values at grid points to form the data files of the contour line. Grapher 7 draws the contours by open the data files (Grapher Grid). The details of operation of Surfer 8 and Grapher 7 were indicated in the following:

- Step 1. Open the Program of Golden Software Surfer 8.
- Step 2. Choose the Function of Data from the Function of Grid.
- Step 3. Open the Test Data in the Form of Excel.
- Step 4. Choose Test Data to Corresponding X-Y-Z Coordinate.
- Step 5. The Test Data are Converted to the Form of Grapher Grid.
- Step 6. Open the Program of Golden Software Grapher 7.
- Step 7. Choose the Function of XY Grid in Contour Maps from the Function of Graph.
- Step 8. Open the Foregoing Saved file of Grapher Grid.
- Step 9. The Contours was Drawn by Surfer 7 with Adjust the Show Type.

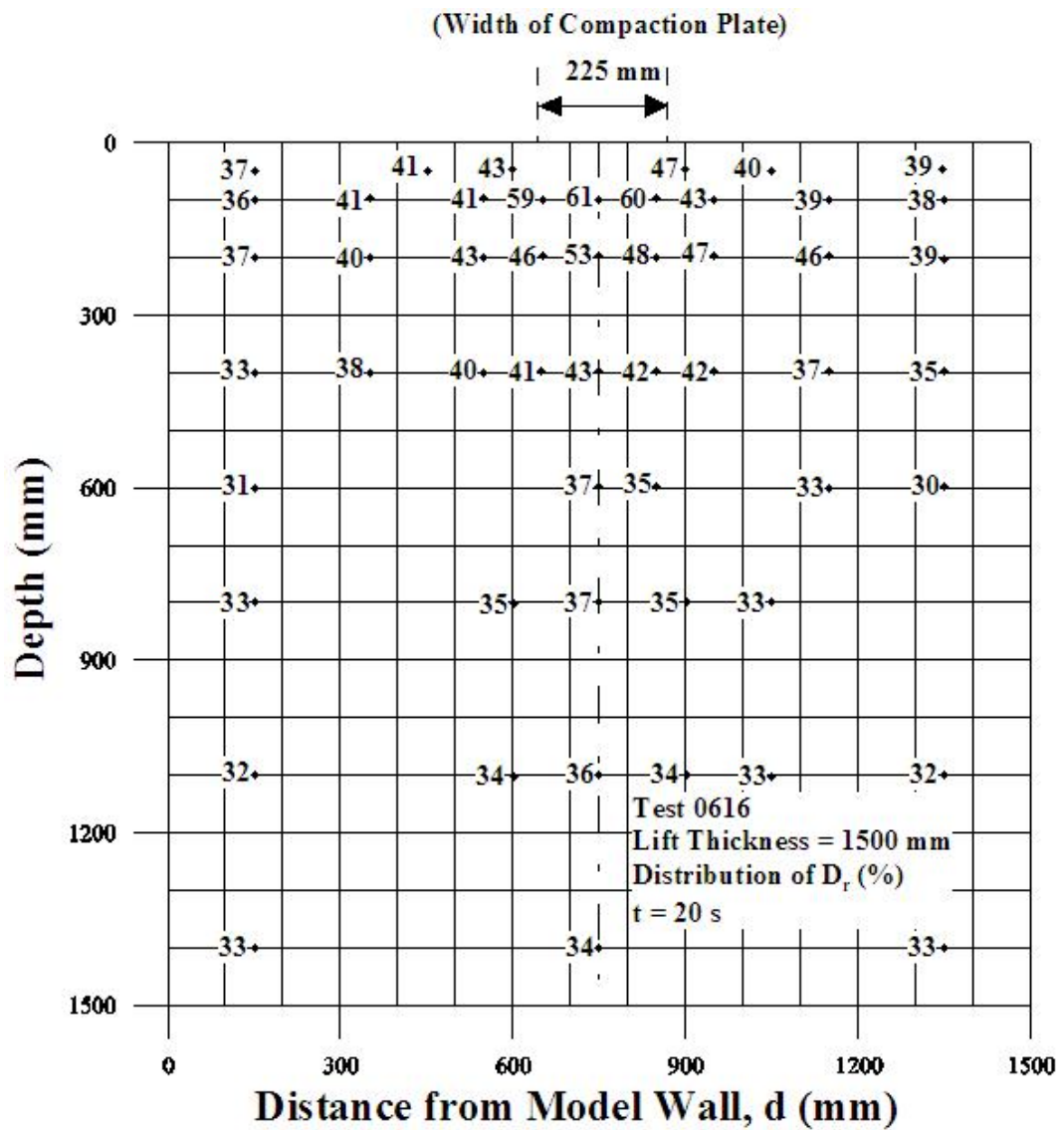


Fig. B.1. Relative density measured at grid points after 20 s of point compaction

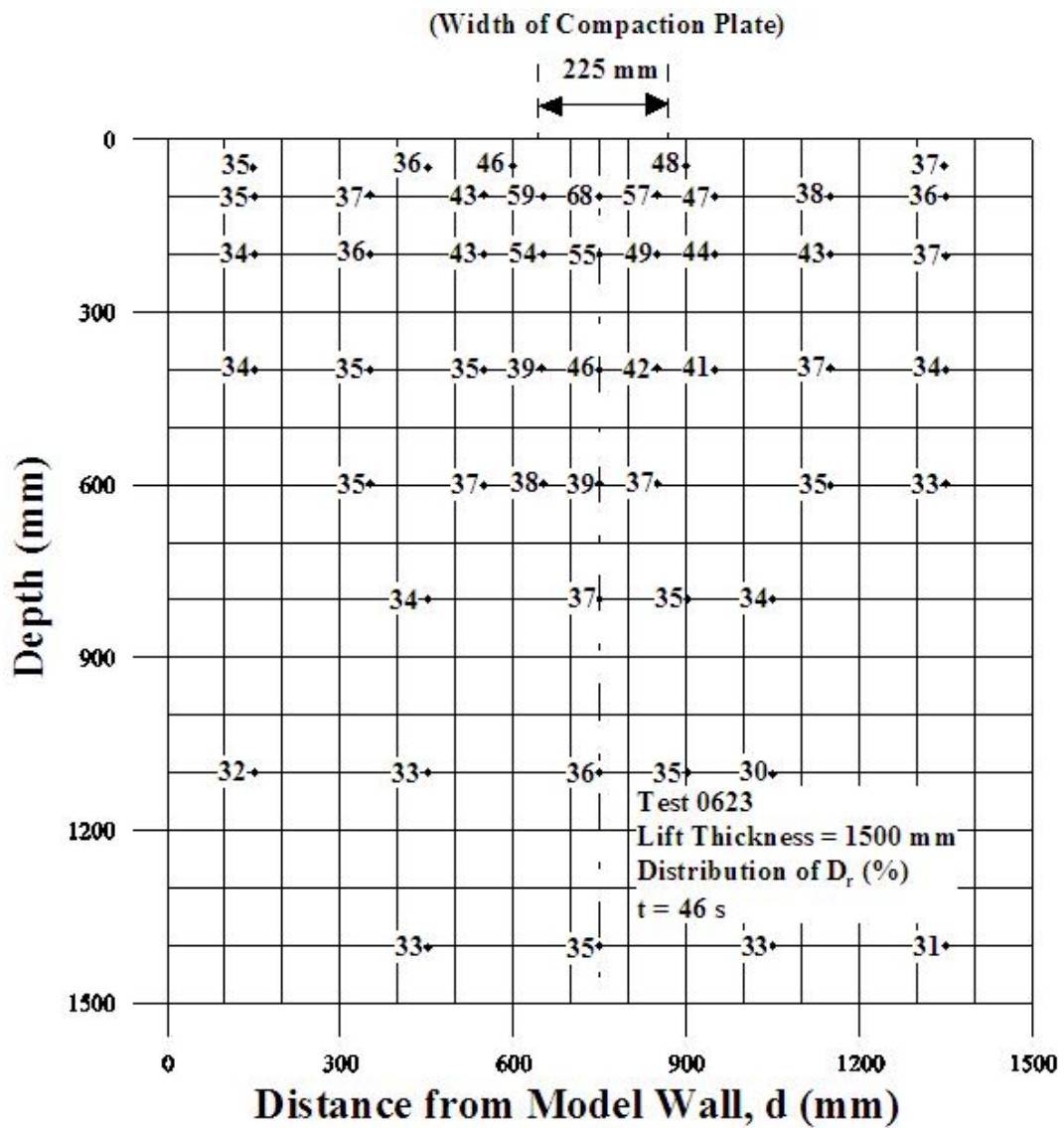


Fig. B.2. Relative density measured at grid points after 46 s of point compaction

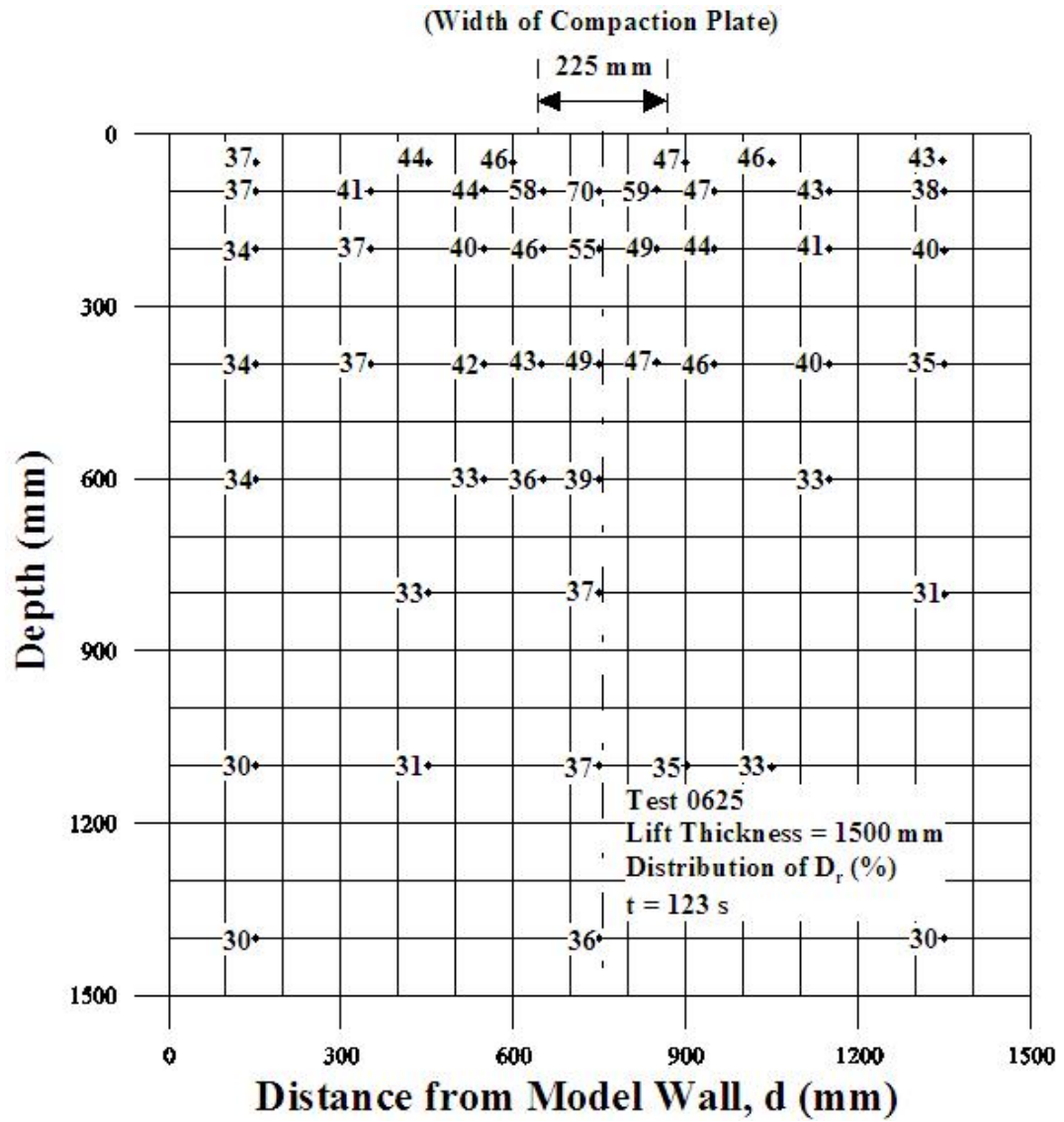


Fig. B.3. Relative density measured at grid points after 123 s of point compaction

Appendix C

$\Delta\sigma_v$ MEASURED AT GRID POINTS AFTER COMPACTION

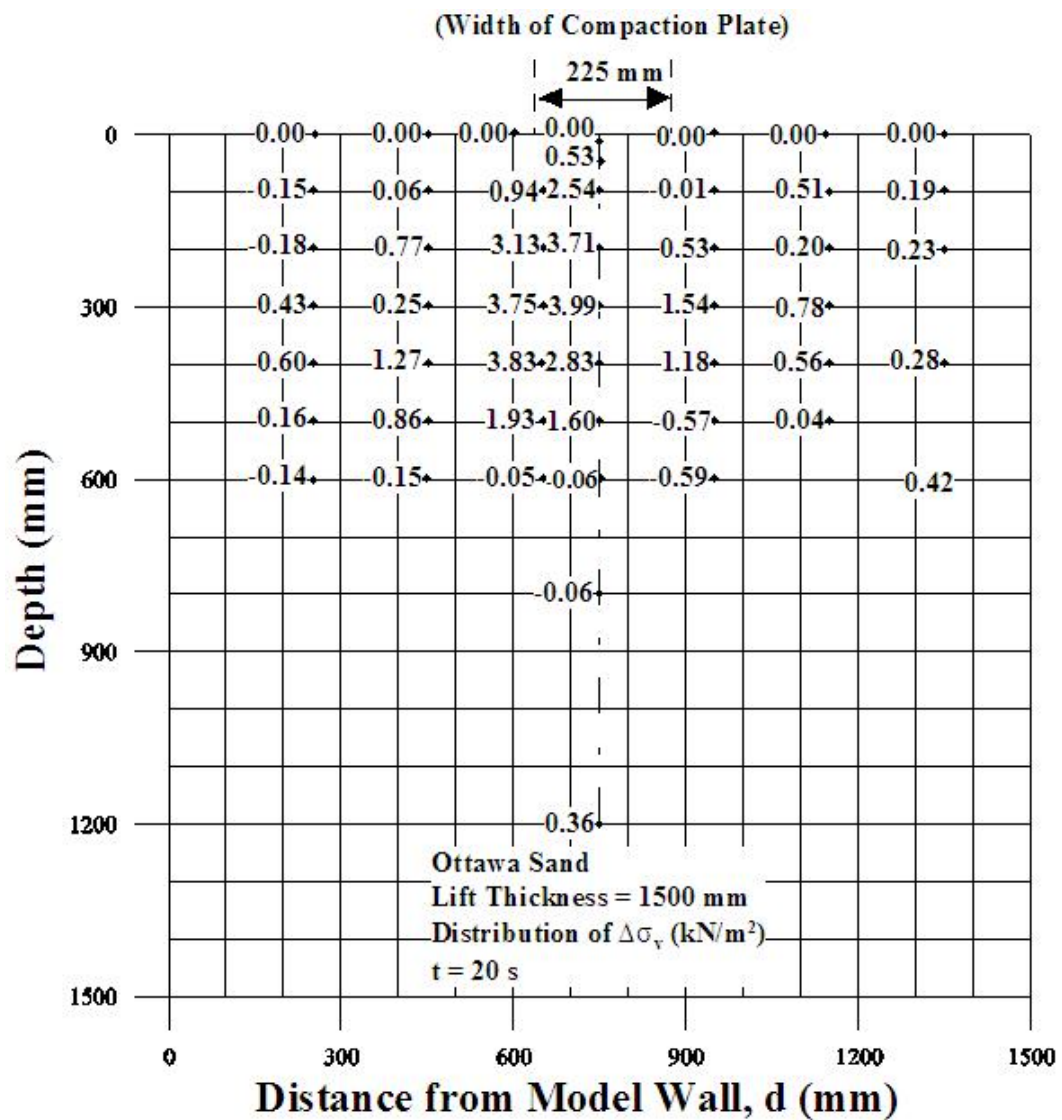


Fig. C.1. $\Delta\sigma_v$ after 20 s of point compaction measured at grid points

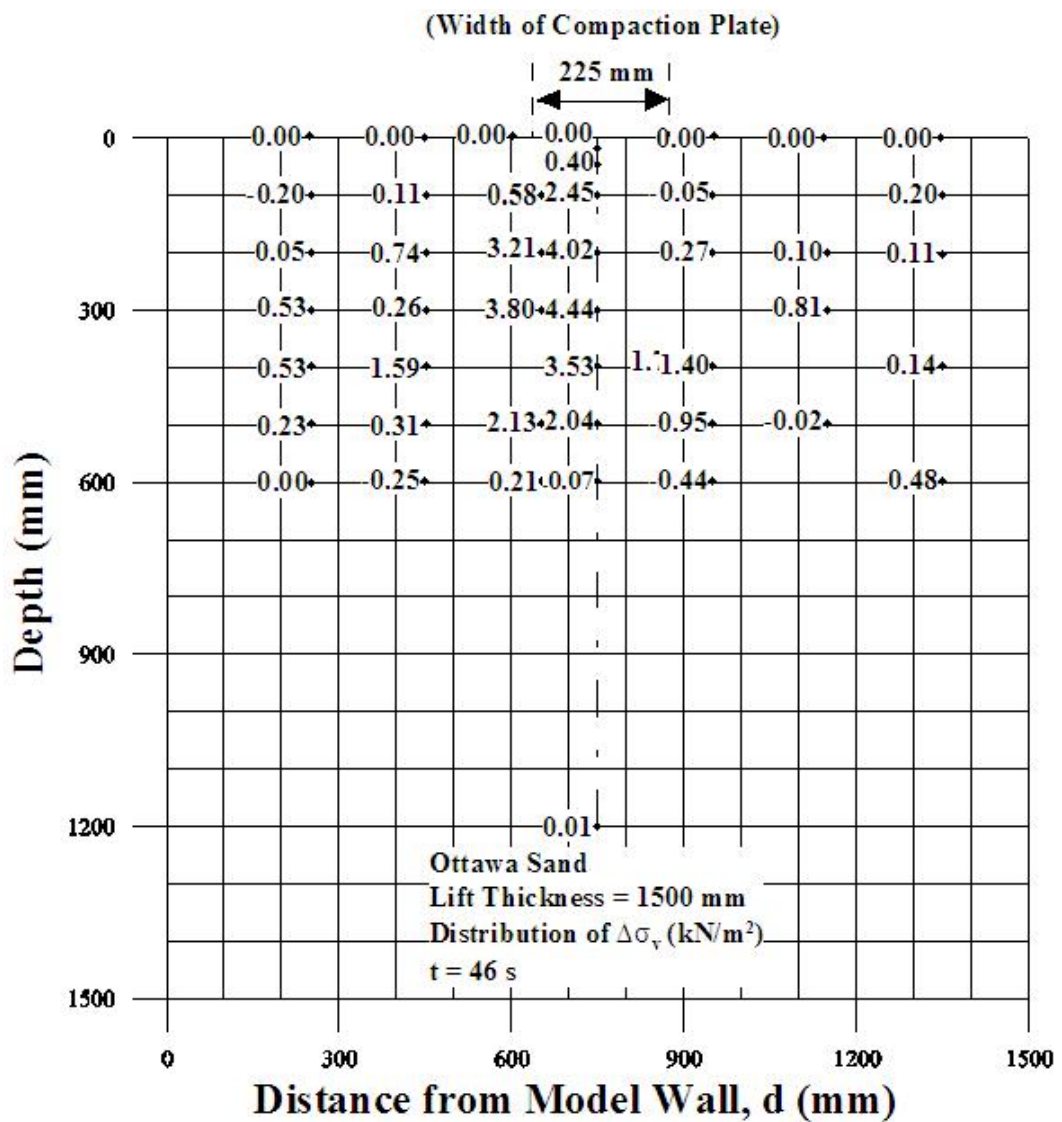


Fig. C.2. $\Delta\sigma_v$ after 46 s of point compaction measured at grid points

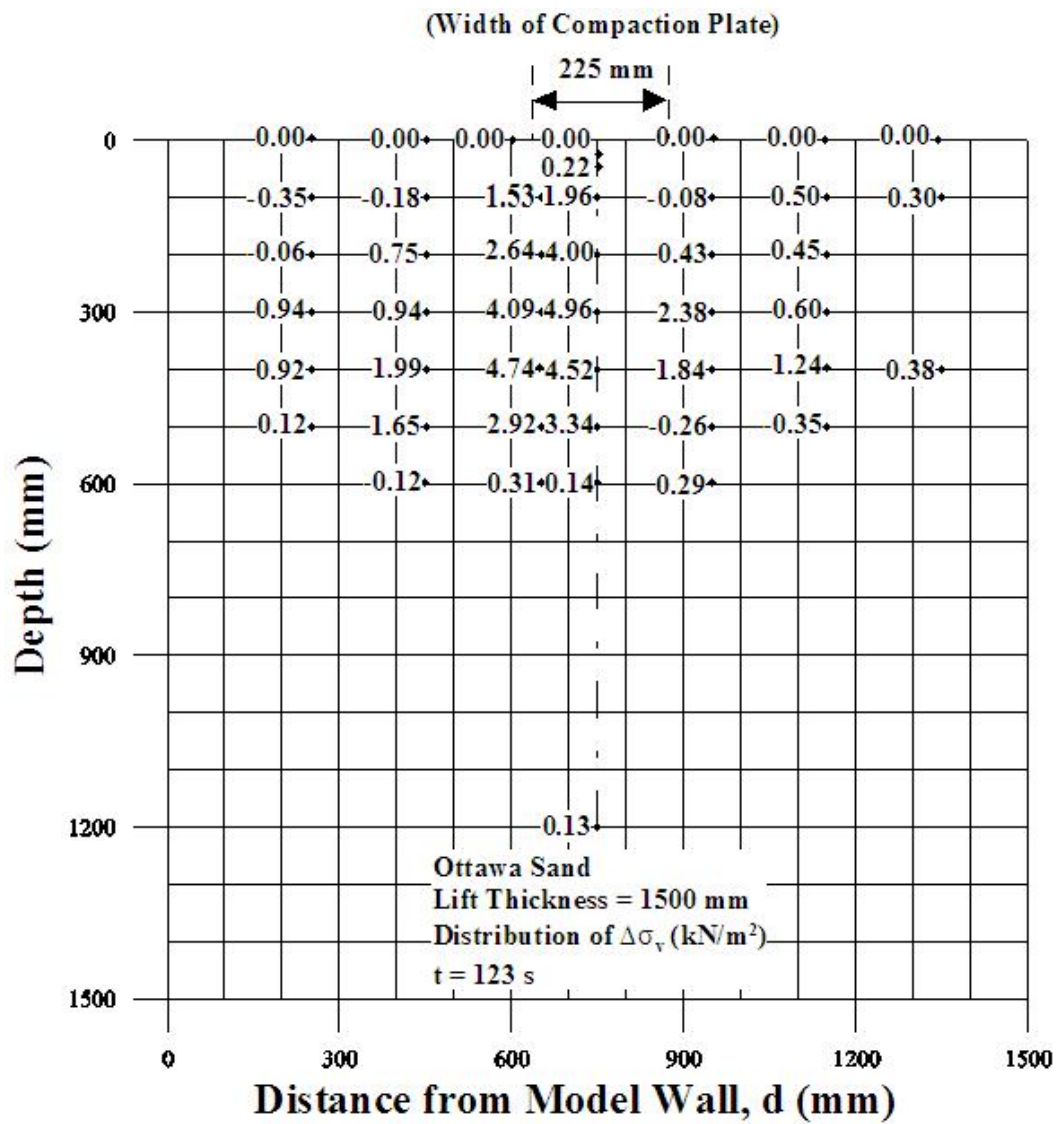


Fig. C.3. $\Delta\sigma_v$ after 123 s of point compaction measured at grid points

Appendix D

$\Delta\sigma_h$ MEASURED AT GRID POINTS AFTER COMPACTION

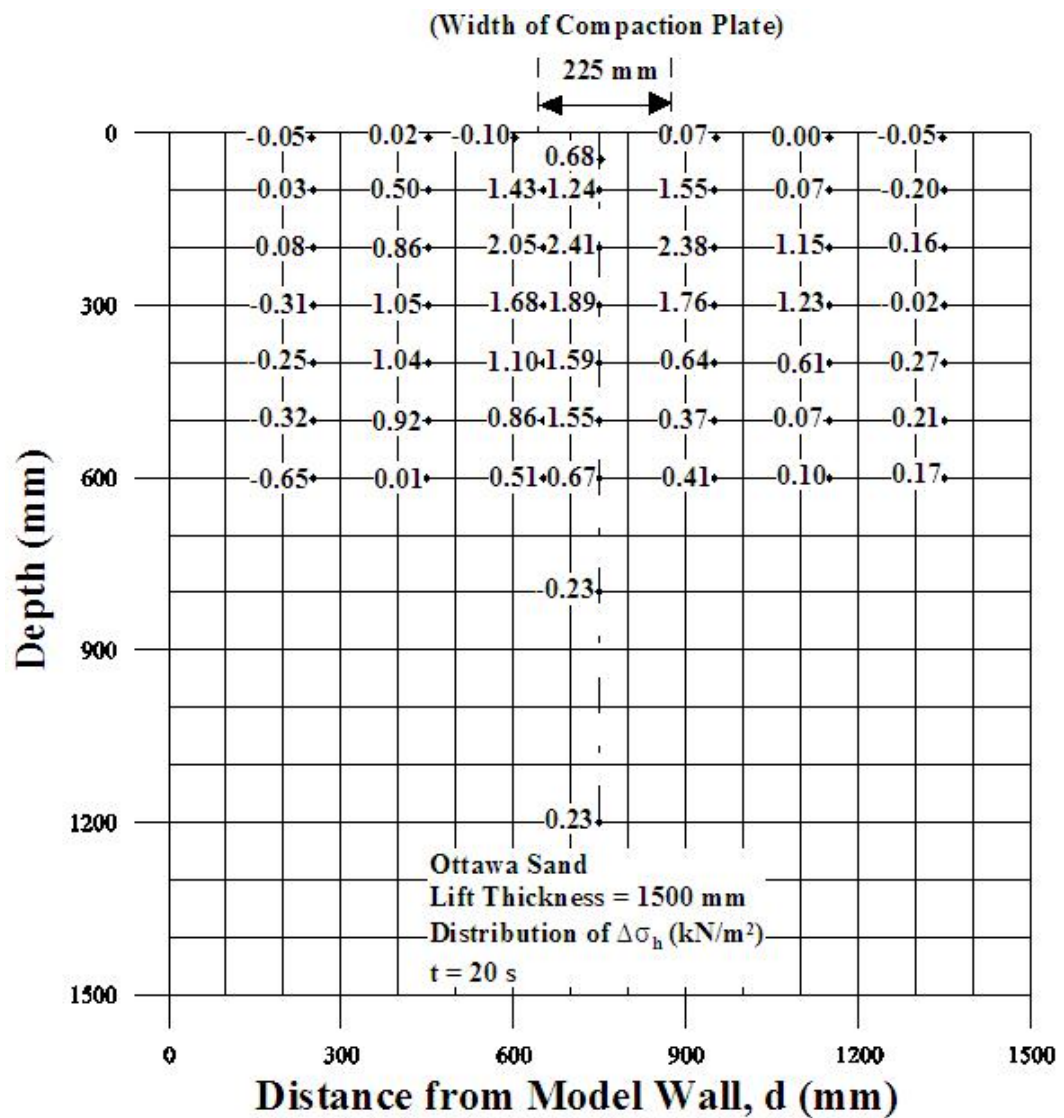


Fig. D.1. $\Delta\sigma_h$ after 20 s of point compaction measured at grid points

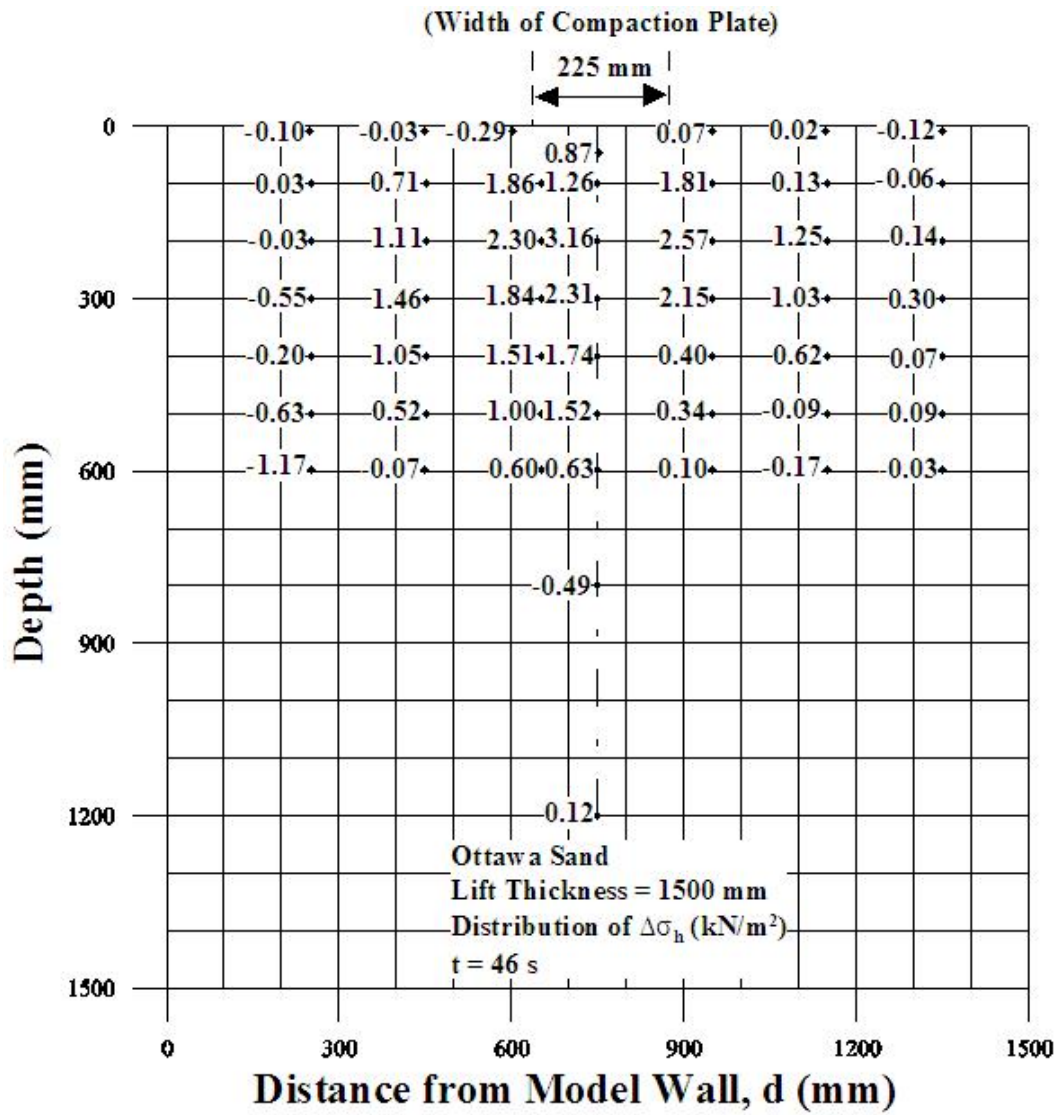


Fig. D.2. $\Delta\sigma_h$ after 46 s of point compaction measured at grid points

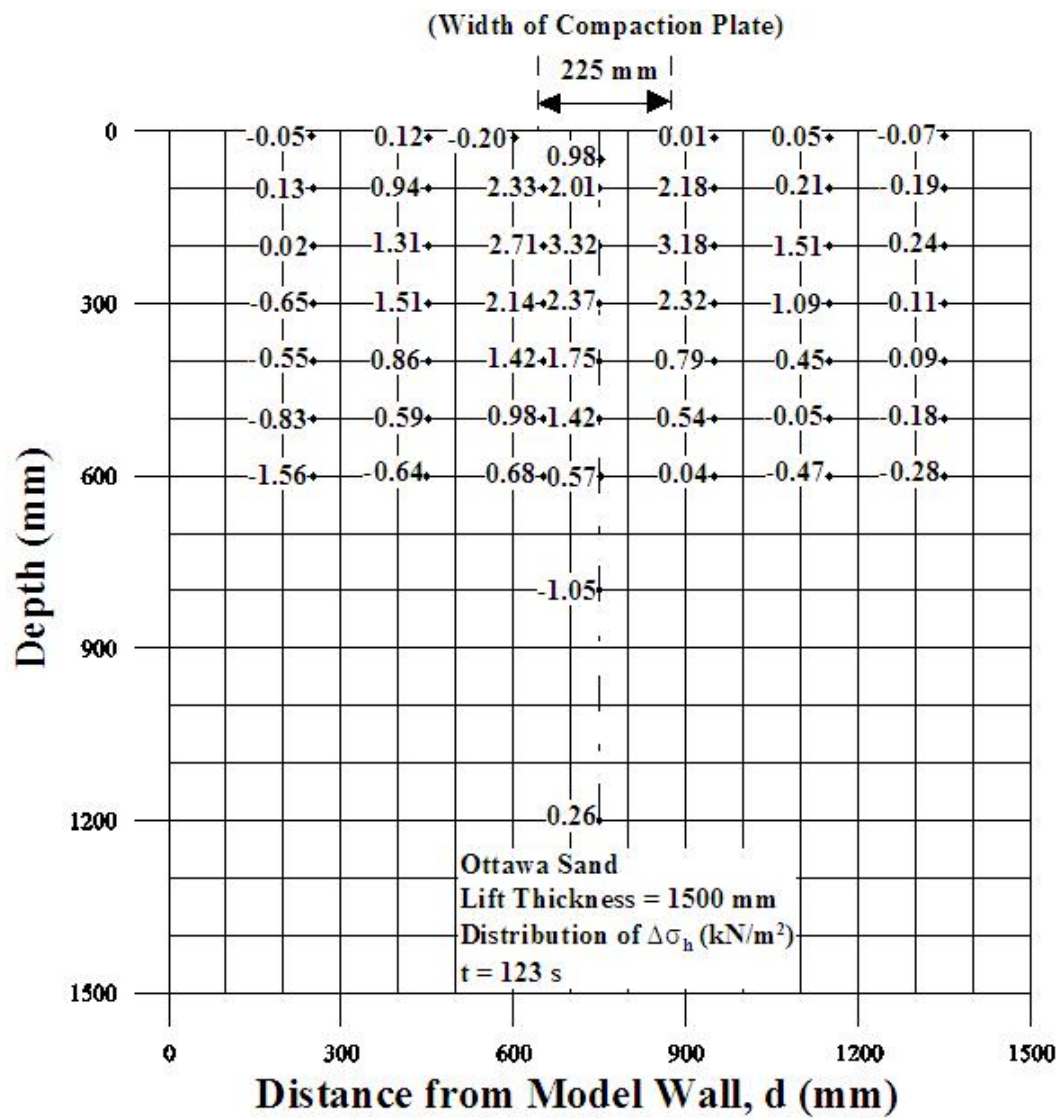


Fig. D.3. $\Delta\sigma_h$ after 123 s of point compaction measured at grid points